REPORT DOCUMENTATION PAGE

Form Approved
OMB No. 0704-0188

1. AGENCY USE ONLY (Leave blank)	2. REPORT DATE	3. REPORT TYPE AND DATES COVERED
	20 JAN 1995	FINAL REPORT

4. TITLE AND SUBTITLE

Visualization of Circuit Card Electromagneitc Fields

5. FUNDING NUMBERS

C: F41608-94-C-1126

6. AUTHOR(S)

Daniel Zwillinger

7. PERFORMING ORGANIZATION NAME(S) AND ADDRESS(ES)

Zwillinger & Associates
63 Greylock Road
Newton, MA 02165

8. PERFORMING ORGANIZATION REPORT NUMBER

AF95-1

9. SPONSORING/MONITORING AGENCY NAME(S) AND ADDRESS(ES)

LDAE-ADTIC
San Antonio Air Logistics Center
404 Greig St. BLDG 178
Kelly AFB, TX 78241-5944

10. SPONSORING/MONITORING AGENCY REPORT NUMBER

11. SUPPLEMENTARY NOTES

12a. DISTRIBUTION/AVAILABILITY STATEMENT

Approved for public release; SBIR report, distribution unlimited

12b. DISTRIBUTION CODE

13. ABSTRACT *(Maximum 200 words)*

Circuit boards are used in nearly every electrical appliance. Most board failures cause differing currents in the circuit board traces and components. This causes the circuit board to radiate a differing electromagnetic field. Imaging this radiated field, which is equivalent to measuring the field, could be used for error detection.

Using estimates of the fields radiated by a low power digital circuit board, properties of known materials, and available equipment, we determined how well the following technologies could be used to visualize circuit board electromagnetic fields (prioritized by promise): electrooptical techniques, magnetooptical techniques, piezoelectric techniques, thermal techniques, electrodynamic force technique.

We have determined that sensors using the electrooptical effect (Pockels effect) appear to be sufficiently sensitive for use in a circuit board imaging system. Sensors utilizing the magnetooptical effect may also be adequate for this purpose, when using research materials. These sensors appear to be capable of achieving direct broadband measurements.

We also reviewed existing electromagnetic field sensors. Only one of the sensors (recently patented) was specifically designed for circuit board measurements.

14. SUBJECT TERMS

VISUALIZATION, INTERFEROMETRY, ELECTROOPTIC EFFECT, MAGNETOOPTIC EFFECT, PIEZOELECTRIC EFFECT

15. NUMBER OF PAGES

84

16. PRICE CODE

17. SECURITY CLASSIFICATION OF REPORT	18. SECURITY CLASSIFICATION OF THIS PAGE	19. SECURITY CLASSIFICATION OF ABSTRACT	20. LIMITATION OF ABSTRACT
UNCLASSIFIED	UNCLASSIFIED	UNCLASSIFIED	SAR

NSN 7540-01-280-5500

Standard Form 298 (Rev. 2-89)
Prescribed by ANSI Std. Z39-18
298-102

REF 9

FINAL REPORT

VISUALIZATION OF CIRCUIT CARD EM FIELDS

CONTRACT NUMBER F41608–94–C–1126

Accesion For		
NTIS CRA&I	☒	
DTIC TAB	☐	
Unannounced	☐	
Justification		
By		
Distribution /		
Availability Codes		
Dist	Avail and / or Special	
A-1		

Zwillinger & Associates
63 Greylock Road
Newton, MA 02165

20 JANUARY 1995

Contents

List of Figures

List of Tables

Summary Report

This is the final report for Air Force contract F41608–94–C–1126: "Visualization of Circuit Card EM Fields".

Circuit cards (or circuit boards) of one type or another are used in nearly every electrical appliance used by the military or by commerce. This naturally includes computers, which are themselves used in many electrical appliances. To assure quality, all circuit board manufacturers use quality control testing to verify that the circuit board perform appropriately. There exist automated, readily available, and inexpensive testing mechanisms for unpopulated boards. However, for the testing of populated boards, the usual testing techniques are expensive due to the cost of construction of specialized test fixtures.

Most board failures are due to either bad solder joints or faulty components. Either of these errors results in differing currents in the circuit board traces and in the components on the board. These differing currents result in a differing electromagnetic field radiated by the circuit board. This differing electromagnetic field can be used as the basis for a detection mechanism of errors.

This report is concerned with the imaging of the electromagnetic fields radiated by circuit boards. If electromagnetic fields could be imaged, then the image of a powered test board could be compared to the image of a known good board or to a prediction of the image. This would permit more accurate quality control.

Visualizing the electromagnetic field surrounding a circuit board is equivalent to measuring an electromagnetic field in space. We have performed an extensive review of existing electromagnetic field sensors and found that several of the technologies we proposed studying have already been studied. However, only one of the sensors we found, which was recently patented, was specifically designed for measuring circuit board electromagnetic fields. Several of the sensors we found could not be applied to measuring circuit board electromagnetic fields, due to frequency limitations or other factors.

Using estimates of the electromagnetic fields generated by a low power digital circuit board (populated on only one side), properties of known materials, and available commercial off the shelf equipment, we have determined how well the following technologies could be used to visualize circuit board electromagnetic fields (listed in order of promise):

1. electrooptical technique
2. magnetooptical techniques
3. piezoelectric techniques
4. thermal techniques
5. electrodynamic force technique

Briefly, we have determined that sensors using the electrooptical effect (Pockels effect) appear to be sufficiently sensitive for use in a circuit board imaging system. Sensors utilizing the magnetooptical effect may also be adequate for this purpose, if research materials are used. These sensors appear to capable of achieving direct broadband measurements. To measure the output of these sensors, very sensitive equipment is required; the needed capabilities of such equipment have been demonstrated by others in laboratory settings.

The electrooptical effect is also the basis for the above mentioned patented electromagnetic field sensor, which was designed for circuit card applications. However, the sensor techniques studied in this report have modes of operation very different from the patented sensor.

1 Introduction

This is the final report for Air Force contract F41608–94–C–1126: "Visualization of Circuit Card EM Fields". The contents of this report are:

- The introduction, which also introduces the proposed new types of electromagnetic field sensors.
- A survey of circuit boards, their characteristics and size (see section 2).
- An estimate of the electromagnetic fields which a sensor, used for circuit board visualization, must be able to measure (see section 3).
- A survey of existing electromagnetic field sensors (see section 4).
- A survey of the sensitivity capabilities of commercially available ancillary measurement devices needed for use with an electromagnetic field sensor (see section 5).
- A tabulation of the parameters of available exotic materials (such as electrooptical materials and magnetooptical materials) considered for use as part of a new visualization technique (see section 6).
- A comparison of performance results of the proposed new techniques (see section 7).
- A discussion of the use of visualization in the comparison of different images for the purpose of fault detection (see section 8).
- Conclusions and recommendation of our research (see section 9).

In addition, this report contains a number of reference sections. These include:

- A bibliography (see section A).
- A list of acronyms (see section B.1).
- A list of mathematical notation (see section B.2).
- A glossary (see section B.3).
- An index appears at the end of the document.

1.1 Purpose of the research

Circuit cards (or circuit boards) of one type or another are used in nearly every electrical appliance used by the military or by commerce. This naturally includes computers, which are themselves used in many electrical appliances. To assure quality, all circuit board manufacturers use quality control testing to verify that circuit board perform appropriately. There exists automated, readily available, and inexpensive testing mechanisms for unpopulated boards. However, for the testing of populated boards, the usual testing techniques are expensive due to the cost of construction of specialized test fixtures.

Most board failures are due to either bad solder joints or faulty components. Either of these errors results in differing currents in the circuit board traces and in the components on the board. These differing currents result in a differing electromagnetic field radiated by the circuit board. This differing electromagnetic field can be used as the basis for a detection mechanism of errors.

This report is concerned with the imaging of the electromagnetic fields radiated by circuit boards. If electromagnetic fields could be imaged, then the image of a powered test board could be compared to the image of a known good board or to a prediction of the image. This would permit better quality control.

Visualizing the electromagnetic field surrounding a circuit board is equivalent to measuring an electromagnetic field in space. Hence, this report is mostly about electromagnetic field sensors.

1.2 Possible new testing techniques

This section introduces several proposed sensing technologies. All but one of the sensing techniques described in this report use the geometry shown in figure 1, which shows the side view of a single-sided circuit board with a measurement apparatus above it. Note that there are traces, resistors, solder, and other components on the populated side of the circuit board and traces and solder on the unpopulated side of the circuit board. Some vias, which connect the two sides of the circuit board, are also indicated.

In all the new measurement techniques described in this report the powered circuit board radiates an electromagnetic field that interacts with a sensing sheet. Depending on the technology under study, the measurement system will use information obtained in one of three ways: (A), (B), or (C) in figure 1. Any

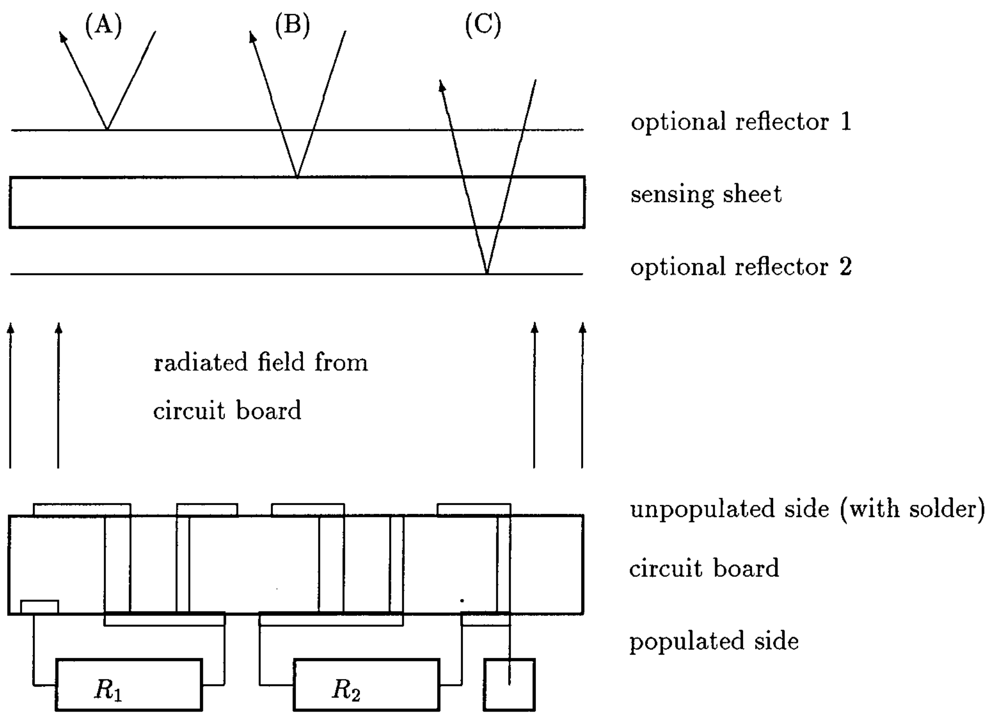

Figure 1: The physical apparatus over a circuit board

optional reflectors, when present, are bonded to the sensing sheet. The measurement technologies studied in this report are, briefly (more detailed descriptions are included with the comparisons in section 7):

1. electrodynamic technique

   For this technique, the sensing sheet is a thin sheet of a conductor carrying a surface current. The magnetic field from the circuit board interacts with the surface current to create an electrodynamic force that deforms the sensing sheet.

   The deformations of the sensing sheet are then measured using measuring technique (A). Only optional reflector 1 is required.

2. piezoelectric technique

   For this technique, the sensing sheet is a thin sheet of a piezoelectric material. The electric field from the circuit board interacts with the sensing sheet to create a stress which deforms the sensing sheet.

   The deformations of the sensing sheet are then measured using measuring technique (A). Neither reflector is required.

3. electrooptical technique

   For this technique, the sensing sheet is a thin sheet of an electrooptical material. The electric field from the circuit board interacts with the sensing sheet causing the polarization of an incident light wave to rotate.

   The polarization angle is then measured using measuring technique (C). Only optional reflector 2 is required.

4. magnetooptical technique: Faraday effect

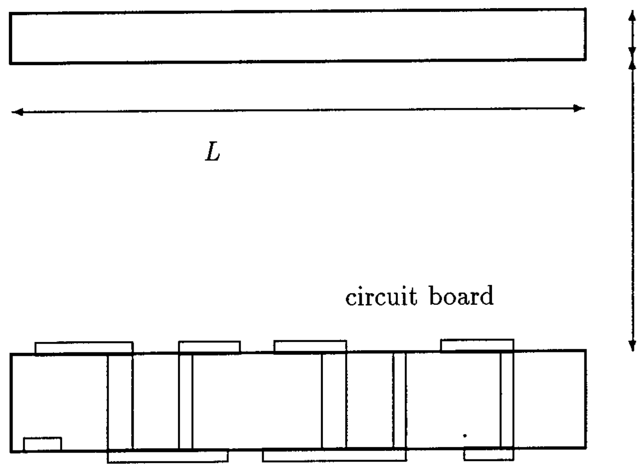

Figure 2: Dimensions of the physical apparatus

For this technique, the sensing sheet is a thin sheet of a magnetooptical material. The magnetic field from the circuit board interacts with the sensing sheet causing the polarization of an incident light wave to rotate.

The polarization angle is then measured using measuring technique (C). Only optional reflector 2 is required.

5. magnetooptical technique: Kerr effect

   For this technique, the sensing sheet is a thin sheet of a magnetooptical material. The magnetic field from the circuit board interacts with the sensing sheet causing the polarization of an incident light wave to rotate.

   The polarization angle is then measured using measuring technique (B). Only optional reflector 2 is required.

6. thermal techniques: piezoelectric slurry and direct imaging

   Neither of these techniques uses measurement systems (A), (B), or (C).

   For the first technique, the sensing sheet is a slurry of a piezoelectric material. The periodic electric field from the circuit board interacts with the sensing sheet to introduce periodic stress in the slurry. These stresses generate heat in the slurry and the temperature of the slurry is then measured.

   For the second technique, there is no sensing sheet. In this case the temperature of the circuit board is directly measured.

The dimensions of the sensing sheet, and its distance from the circuit board are defined by figure 2. The dimensions assumed for the computations in this report are given in table 1. These nominal values are used consistently in all of the estimates of performance contained in this report.

1.3 Uses of a near-field electromagnetic field sensor

1.3.1 Diagnostic Tool

A conservative estimate is that tens of millions of circuit cards are constructed each year. Note that the term "circuit card" can have many interpretations. The circuit cards that we are familiar with have currents

Parameter	Definition	Nominal value
L	length of sensing sheet	$L = 10$ cm
h	height of sensing sheet about circuit board	$h = 2$ mm
t	thickness of sensing sheet	$t = 1$ mm
w	width of sensing sheet	$w = 20$ cm

Table 1: Table of nominal geometrical parameters for the apparatus

ranging from micro-amps (for CMOS logic) to milli-amps (for TTL logic), and frequencies of operation from KHz to MHz.

To assure quality, all circuit card manufacturers use quality control testing to verify that circuit cards perform appropriately. The errors that are of particular concern are shorts between traces and breaks within a trace. Either of these errors will result in a differing current on a circuit board, and hence a differing electromagnetic field. Detection of this differing electromagnetic field can be used as the basis for a testing mechanism.

1.3.2 Predictive Tool

If the electromagnetic field surrounding a circuit card can be numerically simulated from the CAD design of the circuit card, then an electromagnetic field measurement device could be used to verify the predictions. Since it is possible to determine the electromagnetic field at a large distance from an object by using the electromagnetic field close to the object (see, for example, Laroussi and Costache [61]) near field measurements could, in principle, be used to determine the EMI at 3 meters and 10 meters (the usual distances for EMC concerns).

Because numerical simulations are difficult to perform accurately (see section 3.3), near-field electromagnetic field sensors are not presently used in this capacity.

2 Circuit Cards

This section contains a background on circuit cards.

2.1 Standards

There are many books describing the design and manufacture of circuit boards. See, for example, Clark [21].

The Institute for Interconnecting and Packaging Electronic Circuits[1] (IPC) is a United States based trade association dedicated to furthering the competitive excellence and financial success of its members worldwide, who are participants in the electronics interconnect industry. The IPC has created the following major standards documents:

- IPC-A-600C: *Guidelines for Acceptability of Printed Boards*
- IPC-D-300G: *Printed Board Dimensions and Tolerances*
- IPC-D-350D: *Printed Board Description in Digital Form*
- IPC-D-351: *Printed Board Drawings in Digital Form*
- IPC-D-352: *Electronic Design Data Description for Printed Boards in Digital Form*
- IPC-D-354: *Library Format Description for Printed Boards in Digital Format*
- IPC-D-356: *Bare Board Electrical Test Information in Digital Form*
- IPC-ET-652: *Guidelines and requirements for Electrical Testing of Unpopulated Printed Boards*
- IPC-RB-276: *Qualification and Performance Specification for Rigid Printed Boards*

Similar military standards may be found in:

- MIL-P-1394F: *Plastic Sheet, Laminated, Metal Clad (for Printed Circuit Boards)*
- MIL-P-55110D: *General Specification for Printed Wiring Boards*
- MIL-STD-2118: *Design Requirements for Flex and Rigid-Flex Printed Wiring for Electronic Equipment*
- MIL-STD-275E: *Printed Wiring in Electronic Equipment*

The document MIL-STD-275C divides printed circuit boards into two types. Type I includes boards with interfacial connections, or connections that go from one board side to the other, or boards with clinched jumper wire soldered to both sides. Boards that are eyeletted by a funnel-flanged eyelet or plated-through hole with a solder plug fall within type II.

The same specification divides the boards according to the method of attaching components:

- TYPE A: eyelets with clinched leads
- TYPE B: bare holes or plated-through holes
- TYPE C: standoff terminals staked and soldered to the conductive pattern

2.2 Printed circuit board specifications

Because of the need for ever more complicated and dense circuit boards, the circuit board industry has invested heavily in computer aided design (CAD) techniques. The concept is that the designer should create the board (with the help of the computer), and that all needed information should be obtained from that one design. That is, the CAD design should be used for artwork layout, computer-aided manufacturing[2] (CAM), and construction of test fixtures.

For this process to work, the circuit board design must be written in a "language" that allows all of the relevant information to be obtained. There are several specification languages that are currently being used, the major ones include:

- Gerber The Gerber format is one of the most fundamental languages, but it is quite dated and is not very intelligent (it does not readily transfer all needed information).

[1] IPC, 7380 N. Lincoln Ave, Lincolnwood, Illinois, 60646.
[2] CAM includes hole drilling, plating, assembly, etc.

- IPC's D-350 specification

  The IPC designed the D-350 language in response to Gerber, it has been repeatedly updated for the last 20 years. At this time the military is one of the main supporters of the D-350 language.

  While there are presently many CAM facilities that use the D-350 language, there are few CAD programs that use this language.

- EDIF PCB

  A PCB interchange standard based on the Electronic Design Interchange Format has been announced (see [37]). This standard, EDIF PCB, is slated for release in November 1994. It should ease the task of transporting layouts from one CAD system to another. The November release will contain an information model with 155 entities covering 14 major sections: material, technology, documentation, geometry, package library, parts library, mountable package library, net-list, design rule, sub-layout, footprint mapping, and assembled board and design.

There are also many proprietary formats used by manufacturers of CAD tools. For example:

- CAM Software Research[3] manufactures "Gerbln" (which comes in both shareware and professional versions). The output formats that can be produced include: Allegro, Cadstar, Maxi PC, Mentor, P-CAD, PADS-PCB, PADS-Perform, Protel-PCB, Tango-PCB, Ultiboards, Visula.

- Protel[4] manufactures "Advanced PCB 2" which performs printed circuit board layout. Output formats include: Protel binary, Protel ASCII, Autotrax, Gerber 2:3, 2:4 and 2:5 numeric formats, Excellon NC Drill, DXF, Pick and Place, BOM, ECO reports.

There is also a company that specializes in constructing translators for the CAE/CED/CAM industry. Router Solutions[5] manufactures over 120 different database translators, connecting the following different formats: AutoCAD DXF, CV Theda, Cadence Allegro, Cadul Ariadne, Calay V04/V05/PRISMA, EE Designer, Engineer, IGES Version 3, Intergraph PCB Massteck, Mentor, PADS-PCB-2000-UX, PCAD, Protel Autotrax & PFW, Redac Maxi-PC Cadstar, Redac Visula, Spea top-CAD, Tango, Ultiboard, and Zulen. They can also translate the following formats to IPC350 or IPC356: CBDS, CV Theda, Cadence Allegro, Cadnetix, Calay V04/V05/PRISMA, EE Designer, HPPCDS, Mentor, PADS PCB-2000-UX, PCAD, Protel Autotrax/PDW, Redac Maxi-Cadstar, Redac Visula, SciCards, Tango, and Ultiboard.

2.3 Novel circuit boards

While the majority of existing PCPs use orthogonal routing, newer high-speed boards implement point-to-point routing.

About 24 years ago, the concept of using fine wires instead of etched boards was proposed. Advanced Interconnection Technology[6] now creates circuit boards that use this technology. The wires used are circular in cross section, with a diameter of 2.5, 4, or 6.3 mils. Each wire has approximately 1 mil of insulation, and a 0.6 mil coating of adhesive. Since the wires can be placed on top of each other, the two-sided circuit boards that I-CON creates perform the work of a multi-layered board. More details of the parameters of this type of circuit board are in table 2. The sequence of construction steps for these boards is as follows: print and etch voltage and ground planes, pre-preg, epoxy adhesive, wires, overlying material. There are no vias required. Holes are drilled through the overlying material to connect with the wires. The normal separation of wires is 10 mil, center-to-center. In order to reduce EMI emissions, I-CON also makes these boards with a layer of copper on top to shield the wires.

A review of design methods that can be used to reduce EMI emissions is in Maddocks [67].

[3] CAM Software Research, Inc., 30 Maplewood Avenue, Portsmouth, NH 03801
[4] Protel Technology, Inc., 4675 Stevens Creek Blvd, Suite 200, Santa Clara, CA, 95051
[5] Router Solutions Inc., 180 Newport Center Drive, Suite 240, Newport Beach, CA 92660
[6] Advanced Interconnection Technology, 181 Freeman Ave, Islip, NY 11751

Wire size	Insulation thickness	DC current carrying capacity
0.0025"	0.0009"	0.300 amps
0.0040"	0.0011"	0.500 amps
0.0063"	0.0006"	0.850 amps

Other parameters	Value
Wiring grid	0.010" minimum
Hole size	0.016" minimum (standard)
Surface features	0.0004" lines, 0.0003" spaces (minimum)
Wiring grid	0.010" minimum

Table 2: Multi-wire parameters

Fault	Relative Frequency
Shorts	51
Opens	1
Absent	5.9
Wrong	13.0
Reversed	5.5
Bent leads	8.4
Analog specs	4.9
Logic	5.3
Performance	5.0

Table 3: Fault spectra for through-hole devices

2.4 Types of circuit faults

Types of circuits faults include

- open circuits
- a short circuit with another conductor in the same circuit
- a ground, which is a short circuit between a conductor and ground
- leakage (a high resistance path across a portion of the circuit, to another circuit, or to ground)
- a cross (a short circuit or leakage between conductors of different circuits)

From Langley *et al.* [60] we find the relative number of faults for through-hole devices to be as shown in table 3 (no description is given for the faults mentioned). From this table we observe that the predominant error is the occurrence of shorts.

Also, from a GenRad advertisement for the analog measurement device "Opens Xpress" we find

> "The problem with testing and diagnosing opens, one of the most common faults associated with surface mount boards, has been the complexity and cost of test generation."

2.5 EMI/EMC

Many applications of circuit boards are in locations where electromagnetic interference (EMI) could pose a problem. Hence, a concept of electromagnetic compatibility (EMC) has been developed. In order to comply with various governmental requirements (FCC, CISPR 22, etc.) the radiated electric fields of digital electronic products must be measured and cannot exceed certain levels (see, for example, Paul [82]). It has been shown that the dominant contributors to radiated emissions of a digital device are the common-mode currents on the conductors of that device (see Paul [81, 82]).

The visualization concept explored in our work requires that a board have near-field electromagnetic energy. Some manufacturers deliberately try to reduce the EMI by adding layers of conductors to the circuit

board. Dramatic reductions in the radiated emissions from a printed circuit board have been described by German *et al* [41]. See also Hardin *et al.* [47]. Visualizing the electromagnetic field on a circuit board with such an EMI-suppression device will be more difficult.

Note that there is an Air Force run "Electromagnetic Compatibility Analysis Center" at Annapolis, MD. Their mission is to ensure the DoD's effective use of systems in electromagnetic environments in support of national security and military objectives.

2.6 Circuit card parameters: present

The range of values that the current on a circuit board might be is very large. At the high end, the power lines for the DEC alpha chip draw 20 Watts at 5 Volts, so it requires 4 amps from the power supply. At the other extreme, TTL logic draws current in the range 2–16 milli-amps, and CMOS draws about 1 milli-amp of current. We are also believe that currents can, in some cases, be considerably smaller than 1 milli-amp.

In general, we expect there to be two major types of traces on a circuit board; traces carrying power and traces carrying signals. As seen above, the power traces may be carrying large currents. The signal traces will be more difficult to detect, since the currents they carry are much smaller. This report will focus on the visualization of these small current, signal traces. Any conclusions regarding the detection and imaging of these signal traces also applies to the power traces.

It may be thought that the power traces will dominate the signal traces, and preclude the signal traces from being visualized, but this is not correct. We can make a simple estimate of how much the power traces could affect the visualization of the signal traces. The magnetic field produced by a line current varies as (see section 3.4.1) current divided by distance. Assuming the values

- power trace: current of $I_p = 4$ amps, distance of $h_p = 2$ cm
- signal trace: current of $I = 0.02$ amps, distance of $h = 2$ mm (both vales taken from table 5)

then the ratio of the two effects is

$$\text{ratio of signal magnetic field to power magnetic field} = SNR = \frac{I_p/h_p}{I/h} = 0.0125$$

Thus, one might conclude that, with the given distances and currents, the signal trace is dominated by the power trace. This is correct, but only at DC. The high power traces will, in principle, be constant (DC) current, while the low-power traces will be at a much higher frequency (perhaps as high as 100 MHz). Hence, if the power trace is carrying a DC current to 1 part in 10^3, then the above ratio improves to $R = 12.5$ at frequencies away from DC.

There is also an issue of common-mode and differential-mode currents. For common-mode currents, two nearby, nearly parallel wires, carry current in the same direction. For differential-mode currents, the wires carry currents in opposite directions. The electromagnetic fields radiated from these cases are radically different; they are substantially smaller for differential-mode currents.

2.7 Circuit board parameters: future

An idea of the future parameters of circuit boards can be obtained by looking at the design limitations of the CAD tools presently used to design circuit boards. The limitations of the TangoPro package are shown in table 4. The "clearances" entry is the amount of space that the software should leave between one pad, line, or via to another pad, line, or via.

Automatic routers are software programs that determine the layout of a circuit board, from an initial approximation. There are many routing packages available. QuickRoute has 5 pre-defined grid settings, one of which is 17 mil (which is also the minimum allowable separation between adjacent traces).

2.8 Testing circuit boards

There are many ways that circuit cards have been tested. A review of new testing equipment is in Balme *et al.* [8]. Test equipment is usually described as being either universal (capable of being applied to many different circuit boards) or dedicated (specialized for a specific circuit board).

Parameters	Restriction
Clearances	12 mil (default value)
Grid spacing	minimum: 0.1 mil
Trace width	minimum: 0.1 mil, typical: 10–25 mil, maximum: 1 cm

Table 4: Restrictions of TangoPro circuit board layout package

From Clark [21, page 157] we find that

> "Universal electrical testers have made it possible to test economically every job being built in the shop—even the smallest prototype quantities."

and

> "Compared to dedicated equipment, the universal tester is slow."

and

> "Testing speed is limited mostly by how rapidly the operator can lift a lid, place a printed circuit on it, and close it. For this reason, when large quantities are involved, the more costly dedicated test fixture is built."

We note that Langley *et al.* [60] contains the very succinct statement about the allowable time for testing a board with surface mount devices on it (italics added):

> "SMB displacement and intensity variations could not be reliably detected by the ATE operator and a *total test time of two and a half minutes was unacceptable*"

We note that many new types of testing equipment are being developed, from Pearson [83]

> "Several non-contact test techniques for the testing of PCBs in addition to the traditional methods have been introduced in recent years. These include infrared thermography, ultrasonics, visual enhancement, and E-field."

There is a large market for automatic test equipment (ATE). In [2] it was stated that the 1994 worldwide market is more than $5 billion, and the worldwide market in the year 2000 is projected to be more than $7 billion. The percentage of this market that the United States has was 44% in 1993; it is expected to be 39% by the year 2000.

Bare board testing is restricted to detecting opens and shorts. The testing is easy to automate, and no fixtures are required. The most common technique of automated testing of bare boards is with "flying probes" (see the next section). It is also possible to test a circuit board after it has been populated with electronic components. While this may also be done with "flying probes" it is most frequently done by constructing dedicated test equipment. For example, GenRad's "Opens Xpress" works by sourcing an AC voltage to each lead of a device and them measuring the resulting voltage coupled through the device package. This voltage is sensed by a detector plate that is in direct physical contact with the device package. The actual measured values are learned from a known-good board, and thresholds are established on a pin-by-pin basis.

2.8.1 Existing methods

There are many current techniques used to test circuit boards:

- Flying probes

  These probes move to every net list on a board and check for shorts and breaks. The information required for the probes is contained in the original CAD description of the circuit board. Integratest (of Long Island, NY) sells a $100,000 device that uses 2 sets of probes. One tests for capacitance, the other tests for terminal resistance.

There are many other vendors selling probe systems for doing bare board testing. The product literature from Probot[7] indicates that their 6D model can test an SMT board with 3,500 test points and 650 nets in 10 minutes. The design data needed by this machine to create the test is either net lists, or a Gerber file (see section 2.2).

It is also possible to use flying probes to test populated circuit boards. The APT-8300 device is manufactured by Texmac[8], it has three probes and can test all analog components on a circuit board (including resistors, capacitors, inductors, diode/transistor junctions, etc) at speeds up to 0.06 second per test. The probe position repeatability is $\pm 50\mu$m, with a positioning resolution of 0.2mm. The GTL 4000 Series device is manufactured by GigaTest Labs[9], it is similar to the above device except that it is operated manually.

The flying probes are limited in their usefulness to frequencies below approximately 10 MHz.

- In-circuit testing

  An in-circuit test performs an individual test on each component of a populated board. Both digital and analog in-circuit tests may be performed by most advanced board test equipment. A digital in-circuit test is intended to find only component pin faults. An analog in-circuit test is intended to find out-of-tolerance passive analog components. The component under test is isolated from other components using multiple-wire guarding (for analog components) or backdriving (for digital components).

- Functional testing

  A functional test performs one or more digital tests, usually from the board edge connectors, on the entire board. A functional test is designed to find faults of a particular class, usually main level single stuck-ats. (Under this definition, a functional test is not intended to find analog faults.)

- Specification testing

  A specification test performs one or more tests, usually from the board edge connectors, on the entire board. The test is designed to accurately emulate the operational environment of the board and to measure various input/output parameters in an attempt to verify adherence to predefined specifications. The specifications describe the operational attributes of the board at the edge connectors and can encompass both analog and digital parameters.

- Boundary scan testing

  Boundary scan incorporates the use of special components which are linked together to allow access to the internal nodes of a pcb without the need to make physical contact through a bed of nails fixture.

- Bed-of-nails testing

  In this technique a board is precision drilled and outfitted with spring loaded electrodes that line up with the different nets on a circuit board. With the traditional bed of nails, it is only possible to electrically inspect PCB's for missing, misoriented and out of tolerance components. The bed of nails technique is limited in its frequency response to about 30 mega Hz, according to Teradyne.

- E-beam testing

  This refers to an electron beam substrate tester (EBST). The tester can be used to test multichip modules and fine line printed circuit boards for opens, shorts, and capacitance.

  The Advanced Electronics Technology Group at McClellan Air Force Base recently purchased an EDST from Alcedo, Inc. Their tester can test MCMs as large as 10 × 10 inches, with an active area of 8 × 8 inches to a resolution of 5 microns.

- Direct visualization Many groups have tried to optically inspect circuit boards using CCD cameras. See, for example, Silvén *et al* [101].

[7]Probot Incorporated, 36 East Industrial Road, Branford, Conn 06405
[8]Texmac Inc., 3106 Patrick Henry Drive, Santa Clara, CA 95054
[9]GigaTest Labs, 20480 Pacifica Drive, Cupertino, CA 95014

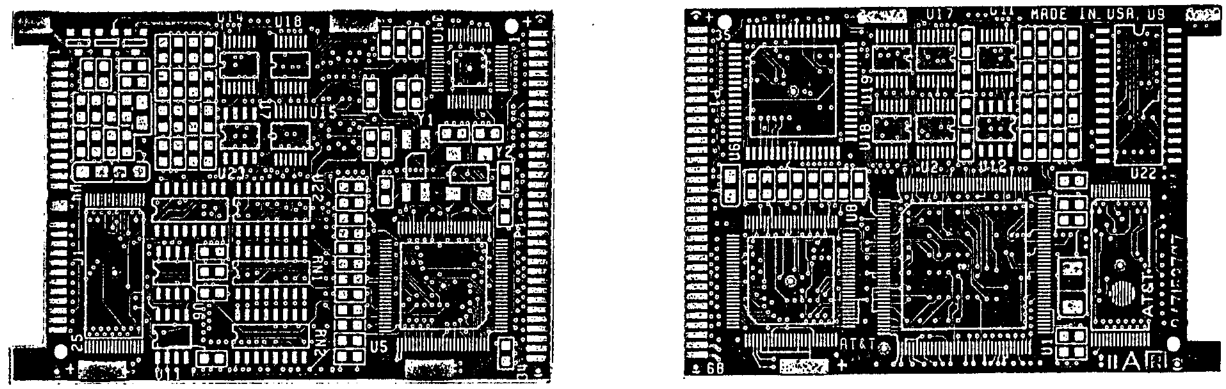

Figure 3: The front (left) and back (right) of a digital circuit board

2.9 Spectral distribution of electromagnetic energy on circuit boards

The electromagnetic fields near the traces on a circuit board will be confined to many well-defined narrow frequency ranges. For example, a circuit board operating at 100 MHz will have electromagnetic fields at this frequency, but it will also have fields at subharmonic frequencies (50 MHz, 25 Mhz, etc) and also at superharmonics frequencies (200 MHz, 300 MHz, etc). With a spectrum analyzer the energy present will appear up as lines on distinct frequencies.

If the energy in the electromagnetic field were dispersed uniformly across frequencies, then detection of that energy would be difficult to achieve, since the signal-to-noise ratio in any resolution bandwidth would be low. As noted above, circuit boards create electromagnetic fields only in certain narrow frequency ranges. A sampling system centered at one of these frequency will have a much improved signal-to-noise ratio within that resolution bandwidth.

2.10 Representative circuit boards

To obtain a realistic view of the scales present in circuit boards, we have included photocopies of a digital circuit board (see figure 3) and an analog circuit board (see figure 4). Both figures show the boards at true size. The digital circuit board is for a PCMICA card (a modem for a portable computer), it would have components on both sides. The analog circuit board is for a power supply, it would be populated with components on one side. Note that the analog board is a single rigid sheet while the digital circuit board is composed of 8 layers laminated together.

The smallness of the traces in figure 3 cannot be observed from the photocopy. A close inspection of figure 3 (front view, near the bottom right) will identify the label `U5`. Above this label is a horizontal stack of traces. Within the width of this stack are 10 vertical lines, on a single internal layer, which are not visible from the photocopy.

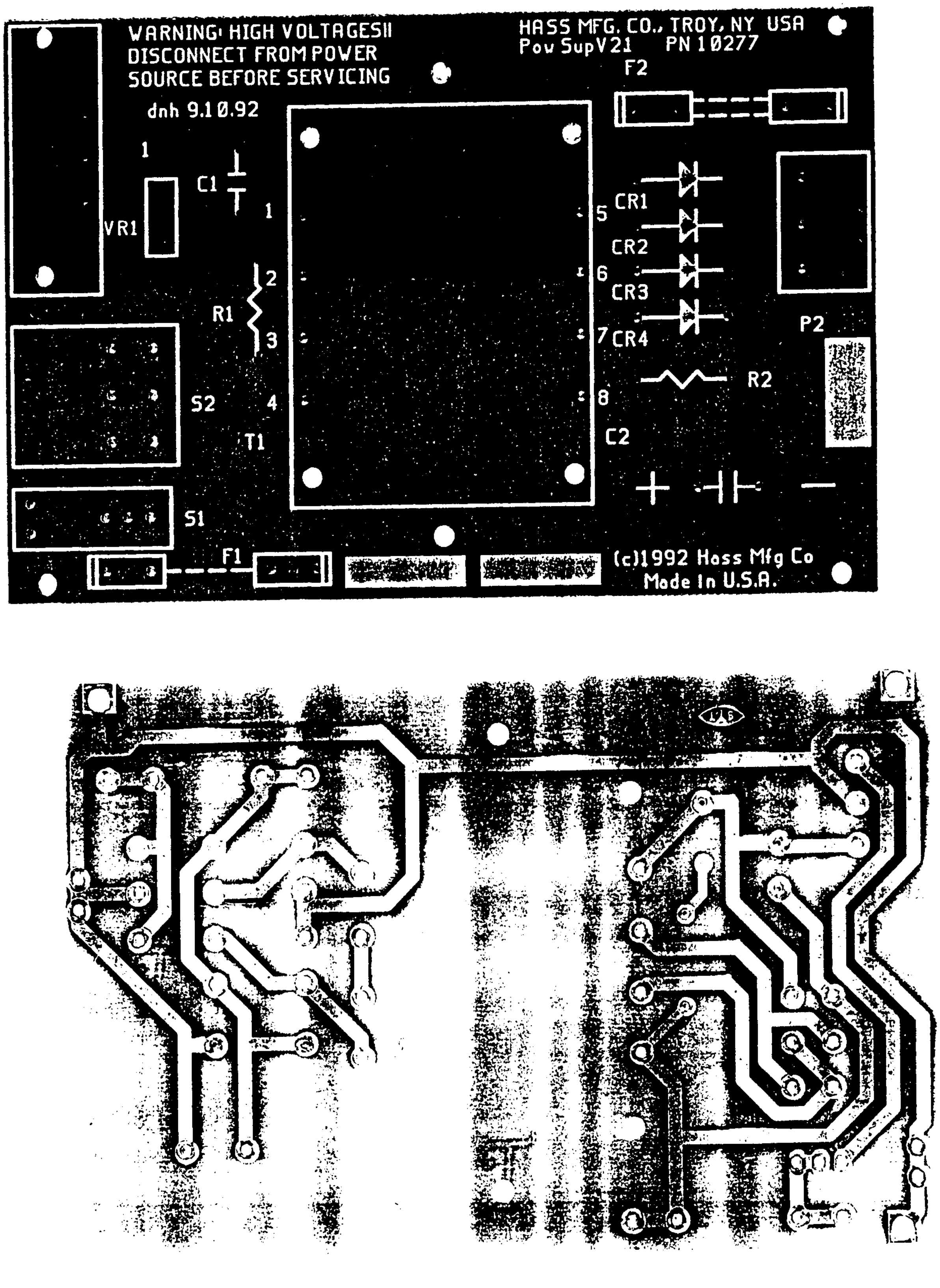

Figure 4: The front (top) and back (bottom) of an analog circuit board

3 Estimate of the Electromagnetic Fields on a Circuit Board

This section estimates the electromagnetic fields that may be obtained for a typical digital circuit board. For the geometry assumed in figure 5 (on page 21), with numerical values given by table 5 (on page 21), the conclusions are listed in table 7 (on page 27).

3.1 Estimation procedure

To simulate the performance of the techniques to be described in section 7, the behavior of the field surrounding a circuit card must be estimated. This involves numerically finding the solution of linear partial differential equations, as described in section 3.2.

There are many books describing different techniques (such as the finite difference method, the finite element method, the method of moments, etc) which may be employed to numerically solve the needed equations (see, for example, the books by Kunz and Luebbers [58] and Sadiku [92]). Additionally, there are also many commercial packages available that will numerically solve these equations, see section 3.3.

Many researchers have tried to determine specifically the radiated field from a printed circuit board, since this is needed for EMC and EMI studies. Sample results may be found in Daijavad *et al* [25], Walter [115], and Gabrielson [39]. This is a growing field, from Dixon *et al* [30]:

> "In the mechanics, structures, and fluids disciplines, numerical tools, such as finite-element analysis (FEA) have become commonplace in the designers toolkit. In electromagnetics (EM) such analysis tools are still in their infancy. Electromagnetic compatibility (EMC) analysis has been primarily limited to the analysis of simple equivalent circuit models or measurements of a completed design. Few reliable methods exist to predict the EMC of a complex system or group of systems before it leaves the designer's desk. Powerful electromagnetic software based on FEA techniques is now becoming commercially available."

One of the difficulties with simulations is that, at high switching speeds, even small small wires must be taken into account. From Wang [116] (recall that 500-ps oscillations correspond to 2 GHz):

> "When digital signals have a 500-ps rise time, conductors as short as 6.7 mm must be treated as a transmission line in the circuit simulation to ensure accurate results."

Hence, most often, EMI and EMC values are obtained experimentally. For example, German *et al* [41] experimentally investigated the radiated emissions from a printed circuit board with a digital circuit which produced current on a signal trace that returned via an adjacent ground-return trace.

All the commercial packages surveyed in section 3.3 are cumbersome to use for this project. When they have been designed to deal specifically with circuit boards, they generally determine the fields on a cylinder at distances of 3 meters and 10 meters from the board (which is needed to determine if the circuit board meets FCC restrictions).

Hence, in section 3.4 we have created and studied a simple problem for which we can estimate the electromagnetic fields produced. Embedded in the sample problem is the assumption that we are interested in low-frequency testing, which means that we are in the regime of quasi-static analysis. The sample problem uses two parallel infinite wires. While infinitely long wires are unrealistic in many scenarios, they are reasonable for our application. A wire of finite length "looks" infinite if it's length is more than some multiple of the distance to the wire (the multiple is commonly taken to be about 10.) From our table of nominal values (table 1 on page 9) the nominal height of the sensing sheet above the circuit board is 2 mm. Hence, any wire longer than about 20 mm (about 0.8 inch) that is directly below will appear to be infinite. While there are usually several wires on a circuit board shorter than this dimension, many wires are much longer than this dimension.

3.2 Mathematical background

Maxwell's equations describe all macroscopic phenomena involving electromagnetic fields. They may be written as:

$$\begin{aligned} \nabla \times \mathbf{E} &= -\frac{\partial \mathbf{B}}{\partial t} \\ \nabla \times \mathbf{H} &= \mathbf{J} + \frac{\partial \mathbf{D}}{\partial t} \\ \nabla \cdot \mathbf{B} &= 0 \\ \nabla \cdot \mathbf{D} &= q \end{aligned}$$

where $\mathbf{E}$ and $\mathbf{H}$ are the electric and magnetic fields, $\mathbf{D}$ and $\mathbf{B}$ are the electric and magnetic flux densities, $\mathbf{J}$ is the current density, and q is the volume charge density.

For a homogeneous medium, $\mathbf{D}$ and $\mathbf{B}$ are related to $\mathbf{E}$ and $\mathbf{H}$, respectively, by scalar constants: $\mathbf{B} = \mu\mathbf{H}$ and $\mathbf{D} = \epsilon\mathbf{E}$. In a source free region, both $\mathbf{J}$ and q are zero.

Any vector can be written as the sum of an irrotational vector and a solenoidal vector. For the case of the electric field, the solenoidal vector corresponds to a temporally changing magnetic field. In the quasi-static approximation, this solenoidal vector can be neglected. In this case, the electric field can be approximated by finding the voltage field V in the region above the the circuit board, and then computing $\mathbf{E} = -\nabla V$. To determine the voltage field, we recall that the voltage field satisfies Laplace's equation in any source-free region (see, for example, Halliday and Resnick [46]), and the voltage on the traces gives the boundary conditions for V.

3.3 Available computer tools

Many articles appear in the literature describing ways in which to compute electromagnetic fields. See, for example, the recent articles by Kamel [51], Laroussi and Costache [62], Mur [74], Piriou and Razek [85], and Trabelsi [107]. There are also several commercial finite element EM solver packages on the market. Some of the packages can accept as input the CAD design of a circuit board in any of several different formats. Prof R. Nelson[10] of North Dakota State University, found the following as regards to CAD support for finite element programs.

- EMAS (The MacNeal–Schwendler Corporation, 4300 W. Brown Deer Road, Milwaukee, Wisconsin 53223)
  - Will accept IGES[11] files.
  - Is working on a direct link with Pro/ENGINEER, Unigraphics, CAEDS and INTERGRAPH.
- Maxwell EM 2D Field Simulator, Maxwell EM 3D Field Simulator, Maxwell SI Eminence (ANSOFT Corporation, Four Station Square, Suite 660, Pittsburgh, PA 15219-1119)
  - He thinks they will accept IGES files.
  - Direct link is available with SDRC (Structural Dynamics Research Corporation).
- MARC
  - Will accept IGES files.
  - Direct link available with INTERGRAPH, PATRAN and SDRD.
- PC-OPERA, OPERA-2d, ELEKTRA, TOSCA, and SOPRANO (Vector Fields, Inc. 1700 N. Farnsworth Avenue, Aurora, IL 60505)
  - Will not accept IGES files.
  - Direct link with I-DEAS and Pro/ENGINEER.

[10] Personal communication while Dr. Nelson was consulting at NIST in 1994.

[11] IGES is a public-domain data specification intended as an international standard of information between CAD systems. A full description of IGES may be found in *The Initial Graphics Exchange Specification (IGES) Version 5.1*, U.S. National Computer Graphics Association.

  - Plans to extend this to CATIA.
- ANSYS (ANSYS, Inc., 201 Johnson Road, Houston, PA 15342-1300)
  - Will accept IGES files.
  - Direct link with Pro/ENGINEER.
  - Plans to extend this to Unigraphics, AutoCAD and others.

There are many other commercial EM packages, such as:

- ESTART (Structural Research & Analysis Corporation, 2951 28th Street, Siote 1000, Santa Monica, CA 90405)
- Algor (Algor, Inc., 150 Beta Drive, Pittsburgh, PA 15238-2932)
- Amperes and Coloumb (Integrated Engineering Services, Inc., 347-435 Ellice Avenue, Winnipeg, Manitoba, Canada R3B 1Y6
- COMPLIANCE and BOARDSPECIALIST PLUS (Quantic Laboratories Inc., 12th Floor, 191 Lombard Avenue, Winnipeg, Canada, R3B 0X1)
- XFX3D and QUIET (Quad Design, 1385 Del Norte Road, Camarillo, California 93010)

as well as packages produced by

- Electromagnetic Applications, Inc., PO Box 260263, Denver, Colorado 80226-2091
- Phillips in Antwerpt, Netherlands
- Teledyne Brown Engineering, Electro-Optics Products Group, PO Box 070007, Huntsville, Alabama 35807-7007

Research continues on the best way to combine a Maxwell's equation with circuit analysis software. Richard Holland of Shield Rite, Inc.[12] was recently awarded an Air Force Phase I SBIR contract (number F29601-93-C-0047 for topic 93-077) for work with the title "Integration of Maxwell-solving and Circuit Analysis Software". The abstract of this work is:

> "Contractor will explore techniques for combining EM coupling code and circuit analysis code to determine transfer functions from fast-pulse HPM threats to circuit-component responses. Techniques must be general enough to consider pulse rise time, total energy, and duration. Treatment must be general enough to work for aircraft, sensor pods, missiles, and satellites. Coupling through antennas, sensors, leaky gaskets, and hatches must be permitted. Contractor proposes to treat the exterior coupling, the RF points of entry, the internal RF response, the internal RF coupling to cables and circuits, and the circuit response as associated, but mostly separate, problems, although the last two aspects probably require simultaneous treatment. Feasibility studies will be made for different approaches to each of these five sub-problems. At present, our inclination is that the external problem may be treated deterministically, but the internal response can only be treated statistically."

3.4 Estimate of the electromagnetic fields for a simple geometry

Consider two parallel wires ($m = 1$ and $m = 2$), carrying currents of $i_m(t)\mathbf{k}$ (in amps), having voltages of V_m (in Volts). These wires are separated by a distance d. The plane of the sensing sheet is parallel to the plane of the wires, and it is a distance h from the wires. See figure 5 for an illustration of the geometry. Note that the vector $\mathbf{k}$ is coming out of the page.

Let $\mathbf{x} = x\mathbf{i} + h\mathbf{j}$ be a specific location on the sensing sheet (the origin of the coordinate system is taken to be midway between the two wires, on the circuit board). We define r_m to be the radial distance from wire m to $\mathbf{x}$, and θ_m to be the angle subtended. Algebraically we determine r_m and θ_m to be:

$$\begin{aligned} r_1 &= \sqrt{(x-d/2)^2 + h^2} & \qquad r_2 &= \sqrt{(x+d/2)^2 + h^2} \\ \theta_1 &= \tan^{-1}\left(\frac{x-d/2}{h}\right) & \qquad \theta_2 &= \tan^{-1}\left(\frac{x+d/2}{h}\right) \end{aligned}$$

[12]Shield Rite, Inc., PO Box 8250, Albuquerque, NM 87198

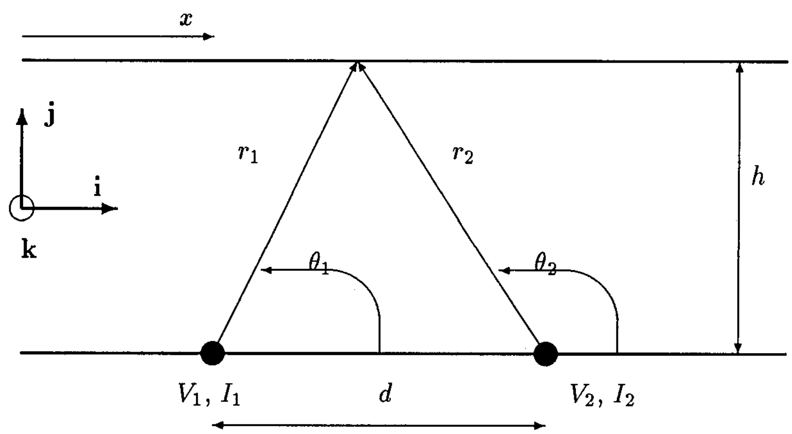

Figure 5: Simple geometry of wires above ground plane (plane not shown)

height of sensing sheet above circuit board	$h = 2$ mm
operating frequency	$\omega = 1000$/sec
current in trace 1	$I_1 = 0.020$ amperes
current in trace 2	$I_2 = \pm I_1$
voltage[a] on trace 1	$V_1 = 2.5$ Volts
voltage on trace 2	$V_2 = \pm V_1$
trace separation	$d = 0.10$ inch
height of trace about ground plane (for **E** field)	$\beta = 0.5$ mm
radius of trace (for **E** field)	$r_0 = 0.2$ mm
characteristic impedance[b]	$Z_0 = 100\Omega$

Table 5: Assumed parameters for simple geometry model

[a]Half the time the signal will be 5 Volts, half the time the signal will be 0 Volts
[b]This value may be useful for reference, it comes from $Z_0 = 60\cosh^{-1}(\beta/r_0)$, see [1].

In section 2.6 we discussed the different possible currents on a circuit board. When we evaluate numerical results in this chapter, we use the nominal values in table 1 (on page 9) and the values specified in table 5 (on page 21).

- Magnetic field computation

  This is determined exactly by the techniques described in section 3.4.1.

  For our nominal values, we find the magnetic field at the sensing sheet to be as shown in figure 6 for common-mode current (i.e., when $I_2 = I_1$) and figure 7 for differential-mode current (i.e., when $I_2 = -I_1$). The graph with the keyword B_y denotes the field perpendicular to the sensing sheet; the keyword B_x denotes the field in the plane of the sensing sheet, orthogonal to the plane of the wires. That is, $B_y = \mathbf{B} \cdot \mathbf{j}$ and $B_x = \mathbf{B} \cdot \mathbf{i}$. We also define $B = \sqrt{B_x^2 + B_y^2}$.

- Electric field computation

  This is approximated by the techniques described in section 3.4.2.

  For our nominal values, we find the electric field at the sensing sheet to be as shown in figure 8 for common-mode current (i.e., when $V_2 = V_1$) and figure 9 for differential-mode current (i.e., when $V_2 = -V_1$). The graph with the keyword E_y denotes the field perpendicular to the sensing sheet; the keyword E_x denotes the field in the plane of the sensing sheet, orthogonal to the plane of the wires. That is, $E_y = \mathbf{E} \cdot \mathbf{j}$ and $E_x = \mathbf{E} \cdot \mathbf{i}$. We also define $E = \sqrt{E_x^2 + E_y^2}$.

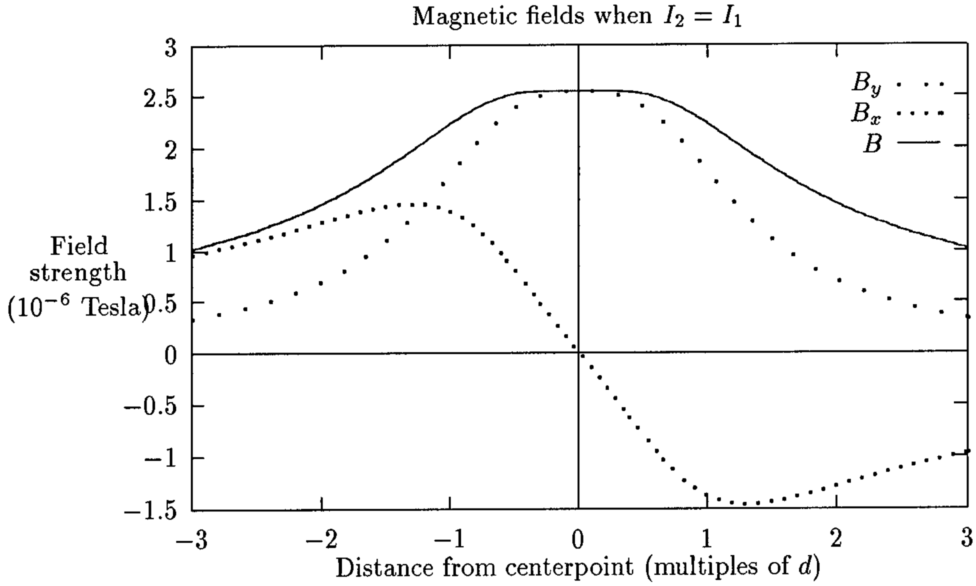

Figure 6: Nominal values of the magnetic field for common mode

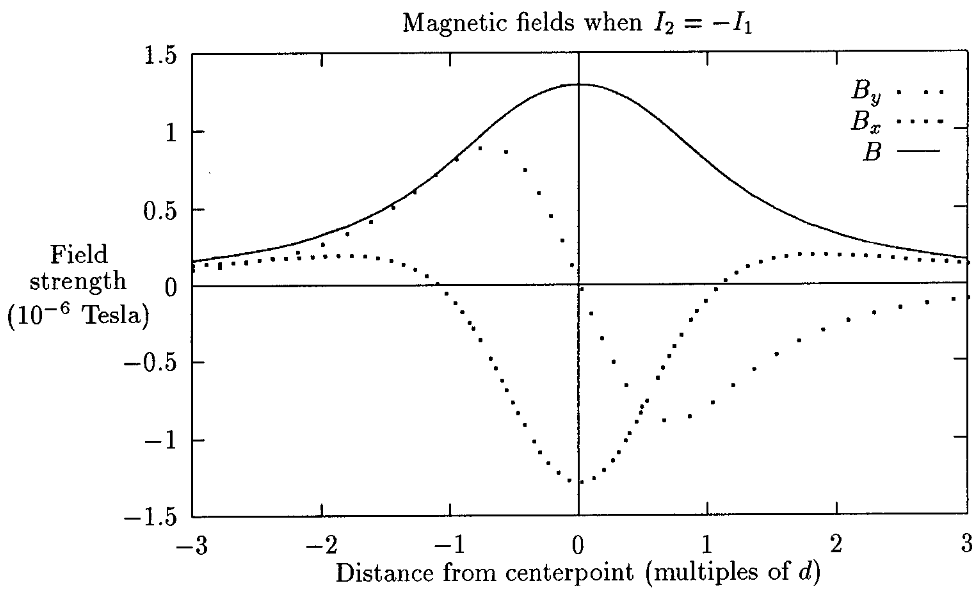

Figure 7: Nominal values of the magnetic field for differential mode

3.4.1 Estimate of the magnetic field

The magnetic field associated with wire m is found from classical physics (see Halliday and Resnick [46, equation 34–4]) to be $\mathbf{B}_m = B_m\hat{\theta} = B_m(-\sin\theta_m\mathbf{i} + \cos\theta_m\mathbf{j})$, where $B_m = \mu_0 i_m/2\pi r_m$.

We have presumed that the sensing sheet is not a conductor. If it were (as in the electrodynamic technique) then the $\mathbf{B}$ field may be affected by the presence of this conductor.

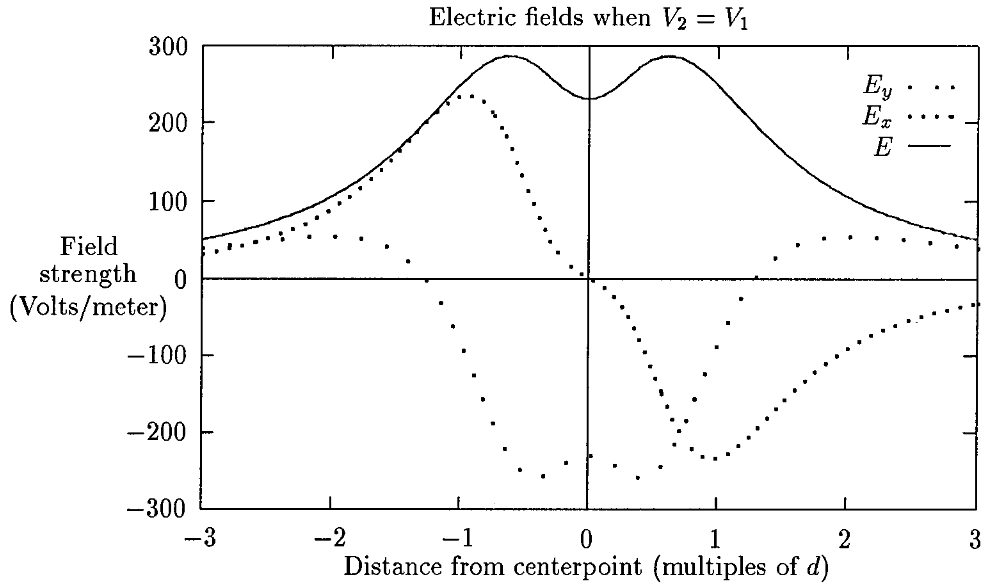

Figure 8: Nominal values of the electric field for common mode

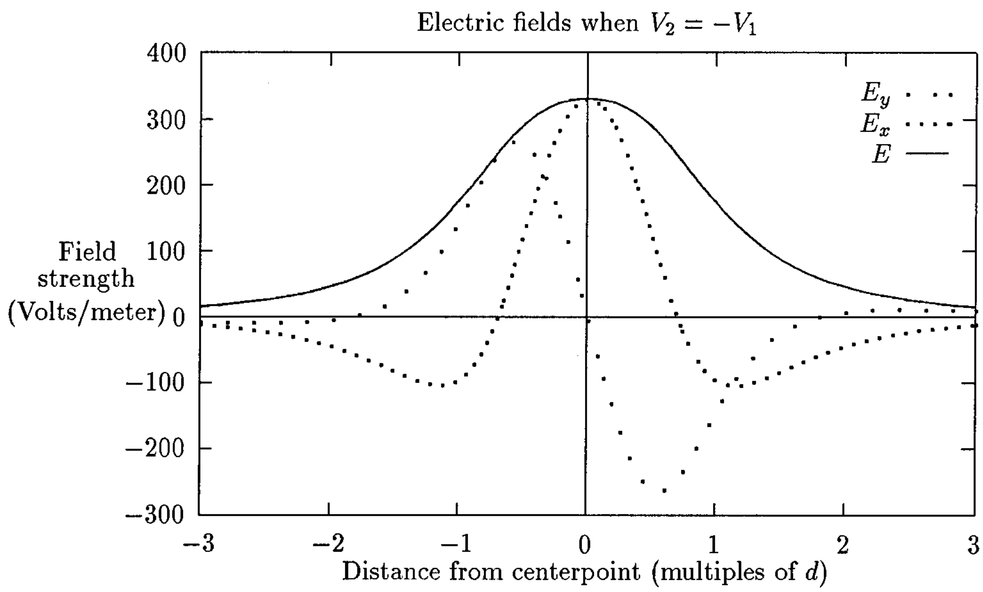

Figure 9: Nominal values of the electric field for differential mode

3.4.2 Estimate of the electric field

In this section we estimate the electric field by using superposition with the method of images. This method was used to create figures 8 and 9 (recall that voltages on the traces are V_m Volts, and the voltage on the circuit board is 0 Volts). Note that there are several ways in which the exact solution (with no approximations) can be obtained; see, for example, the method using bipolar coordinates (see page 81) and the method using elliptic functions and conformal mappings (see page 81). These exact techniques suffer from computational complexity and a resulting loss of physical insight.

To obtain our approximation, we will need to make further assumptions about the geometry of the circuit

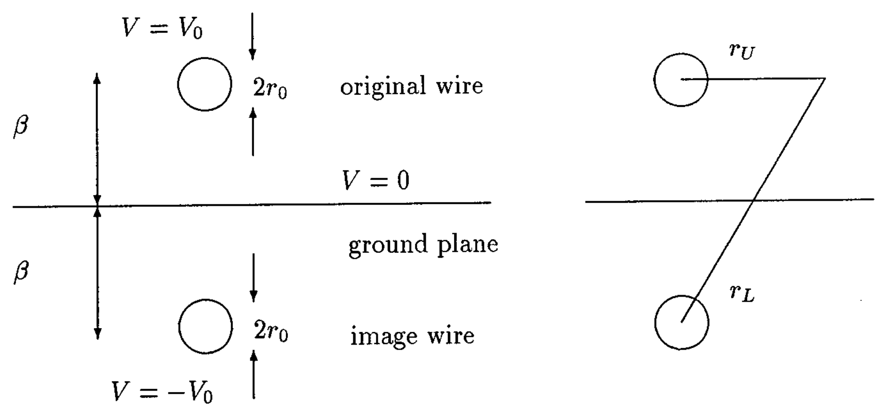

Figure 10: A wire and the image wire that simulates the ground plane

board traces. We now assume that each of the circuit board traces is a circular wire with a radius of r_0. Consider an isolated circular wire located above a ground plane (a plane where $V = 0$) by a distance β. It is known that the fields that are the solution to this problem can be generated by an image solution. That is, another wire on the other side of the location of the ground plane and equally spaced from it as the wire above carries an equal but opposite current and an equal but opposite voltage. If the potential on the single wire is V_0, then the entire effect of the ground plane can be replicated by placing an image wire[13] at a height β below the plane, with a potential of $-V_0$. The geometrical configuration is shown in figure 10.

The fields produced by the wire and it's image satisfy the boundary condition imposed by the ground plane, and therefore these fields are the solution of the problem. Because of antisymmetry of the voltages, the voltage anywhere at the location of the ground plane is zero. The lowest mode of this system happens to correspond to a transverse electromagnetic mode (see Stratton [104]). This is a mode in which the electric and magnetic fields are always perpendicular to the wire. In the plane perpendicular to the wire the fields satisfy Laplace's equation. All effects associated with the curl occur in the direction along the wire. In fact, the fields all propagate at the speed of light along the wire, but in the perpendicular cross-section they "look like" static fields.

To motivate the final solution for a wire and it's image companion in equation 3, consider first the case of a single trace and no image trace. Recall that the solution to Laplace's equation, $\nabla^2 V = 0$, around a single wire at constant potential ($V(r = r_0) = V_0$) is, in cylindrical coordinates,

$$V = a + b \log(r/r_0) \tag{1}$$

where a are b are constants to be determined. To have boundedness as $r \to \infty$ we require $b = 0$. To match the boundary conditions at $V(r = r_0)$ we require $a = V_0$. Hence, $V = V_0$ everywhere.

We will now find an approximation to the solution to Laplace's equation for a wire and it's image wire. We begin with an exact solution to Laplace's equation for a wire and it's image wire, with one term for each wire (analogous to equation 1):

$$V = a + b \log \frac{r_U}{r_0} + c \log \frac{r_L}{r_0} \tag{2}$$

where r_U is the distance from the original (upper) wire and r_L is the distance from the image (lower) wire (see figure 10). To have boundedness of V as $r \to \infty$, we require $c = -b$. To have the voltage zero on the ground plane, which is specified by $r_U = r_L$, we require $a = 0$. To determine the last constant we approximate the boundary conditions on the traces themselves.

On the upper trace, where $r_U = r_0$ and $r_L \approx 2\beta$, we have $V = V_0$. Using this approximation we determine

[13]The method of images is described in Zwillinger [123].

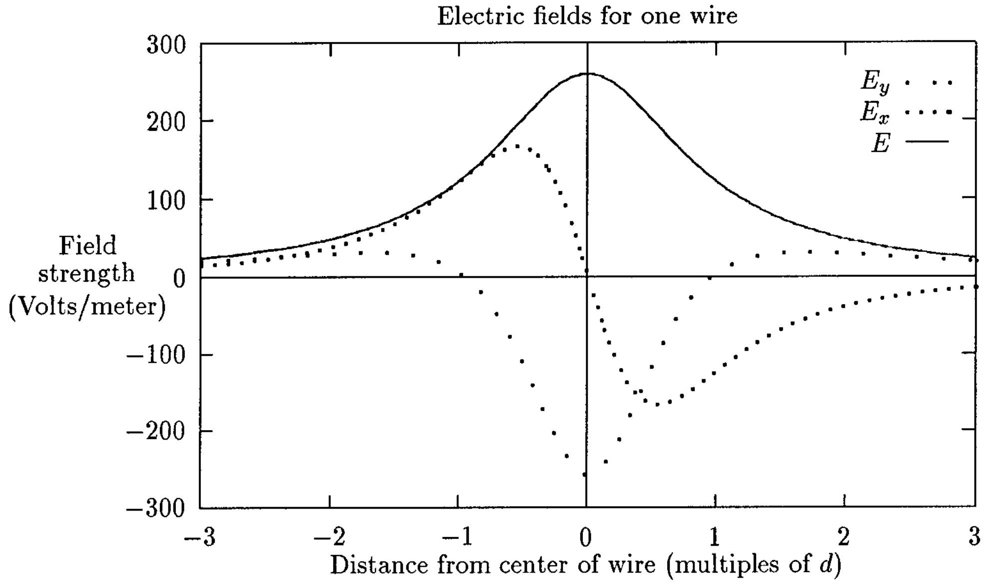

Figure 11: Nominal values of the electric field for a single wire

the last constant in equation 2 to be $b = V_0/\log(r_0/2\beta)$. Hence, the final solution is given by

$$V \approx V_0 \frac{\log\left(\frac{r_U}{r_L}\right)}{\log\left(\frac{r_0}{2\beta}\right)} = \frac{V_0}{\log\left(\frac{r_0}{2\beta}\right)}(\log r_U - \log r_L) \tag{3}$$

Note that the boundary condition on the lower trace, where $r_L = r_0$, $r_U \approx 2\beta$ and $V = -V_0$, is satisfied to the order of our approximation.

If we represent a point in space with the coordinates $\mathbf{x} = x\mathbf{i} + y\mathbf{j} + z\mathbf{k}$, and define the ground plane to be specified by $y = 0$, then we find

$$r_U = \sqrt{(y-\beta)^2 + x^2} \qquad r_L = \sqrt{(y+\beta)^2 + x^2}$$

Using $\mathbf{E} = -\nabla V = E_x\mathbf{i} + E_y\mathbf{j} + E_z\mathbf{k}$ we obtain

$$E_x = -\frac{\partial V}{\partial x} = -\frac{V_0}{\log\left(\frac{r_0}{2\beta}\right)} x \left[\frac{1}{r_U^2} - \frac{1}{r_L^2}\right] \qquad E_y = -\frac{\partial V}{\partial y} = -\frac{V_0}{\log\left(\frac{r_0}{2\beta}\right)} \left[\frac{y-\beta}{r_U^2} - \frac{y+\beta}{r_L^2}\right]$$

$$E_z = -\frac{\partial V}{\partial z} = 0 \tag{4}$$

The expression $E_z = 0$ indicates that the field does not change in the $\mathbf{k}$ direction. Using equation 4 with the values in table 5 we have computed the electric field for a single wire (see figure 11)

Using the above results, we can now consider the case of two wires above the circuit board. We assume that the plane of these two wires is parallel to a ground plane, fixed at $V = 0$. The geometry of the situation, two wires and two image wires, is as shown in figure 12. Using superposition, the voltage field is then approximated as

$$V = V_1(\log r_{U,1} - \log r_{L,1}) + V_2(\log r_{U,2} - \log r_{L,2})$$

where the subscripts of "1" and "2" correspond to the two different wires. If we once again (1) represent a point in space with the coordinates $\mathbf{x} = x\mathbf{i} + y\mathbf{j} + z\mathbf{k}$, (2) define the ground plane to be specified by $y = 0$ (as before), and (3) define the x origin to be midway between the original wires, then we find

$$r_{U,1} = \sqrt{(y-\beta)^2 + (x-d/2)^2} \qquad r_{U,2} = \sqrt{(y-\beta)^2 + (x+d/2)^2}$$
$$r_{L,1} = \sqrt{(y+\beta)^2 + (x-d/2)^2} \qquad r_{L,2} = \sqrt{(y+\beta)^2 + (x+d/2)^2}$$

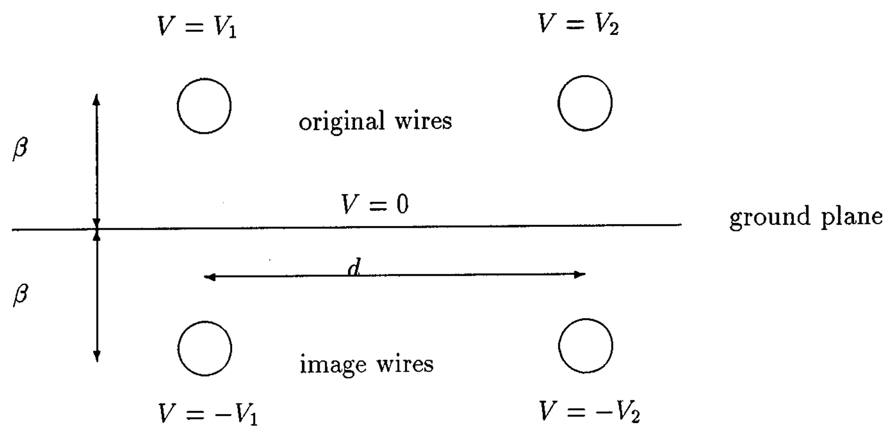

Figure 12: Geometry of two original wires, two image wires, and ground plane

height of sensing sheet above circuit board	$h = 5$ mm $= 0.5$ cm

Table 6: Modified parameters used in sensitivity analysis

From this we compute $\mathbf{E} = -\nabla V = E_x\mathbf{i} + E_y\mathbf{k} + E_z\mathbf{j}$ to be

$$\begin{aligned}
E_x &= -\frac{V_1}{\log\left(\frac{r_0}{2\beta}\right)}\left(x - \frac{d}{2}\right)\left[\frac{1}{r_{U,1}^2} - \frac{1}{r_{L,1}^2}\right] - \frac{V_2}{\log\left(\frac{r_0}{2\beta}\right)}\left(x + \frac{d}{2}\right)\left[\frac{1}{r_{U,2}^2} - \frac{1}{r_{L,2}^2}\right] \\
E_y &= -\frac{V_1}{\log\left(\frac{r_0}{2\beta}\right)}\left[\frac{y-\beta}{r_{U,1}^2} - \frac{y+\beta}{r_{L,1}^2}\right] - \frac{V_2}{\log\left(\frac{r_0}{2\beta}\right)}\left[\frac{y-\beta}{r_{U,2}^2} - \frac{y+\beta}{r_{L,2}^2}\right] \\
E_z &= 0
\end{aligned} \tag{5}$$

For the parameters appearing in table 1, and defining $E_y = \mathbf{E}\cdot\mathbf{j}$ and $E_x = \mathbf{E}\cdot\mathbf{i}$, equation 5 was used to obtain the electric fields as shown in figures 8 and 9.

3.5 Sensitivity analysis: sensing sheet displacement

As a simple estimate of how sensitive the distance from the circuit board to the sensing sheet is, we recomputed figures 6–9 with the modified values in table 6. The results are shown in figures 13–16.

These comparison figures show that both the electric field and magnetic field decrease rapidly when the sensing plate is further from the circuit board than our baseline computation has presumed. These results are used in the following section.

3.6 Conclusions regarding estimated electromagnetic fields

From the estimates given in the preceding sections, we conclude that the sensitivity required for imaging a low power circuit board is as shown in table 7; the last column of this table in used for comparison purposes in section 7). Note that few boards (although an increasingly large fraction) are designed to minimize common-mode radiation by using differential-mode radiation.

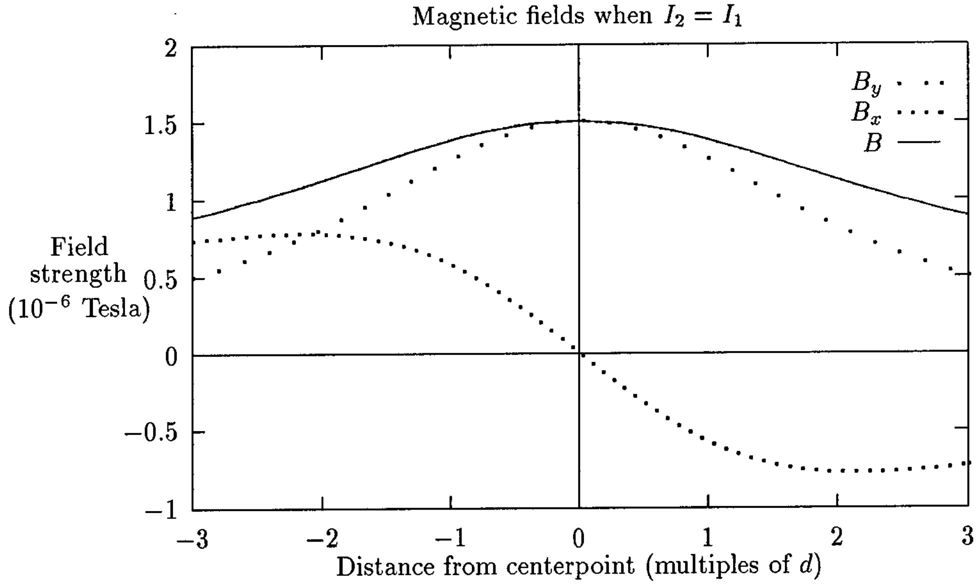

Figure 13: Nominal values of the magnetic field for common mode (modified values)

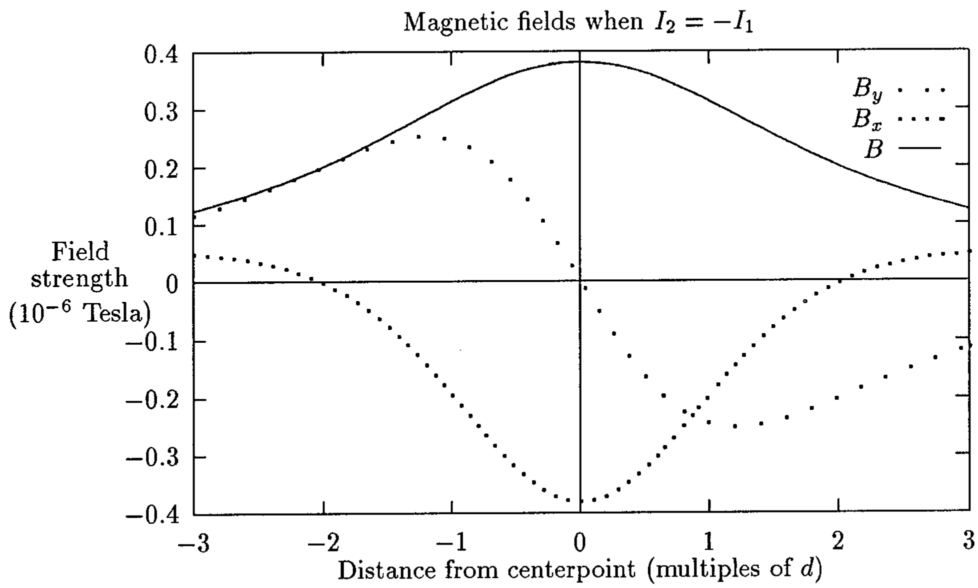

Figure 14: Nominal values of the magnetic field for differential mode (modified values)

	Common mode	Differential mode	One wire	Value used in comparisons
Magnetic field	1.0×10^{-6} Tesla	0.4×10^{-6} Tesla	0.5×10^{-6} Tesla	0.5×10^{-6} Tesla
Electric field	100 Volts/m	50 Volts/m	100 Volts/m	100 Volts/m

Table 7: Required detection sensitivity for imaging a low power digital circuit board

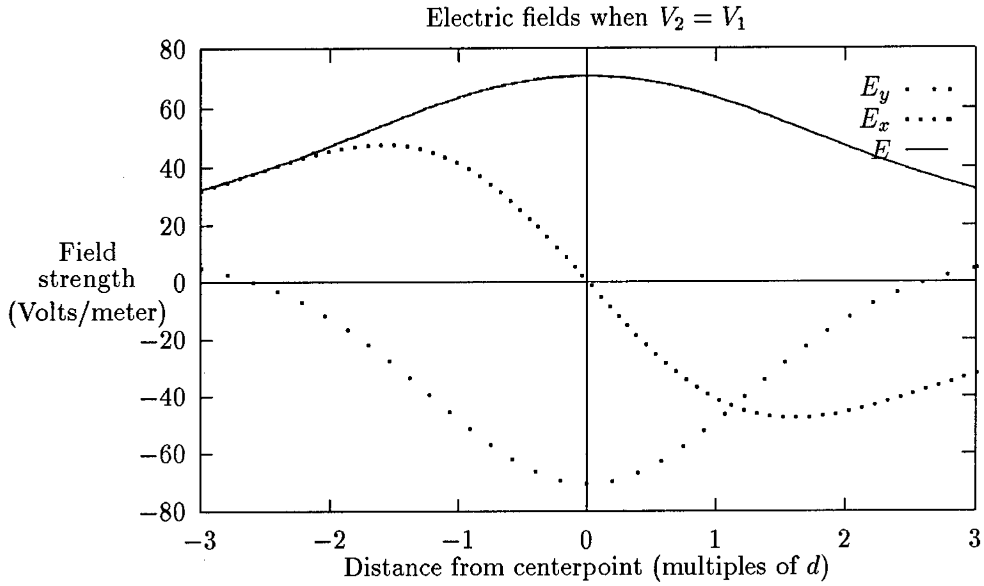

Figure 15: Nominal values of the electric field for common mode (modified values)

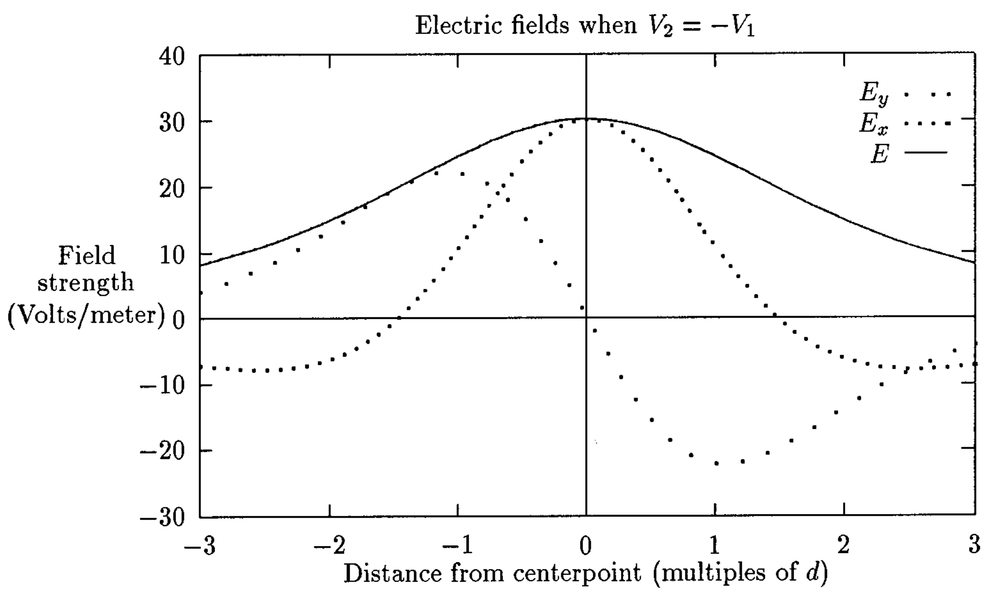

Figure 16: Nominal values of the electric field for differential mode (modified values)

4 Existing Electromagnetic Field Sensors

While there are many techniques which can be used to test circuit boards (see, for example, section 2.8), a natural technique is to directly measure the radiated electromagnetic field, which is the technique this report also studies. This requires that an electromagnetic field sensor be constructed which is appropriate for our currents and frequencies. Previous electromagnetic field sensors have used a variety of techniques:

- arrays of FETs (field effect transistors) (see section 4.1)
- arrays of Hall effect devices (see section 4.2)
- arrays of loop antennae (see section 4.3)
- electrooptical materials (see section 4.4)
- electrostrictive materials (see section 4.5)
- liquid crystals (see section 4.6)
- magnetic force microscopy (see section 4.7)
- magnetooptical materials (see section 4.8)
- magnetostrictive materials (see section 4.9)
- piezomagnetometer technique (see section 4.10)
- superconducting techniques (see section 4.11)
- thermal techniques (see section 4.12)

Several of these sensors have only recently been developed. This chapter describes these different techniques.

4.1 Arrays of FETs

A field effect transistor (FET) (see Dorf [31, pages 462–464]) can, in our application, be thought of as a semiconductor antenna similar to the antennae used in EMSCAN (see section 4.3). The ambient electric field can, if large enough, cause the FET to transmit a current. Hence, interrogation of the FETs will reveal information about the ambient electric field. Recent United States patents awarded for developments in this area include:

- Patent 5,182,624 was awarded for the invention of "Solid state electromagnetic radiation detector FET array" on 26 January 1993. This device is described as a "real-time detector," but the read-out time of the detector varies from one to four seconds.

- Patent 5,273,910 was awarded for the invention of "Method of making a solid state electromagnetic radiation detector" on 28 December 1993. This device can have approximately 4,000,000 pixels with densities up to 250,000 pixels/cm^2. In an example described in the patent, the gate voltage was adjusted for optimal sensitivity between -5 and 15 Volts. For a thin array, this leads to a large electric field. We believe that this device is only capable of measuring large electric fields.

- Patent 5,285,069 was awarded for the invention of "Array of field effect transistors of different threshold voltages in same semiconductor integrated circuit" on 8 February 1994.

4.2 Arrays of Hall effect devices

The Hall effect is a phenomenon that arises when an electric current and a magnetic field are simultaneously applied on a conducting material (see Dorf [31, chapter 49]). If a flat plate conductor has a current J in the x-direction and is exposed to a magnetic field B in the z-direction, then there will be a current E in the y-direction of magnitude RJB where R is known as the Hall coefficient. One such Hall effect device is described in United States patent 4,737,710. This patent was awarded for the invention of "Hall-effect array for sensing second spatial derivatives of magnetic fields" on 12 April 1988.

4.3 Arrays of loop antennae

The EMSCAN[14] (which stands for ElectroMagnetic SCANner) device, marketed by Amplifier Research,[15] is a tool which measures the near-field magnetic field under an active circuit board. The measurement panel consists of an array of 40×32 loop probes built into a 16 layer circuit board. Each loop probe is individually addressable via the IEEE488 bus, and the received signals are measured using a spectrum analyzer. The switching of the probes and the spectrum analyzer are controlled by a PC. The probes in the array are on 0.3" centers.

The EMSCAN measures the RF current levels existing on a functioning circuit board. This measurement provides a spatial resolution of the RF current levels across the entire board by measuring the near-field magnetic fields using an array of loop probes. Naturally, the presence of the measurement probes changes the RF current. Archambeault [4] claims this effect can be compensated.

EMSCAN is an electromagnetic emissions analysis and engineering tool used by design, support, and manufacturing personnel in evaluating printed circuit packs for EMC performance. It does this by measuring the near-field magnetic flux changes from the circuit board due to RF currents flowing in the pack and displaying this as a "signature" or spatial map of the emissions by color intensity. This is a table top sensor which non-invasively performs measurements. The unit can determine a frequency versus amplitude plot of emissions from a printed circuit board and an x, y coordinate map of the board's surface current distribution at a given frequency. It retails for about $50,000.

The EMSCAN unit is a fully controllable automated measurement system comprising three elements

1. The antenna board (sensor)
   This contains the antenna array and the control logic. It is manufactured by Bell Northern Research (BNR) of Canada.
2. The measuring system
3. The control and display software

Technical information on EMSCAN includes the following:

- Frequency response: 10 MHz to 750 MHz
  - The sensitivity increases at a rate of about 4dB per octave from 10 MHz to 100 MHz, and at about 2.5 dB per octave thereafter.
  - The lower frequency limit is caused by the noise threshold of the system.
  - The upper frequency limit is caused by a transmission line resonance at around 800 MHz.
- Sensitivity: 1 μAmp of current generates a voltage of 0.5 μVolts in the probe at 100 MHz when the device separation is less than 2.5 mm.
- Interface: IEEE - 488C (GPIB)
- Isolation: 30–35 dB (probe to probe)
- Number of probes: 1280
- Probe to probe spacing: 7.6 mm (0.3")
- Probe to probe sensitivity is ± 3 dB
- Scanning area: 304.8 mm (12") $\times$ 243.8 mm (9.6")

The short note by Previti [86] indicates that, with their configuration, it took one minute per scan (when using all 1280 probes). Archambeault [4] provides a good description of the device. He notes that "EMSCAN measures the current flow over the probe array but provides no information on current direction or phase."

The main drawback we have identified for EMSCAN, which is sold commercially, is that the resolution is only 0.3 inches between sensors. This is very large distance when compared to modern digital circuit boards traces (see, for example, figure 3). Increasing the resolution of the EMSCAN device would appear to be very expensive.

[14] EMSCAN is a registered Trademark of EMSCAN Corporation
[15] Amplifier Research, 160 School House Road, Souderton, PA 18964-9990

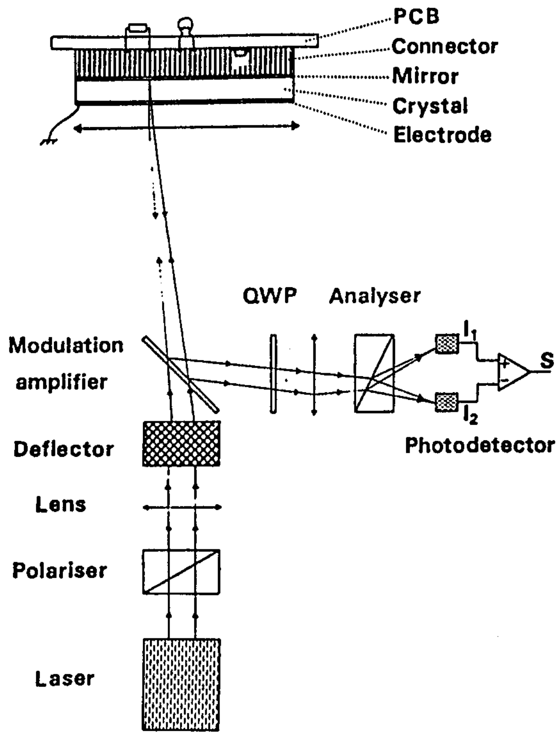

Figure 17: The experimental arrangement of Tremblay *et al.* [109]

4.4 Electrooptical field sensors

There are numerous papers describing electrooptical sensors designed to measure large electric fields. See, for example Massey *et. al* [68] and Kyuma *et al.* [59]. These devices are not able to measure the modest fields on circuit boards. We have found two groups which have built devices which do have promise for measuring circuit board fields, the Schlumberger group (see section 4.4.1) and the SRICO group (see section 4.4.2).

4.4.1 Electrooptical techniques used by Schlumberger

Articles by Tremblay and Meyrueix [108] and Tremblay *et al* [109] describe using the electrooptical crystal $Bi_4Ge_3O_{12}$ (BG0) for the specific application of measuring the electric field on circuit boards. They have been awarded United States patent number 5,272,434 (issued 21 December 1993) for their specific implementation of this method: "Method and apparatus for electrooptically testing circuits."

The authors describe a system in which a single beam is used to interrogate an array of points on the underside of the circuit board. Their system utilizes a beam traversed over the board with an acousto-optic deflector (see figure 17). Their system includes a special elastomeric-based connector whose purpose is to enhance the electric field in the electrooptical crystal.

The authors have been not been responsive to requests for information.

4.4.2 Electrooptical techniques used by SRICO

S. Sriram, at SRICO,[16] performed research on a Phase I SBIR project using the electrooptic effect and Mach–Zehnder interferometers. This work was performed for the Army's Harry Diamond Laboratories, under contract number DAAL02–90–C–0078. The final report is in Sriram [102] United States patent number

[16] SRICO, 664 Petworth Court, Powell, OH, 43065–9398

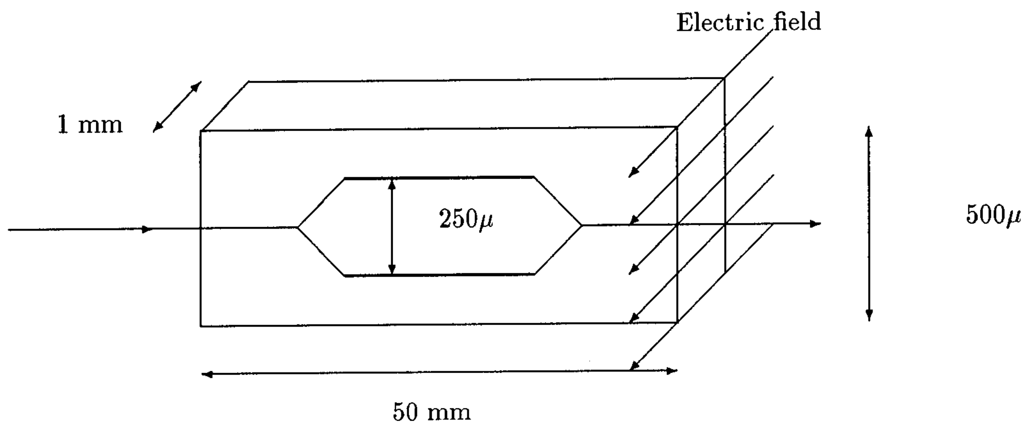

Figure 18: SRICO's electromagnetic field sensor (not to scale)

5,267,336 has been awarded for this work on 30 November 1993 (this patent has the title"Electro-optical sensors for detecting electric fields").

SRICO continued with this project and is now in the middle of a SBIR Phase II contract for the Army's Harry Diamond Laboratories (contract number DAALO2-92-C-0018) with the title *Optical Interferometers for Sensing Electromagnetic Fields.* A recent report of their progress may be found in Naghski *et al* [75].

SRICO has developed (see Sriram [102]) a unique method of creating an electrode-less Mach–Zehnder interferometer in lithium niobate by combining a titanium diffusion step followed by a proton exchange process. The titanium diffusion in selected sections of the crystal in a +Z oriented substrate reverse poles that section. Subsequently the Mach–Zehnder waveguide structure is created at a low temperature by using proton-exchange waveguide techniques. A graphical illustration of the active components in SRICO's sensor is shown in figure 18 along with typical dimensions. The device is made from an electrooptical material, is about 50 mm long by 500μ wide, and is fabricated on a plate 1 mm thick. The lines shown are about 5μ deep. The diamond-shaped area has upper and lower "legs" (shown darker). The upper leg is doped so that it is "oppositely poled" from the lower leg.

A light ray is injected from the left into the device. This ray is split and each ray travels down one side of the diamond-shaped area. The rays are combined to determine a phase difference. If there is no ambient electric field, then there is a zero phase difference between the two light rays. If there is an ambient electric field, then there will be a detectable phase difference since the optical properties in each leg will be different. Because of the orientation of the opposing electrooptical components, this device can detect electric fields that are in to (or out of) the page.

Note that the device has no metallic electrodes, hence there is no interference of the electromagnetic field being measured. Connection of fiber optic cables requires that a 5 mm long connector be attached where the light ray enters the device.

Naghski *et al* [75] describes the results of tests on fabricated SRICO devices. They indicate a measured minimum detectable field of 0.22 V/m$\sqrt{\text{Hz}}$. This is interpreted as follows: if the bandwidth of the measurement system (the bandwidth around some clock frequency) is 1 Hz, then the device can detect fields as small as 0.2 Volts per meter. If the measurement bandwidth around a center frequency were 100 Hz, then the device can detect fields as small as 2 Volts per meter. The product literature from SRICO indicates that maximum detectable electric field is 150 kV/m.

Further, Sriram of SRICO has estimated that

- the measurement time is on the order of 10–30 milliseconds.
- the repeatability of measurements using the same probe is about 5%
- two ostensively identical sensors may disagree by as much as 5%

4.5 Electrostrictive materials

Fiber-optic electric field sensors employing electrostriction ceramics have demonstrated high resolution detection of electric fields both at very low frequencies (less than 1 Hz) using a high frequency differ field (see Vohra *et al* [113] and Fabiny *et al.* [34]) and at frequencies in the range of 1–60 kHz using a DC bias field (see Vohra and Bucholtz [112]).

The measurement device described by Vohra and Fabiny [114] is a mechanical device and, because of inertia, it's motion is limited in frequency. The electrodynamic device is a lead magnesium niobate ceramic which has a nonlinear strain response to an applied electric field. The material is an insulator and electric fields up to microwave frequencies can penetrate the material. By using a mixing technique in which a local oscillator field is applied to the electrostriction material (analogous to that discussed in section 4.9.2) the device can be used to measure very high frequency electric fields.

Vohra and Fabiny [114] have made measurements up to 20 GHz, and their device had a resolution of 5 μVolts/$\sqrt{}$Hz. However, their total device was "large" (it used 35 meters of fiber-optic material wrapped on the electrostriction shell).

4.6 Liquid crystals

The discovery in 1968 of dynamic scattering in nematic liquid crystals made possible liquid crystal displays for devices such as watches and calculators. (Note, though, that some display devices use a different effect, the field-effect mode.) Background may be found in Blinov and Chigrinov[11] or Castellano [20].

Standard liquid crystals are constructed of a parallel plate capacitor with liquid crystalline material acting as the dielectric. The plates are two pieces of glass, each having a thin conductive coating. The thickness of the active area is generally in the range 6–25 μm. Application of a DC or low-frequency AC signal across the plates changes the material into a milky white liquid. The appearance is due to the creation of scattering centers within the liquid and not to a chemical reaction. Many studies of the light-scattering ability of liquid crystals when an electric field is applied, have been made (see, for example, Bertolotti *et al.* [10], Gerritsma and Van Zanten [42], or Schaetzing and Litster [97]).

Several electromagnetic field imaging devices have been constructed using liquid crystals, United States patents 3,627,408 and 3,790,251 contain specific applications of this (a good review is in Kaneko [52]). We have reproduced Kaneko's figure 2.15 as our figure 19. Note that the required applied voltage is on the order of Volts. Given the size of the liquid crystal, this requires an electric field on the order of kilo-Volts per cm. This is a much larger field than the one emitted from a circuit board.

From our contacts we believe that liquid crystals can be activated at much lower electric field levels, but we have not been able to find appropriate references. However, we do not believe that liquid crystals can be used at the frequencies of operation that we are interested in (MHz) for the application to circuit boards.

Note that other groups have investigated the imaging of liquid crystals (1) under the effect of magnetic fields (see, for example, Leslie [64]) and (2) under the effect of temperature (see for example, Ennulat and Fergason [33]).

4.7 Magnetic force microscopy

This technique developed at Sandia National Laboratory uses a scanning probe microscopy technique to detect and image the magnetic fields induced by internal currents in operating integrated circuits, with a high degree of spatial resolution and magnetic field sensitivity (see Hartmann [48] for the general theory and Campbell *et al.* [18] and [19] for imaging applications). Campbell *et al.* [19] indicates that fields as small as 1 μTesla can be measured in a horizontal resolution of 1 μm. Because of the fine horizontal resolution this technique does not, we believe, generalize to large areas such as printed circuit boards.

4.8 Magnetooptical field sensors

Many magnetic field sensors have been reported which use magnetically active materials and optical measurement techniques, including the magnetostrictive sensor, the Faraday effect sensor (see Bucholtz [15] and Lenz [63]), and the Kerr effect sensor (see Oliver *et al* [78]).

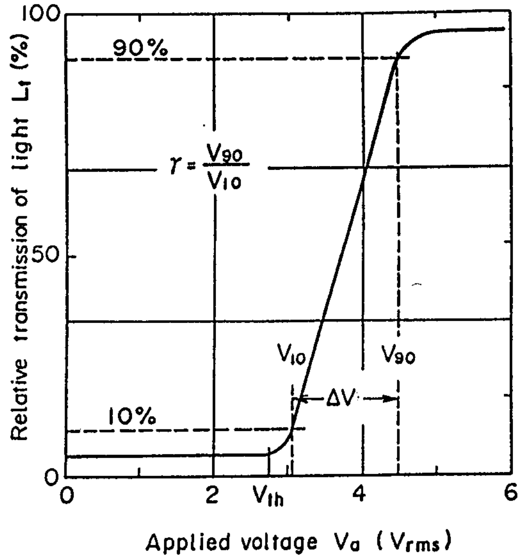

Figure 19: Electrooptic response of a TN-FE mode liquid crystal cell (from Kaneko [52]).

- Magnetostrictive sensors use magnetic materials that enlongate or contract upon magnetization to change the length of attached optical fibers. The magnetic field strength is then be determined by measuring the difference in optical path between the distended fiber and a reference fiber using interferometric techniques.
- Many Faraday effect sensors use magnetic materials which have large Verdet constants, where the magnetic field component along the direction of light propagation can be determined through polarimetric measurements of the non-reciprocal polarization rotation that occurs as light transits the magnetic material.
- The magnetooptic Kerr effect (MOKE), like the Faraday effect, causes non-reciprocal changes in the state of polarization of light. But in the MOKE, the effects occur when light reflects off a magnetized surface (see Freiser [36]).

The Faraday effect is a rotation of the polarization of an optical wave transmitted through a material along the magnetic field. It occurs as a result of the right circular component of the wave propagating with a slightly different phase velocity than the left circular component of the wave. The Kerr effect corresponds to the polarization rotation produced by surface reflection. An excellent description of the interrelationship of the Kerr and the Faraday effects is contained in the article by Suits [105]. The Kerr effect and the Faraday effect are linearly related by the off-diagonal element of the permittivity tensor. The dielectric tensor can be written in the following manner when the magnetic field is aligned with the z-axis (from Suits [105, equation 3]):

$$\epsilon = \begin{pmatrix} \epsilon_{xx} & \epsilon xy & 0 \\ -\epsilon_{xy} & \epsilon xx & 0 \\ 0 & 0 & \epsilon zz \end{pmatrix}$$

In this notation (and introducing θ and ψ as the real and imaginary parts of the angle through which the polarization is rotated)

- for the complex Faraday rotation (when transitted a length l, and λ_0 is the free-space wavelength):

$$\theta_F - i\psi_F = \frac{\pi l}{\lambda_0} \frac{\epsilon_{xy}}{\sqrt{\epsilon_{xx}}}$$

- for the polar Kerr polarization rotation (see below):

$$\theta_K - i\psi_K = \frac{i\epsilon_{xy}}{\sqrt{\epsilon_{xx}}(\epsilon_{xx}-1)}$$

Both the Faraday and Kerr rotation angles are proportional to ϵ_{xy}. The Faraday effect increases linearly with distance traveled and has the potential to be much larger than the Kerr effect. It is proportional to $k_0 l$, while the Kerr angle has a relative permittivity in the denominator, which will reduce the rotation compared to that of the Faraday rotation. Faraday rotations of 8,000 degrees (see Samarth and Furdyna [94]) have been measured in transmission measurements with a diluted magnetic semiconductor composed of crystalline $Cd_{1-x}Mn_xTe$.

Other recent work on this topic has included:

- A paper in Russian by Vetoshko *et al* [111] claims to have used ferrite–garnet films to measure 10^{-6} Oe, in 10 nanoseconds, with a resolution of 3μm. We have not seen an English translation of this paper.
- Gerald L. Fitzpatrick of Physical Research[17] received a 1993 Phase II SBIR contract (number N60921-93-C-0066 on topic 90-176) for work with the title *Advanced Magneto-Optic/Eddy Current Techniques for Detection of Hidden Corrosion Under Aircraft Skin.* The abstract of their Phase II proposal was:

  > "Magneto-optic/eddy current technology has been recently developed for rapid inspection of surface breaking cracks initiating near rivets in aluminum aircraft alloys. Experimental evidence indicates that this technology can be extended to include rapid detection and imaging of subsurface cracks and corrosion. With this new technology planar eddy current induction methods excite electromagnetic fields in the workpiece, which are detected with a magneto-optic sensor, producing direct, real-time imaging of defects. The magneto-optic sensor responds to static or time varying magnetic fields normal to the inspection surface. These fields are produced when cracks or other defects, including corrosion, interact with the induced electric currents. The magneto-optic sensor responds to frequencies from 0 (DC) to well over 500 kHz. The lower frequencies, 0 to about 10 kHz, should be useful for imaging and detection of subsurface cracks and corrosion, while the higher frequencies are useful for inspection of surface cracks. Direct observation of the magneto-optic sensor using polarized light and an analyzer reveals real-time images of defects. This new technology offers the advantages of rapid coverage of large areas, higher sensitivity to small cracks, more direct detection and classification of defects, and simple, inexpensive recording of the entire inspection."

  We do not know the size or resolution of this proposed sensor.

4.8.1 Geometry of the Kerr effect

Kerr effects occur when a light beam is reflected from a magnetooptical material. There are three separate manifestations of the Kerr effect (polar, longitudinal, and equatorial), corresponding to the orientation of the incident light beam relative to the orientation of the magnetic field. Figure 20 contains graphical illustrations of these three cases. For sensing of an electromagnetic field above a circuit board, all three effects will be present.

The three types of Kerr effects can be explained by the reflectivity relation between the incident light and the reflected light:

$$\begin{pmatrix} E_{\text{reflected}\perp} \\ E_{\text{reflected}||} \end{pmatrix} = \begin{pmatrix} r_{11} & r_{12} \\ r_{21} & r_{22} \end{pmatrix} = \begin{pmatrix} E_{\text{incident}\perp} \\ E_{\text{incident}||} \end{pmatrix}$$

where r_{ij} are the coefficients of the reflectance matrix, and the perpendicular (TE) and parallel (TM) electric field components are represented by the subscripts $\perp$ and $||$. Note that the r_{ij} are dependent on the angle of incidence between the incident light and the magnetooptical sheet.

[17] Physical Research, Inc., 25500 Hawthorne Blvd, Ste 230, Torrance, CA 90505

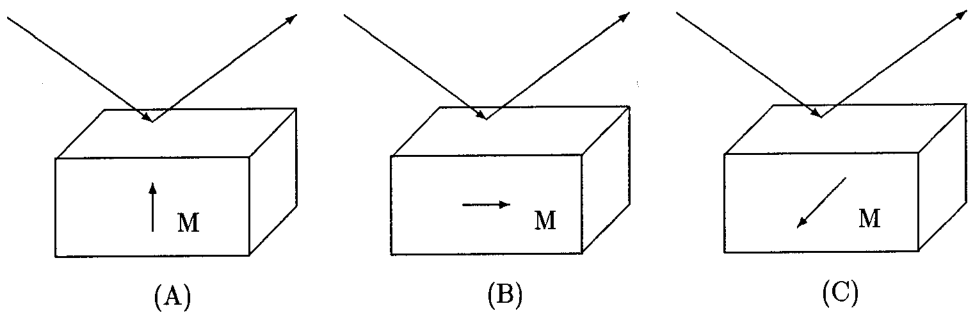

Figure 20: The three aspects of the Kerr effect: (A) polar, (B) longitudinal, (C) equatorial

The diagonal elements r_{11} and r_{22} can be calculated by Fresnel reflection coefficients and Snell's law. The off-diagonal elements (r_{21} and r_{12}) can be derived from the magnetooptical permittivity tensor, the applied magnetization, and Maxwell equations with the appropriate boundary conditions. See, for example, Arecchi and Schulz-DuBois [5]. We now describe how the r_{ij} differ in the three cases of the Kerr effect:

- polar Kerr effect

  This effect takes place when the magnetization is perpendicular to the plane of the magnetooptical sheet. The reflection coefficients satisfy $r_{12} = r_{21}$.

- longitudinal Kerr effect

  This effect takes place when the magnetization is in the plane of the magnetooptical sheet, and parallel to the plane of incidence. The reflection coefficients satisfy $r_{12} = -r_{21}$.

- equatorial Kerr effect

  This effect takes place when the magnetization is in the plane of the magnetooptical sheet, and perpendicular to the plane of incidence. The reflection coefficients satisfy $r_{12} = r_{21} = 0$.

The Kerr effect has long been used for the characterization of magnetic materials. It has been used to measure the magnetic field distribution around a magnetic recording head (see Re and Kryder [89]). It is now being used as a stand-alone magnetic field sensor. In particular, Oliver *et al* [78] has measured fields as small as 2 mOe/$\sqrt{}$Hz at a frequency of 8 MHz. They also indicate that their technique should measure fields as low as 10^{-6} Oe/$\sqrt{}$Hz. DiMarzo,[18] one of the authors of [78], has told us they can measure 10^{-4} gauss.

When MOKE is being used, magnetic sensing materials are required. Oliver used 0.5 cm diameter disks of amorphous $Fe_{20}B_{20}$, deposited onto fused quartz substrates using standard ion beam sputtering techniques.

Measurements utilizing the Kerr effect have been used to image the domain structure of ferromagnetic materials in the presence of high fields (see Cullity [24]). It appears to us that this effect has not been used to observe effects associated with small fields until recently. Oliver *et al.* [77] has recently utilized the Kerr effect to measure small fields, with the fields varying at eight milli-Hz.

The measured sensitivity in the experiment was 0.4 μTesla. Oliver projects that with improvements to his apparatus to increase the sensitivity, it might be possible to measure fields whose spectral density is as small 10^{-10} Tesla/$\sqrt{}$Hz.

We understand that increasing the frequency range of operation would present difficulties.

4.8.2 Limitations due to environmental isolation

The techniques discussed in this report generally require that the sensing materials be environmentally isolated. That is, there cannot be large vibrations, magnetic fields, electric fields, temperature changes near the measuring equipment. The earth has a magnetic field that varies from 0.1–1.0 Gauss (see Lenz [63]). Note that this is approximately two orders of magnitude larger than the field that we are trying to measure (see table 7). However, since the Earth's field is a DC field it will not interfere with our measurements.

[18] Personal communication

4.9 Magnetostriction techniques

Magnetostriction is a phenomenon in which a magnetically active material strains in response to approximately the second power of the applied magnetic induction field, B, i.e.

$$e = CB^2, \tag{6}$$

where e is the strain of the magnetostrictive material. The constant parameter C is dependent on the materials and the design of the sensor. For some recent designs with modern transducer materials such as iron–boron metallic glass alloys, the value of C is about 100/Tesla^2 according to Bucholtz [15].[19]

The small–signal strain can be made to be a linear function of a small magnetic field by applying a large bias field. The "cross–product" term in the square of the total magnetic field is linear in the small magnetic field.

Fiber optic waveguides can be used in one of two ways to measure the strain of the magnetostrictive material.

1. Magnetostrictive coatings can be painted onto a fiber waveguide exposed to a magnetic field and the strain of the fiber caused by the magnetically–induced stress in the jacket can be measured optically.

2. The fiber can be bonded to a magnetostrictive object exposed to a field. The object might be a strip or cylindrical shell of metallic glass or other magnetostrictive material. This way of measuring magnetic fields can have high sensitivity, but because it relies on axial strain (and therefore motion of the fiber and magnetostrictive material) inertial effects limit the frequency at which such a device can faithfully follow the applied field.

4.9.1 Sensitive low–frequency device

A very sensitive device has been made by Bucholtz *et al.* [16] with fiber wound azymuthally on a metallic glass cylindrical shell. The shell was 5.1 cm long, 4.45 cm diameter and had a wall thickness of 25 micrometers. The length of fiber bonded to the shell was 34 meters. Such an arrangement is appropriate for measuring magnetic fields of frequency lower than the mechanical resonance frequency of the shell. This design has been demonstrated at frequencies up to 34 kHz and it was shown to have very high sensitivity (see Bucholtz *et al* [16]). This device operating with a laser interferometer had a noise floor of 70×10^{-15} Tesla/$\sqrt{\text{Hz}}$ at 34 kHz.

4.9.2 Achieving high frequency performance through mixing

Bucholtz *et al* [17] demonstrated an arrangement in which through applying both a DC magnetic field and a high frequency dither field, a large device which resonates mechanically at about 25 kilo Hertz is operated so as to measure RF magnetic fields with a sensitivity which is uniform from 0.1 Hertz to about 1.0 MHz.

We will report on this concept in some detail. The sensitivity given by equation 6 is modified to include the presence of three fields, a static bias field, a dither field and the field to be measured. This equation then becomes

$$e = C(B_0 + B_d \cos\omega_d t + B_s \cos\omega_s t)^2$$

The high frequency detection uses the difference frequency term in the expansion of the square of the field. In the expansion of the time–varying field there is a term of the form,

$$e(t) = CB_d B_s \cos(\omega_s - \omega_d)t,$$

which describes the strain at the difference frequency. In the experiment described in Bucholtz *et al.* [17] there is a natural resonance of the magnetostrictive cylinder at about 30 kHz. This resonance is used as an IF strip in a heterodyne receiver in which the local oscillator is the dither field, B_d. The resonance of the receiver and the response of the system are shown in figures 1 and 3 of Bucholtz *et al.* [17]. Their figure 3 has been reproduced as our figure 21. Note that the IF receiver used in the experiment is basically a fairly

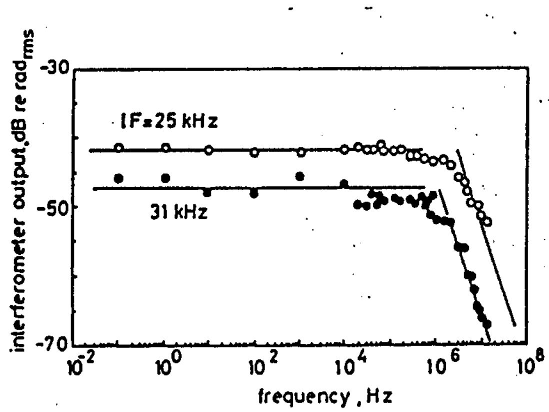

Figure 21: Amplitude of strain at difference frequency (IF) as a function of test signal frequency for IF= 25 and 31 kHz (from Bucholtz *et al.* [17])

large low-frequency device operating at it's resonance. The resolution using mixing was 26 pT/$\sqrt{\text{Hz}}$; it was limited by the 4 μradian/$\sqrt{\text{Hz}}$ interferometry noise level at the intermediate frequency.

The operative question, to determine whether a similar system would be useful with circuit boards, is whether the principles employed can be scaled to the physical dimensions of circuit boards without the noise of the system becoming excessive. There are two significant noise sources, thermal noise in the magnetostrictive device and phase noise in the laser system.

- The interferometer phase noise is on the order of 1.5μradian/$\sqrt{\text{Hz}}$ and is approximately independent of frequency.
- The thermal noise–limited performance of the magnetostrictive device has been estimated using the fluctuation dissipation model described by Mermelstein [70]

$$\frac{B_{min}}{\sqrt{Hz}} = \frac{1}{CB_0}\sqrt{\frac{k_B T}{V E_m \omega Q}}. \tag{7}$$

4.10 Piezomagnetometer technique

Walter Podney of SQM Technology, Inc.[20] received a Phase II SBIR contract (number DAAH01-93-C-R341 on topic 91-004) for work with the title *Development of Piezomagnetometer Arrays.* The abstract of their Phase II proposal was:

> "Phase I demonstrates feasibility of a PiezoMagnetometer, a small, rugged low cost magnetometer that promises a resolution of 1 pT/$\sqrt{\text{Hz}}$ at a power of 1 mW. It is a composite of magnetostrictive and piezoelectric materials. A change in magnetic field strains the magnetostrictive layer, which in turn stresses the piezoelectric layer. Stress polarizes the piezoelectric material, separating electric charge in proportion to the magnetic field variation. The composite converts variations in magnetic field to variations in electric charge. Their small size, low power, and low cost make arrays of PiezoMagnetometers practical. Phase II development divides into three parts: (1) a Base Plan, (2) Option I, and (3) Option II. The Base Plan develops a magneto-electric sensor, with a volume of 1 cc, that can resolve a magnetic induction of 1 pT/$\sqrt{\text{Hz}}$, below 100 Hz, uses it to form vector, scalar, and differential magnetometers, and sets designs for linear and planar arrays of PiezoMagnetometers. Success of the Base Plan leads to development of linear and planar arrays in Options I and II."

[19] Note that Bucholtz [15] designates the magnetic field as H, but uses SI units for B rather than H

[20] SQM Technology, Inc., P.O. Box 2225, La Jolla, CA 92038.

A piezomagnetometer uses a magneto-electric composite, formed by alternating layers of piezoelectric and magnetostrictive material, to convert a fluctuating magnetic field directly to electric current. Strain in the magnetostrictive layers, coming from an ambient magnetic field, stresses piezoelectric layers and drives a polarization current proportional to amplitude of the ambient field. Electrically, the composite is a current source connected in parallel with a capacitor. Its simple and direct operation and solid state sensor enables constructing a small, rugged, inexpensive magnetometer that operates at ambient temperature with high sensitivity at low power.

Communication with Podney[21] has revealed the following results. Measurements using a 25μm layer of a metallic glass (Metglas 2605 SC) bonded to a 125μm thick wafer of lead zirconate-titinate ceramic piezoelectric show a resolution of about 0.6 nT/$\sqrt{\text{Hz}}$, above a few Hertz. A composite stack of 200 layers, about 1 cm tall and 1 cm in diameter, can give a resolution of 1 pT/$\sqrt{\text{Hz}}$, at frequencies above a few Hertz.

The large size of the Podney sensor would, initially, disqualify it as a likely method to be used with circuit board imaging.

4.11 Superconductive techniques

The most familiar type of superconducting electromagnetic field measurement device is the superconductive quantum interference device (SQUID), but there are other superconducting techniques (see Gousev *et al.* [45]). A SQUID can act as an extremely sensitive magnetic field sensor. From Giallorenzi *et al* [43]:

> "The most sensitive devices for measurements of small magnetic fields at present are SQUIDs, which are capable of detecting fields as small as 10^{-11}–10^{-12} gauss in the laboratory, but often less sensitive in the field.

This is orders of magnitudes more precision than is required for our application.

A two dimensional array of SQUIDs could be used to visualize the magnetic field over a region.

Walter Podney of SQM Technology, Inc.[22] received a Phase II SBIR contract (number FQ8671-9301339 on topic 93-022) for work with the title *High Temperature SQUID Microprobe for Eddy Current Evaluation of Airframes.* Part of their Phase I abstract was:

> "Superconductive Quantum Interference Devices (SQUIDs) bring new physics, new technology, and new capability to eddy current nondestructive evaluation (NDE) of materials. A SQUID offers new technology for measurement of magnetic flux at low frequencies with unprecedented sensitivity. Its extreme sensitivity at low frequencies can provide an electromagnetic microscope for eddy current NDE of underlying defects and hidden corrosion in airframes. Our measurements with a prototype SQUID microprobe, using niobium technology at 4 K, show that it reliably finds a 1 mm flaw through 6 mm of aluminum, at 88 Hz and a standoff of 4 mm, as well as material loss less than 1% from corrosion under a 2.29 mm thick aluminum plate. The new capability offered by a SQUID microprobe together with advances in fabricating SQUIDs and pickup coils from high-temperature superconductors provides a technological opportunity for developing a hand-held, electromagnetic microscope for evaluating hidden defects in airframes during flight-line operations. Its development requires the combined skills of experts knowledgeable in (1) eddy current NDE of materials, (2) NDE of military and commercial airframes, (3) fabrication of SQUIDs from high-temperature superconductors, and (4) use of SQUIDs for eddy current NDE. To realize the promise of a new capability for inspecting the aging fleets of both military and commercial aircraft, we propose to lead a development team comprising IBM, Northrop Corporation, Boeing, and SQM Technology, Inc."

4.12 Thermal Techniques

Many researchers have attempted to use thermal techniques (detection of infrared radiation) to directly measure electromagnetic fields. See, for example Norgard *et al.* [76], Sega [98], Sega and Genello [99], and Sega *et al.* [100].

[21] Personal communication

[22] SQM Technology, Inc., P.O. Box 2225, La Jolla, CA 92038.

The infrared thermal imaging technique s based on Poynting's theorem for the absorption of electromagnetic energy in a lossy, complex material, when an electromagnetic wave passes through that material. The lossy material forms a detection screen for the absorbed electromagnetic energy. The absorbed electromagnetic energy in the detection screen is re-radiated as "black body" type energy, which can be detected with a thermal infrared imaging system.

In Sega *et al.* [100] the authors determined the field scattered from an aluminum cylinder when illuminated by a 2–4 GHz microwave field. The material that responded to the field was a sheet of carbon paper placed 1/8 inch behind the cylinder. The infrared system gave a 30 dB dynamic range (peak measurements of 20°K, with an accuracy of 0.02°K).

5 Sensitivity Requirements of Ancillary Measurement Devices

Depending on the technology used, there are several different types of equipment and ancillary measuring devices that may be required for the visualization of electromagnetic fields. These devices and concerns include:

- infrared detectors (see section 5.1)
- phase angle detectors (see section 5.2)
- surface height measurement systems
  - non-contact systems (see section 5.3.1)
  - contact systems (see section 5.3.2)
- motion of the sensing point (see section 5.4)
- sampling time (see section 5.5)

5.1 Infrared detectors

Infrared detectors detect heat. Heat may build in resistor components of a circuit board, as well as on an external sensing sheet. There are periodic reviews in the literature, comparing and contrasting different commercially available infrared detectors. For example Kaplan [53] lists 12 commercial manufacturers of infrared imaging systems. From Kaplan [53] we also find:

- general information about thermal viewers

  > "Thermal viewers are inexpensive ($10,000 to $14,000) battery powered scanning instruments producing a qualitative image of the thermal distribution over the surface of the target. ...
  > Thermal viewers were not designed for absolute temperature measurements, but they can demonstrably sense temperature differences of tenths of degrees. ... Thermal viewers operate most effectively with cooler targets (0–200°F) but, though the use of optical attenuators, they can be used for targets up to 2000°F. Typically the area scanned (field of view) of thermal imagers is from 6 to 8 degrees high and from 12 to 18 degrees wide, with a spatial resolution (instantaneous spot size) of 2 milliradians (0.1" at 5 feet)."

- general information about pyrovidicon imagers

  > "Pyrovidicon imaging systems ar not unlike home videorecording systems except that the camera tube is a pyroelectric vidicon (pyrovidicon) rather than a conventional vidicon, and records target radiation in the infrared rather than the visible spectrum. ...
  > Thermal resolution of these instruments is between 0.2 and 0.4°F. in panned made and double that (half as good) in "chopped" mode."

- general information about thermographic raster scanners (imaging radiometers)

  > "Thermographic raster scanners (also called imaging radiometers) constitute the "top-of-the-line" of commercial thermographic instruments. ... Thermographic scanners use refractive, reflective or hybrid scanning systems and operate in either the 3–5μ or the 8–14μ atmospheric window. In addition to quantitative temperature measuring capability, these instruments feature excellent spatial resolution (about 1 milliradian) and minimum resolvable temperature (0.05 to 0.1°C)."

Kaplan also provides information about current applications of imaging systems:

> "Clearly the most dramatic recent development in the use of thermographic raster scanners has been the introduction of computer-assisted thermal image storage and processing, causing thermographic scanning to become a far more exact science and greatly expanding its usefulness. ... Perhaps the single most powerful feature of these new routines is the capability for archiving

Field of view	20° (vertical) by 27° (horizontal)
Minimum discernible temperature	0.1°C at 30°C
Display resolution	480 lines × 512 pixels
Image update rate	30 frames per second

Table 8: Parameters for FLIR's IQ Series Model 325 infrared detector

Field of view	30.5° by 22.5°
Thermal sensitivity	0.2°C for 22–55°C
Display resolution	245 × 193 pixels
Image update rate	15 seconds per image

Table 9: Parameters for Compix's PC2000 infrared detector

thermal images of acceptable components, assemblies and mechanisms, and using these stored images as models for comparison to subsequently produced items. Subtractive routines produce differential images illustrating the deviation of each pixel (picture element) from its corresponding model. ... There is great interest in applying this spatial emittance correction to larger targets such as printed circuit boards, where several military programs are concerned with infrared mass screening of printed circuit boards for gross faults at the depot level. The approach used is to archive a standard thermal profile of a known acceptable board, and use this as a model against which to compare the profile of a powered unit under test."

Research on improved infrared detectors continues. Olsen [79] reports the results of a recent Army SBIR Phase I research effort.

Applications of infrared imaging to circuit boards includes:

- Funk *et al* [38] presents a semi-numerical technique for predicting the temperatures on circuit boards.
- Godfrey *et al.* [44] has used ANSYS to predict package temperatures.
- There are several simulation packages that perform a thermal analysis from a CAD design of a circuit board. One of these is AutoTherm.[23]
- Pearson [83] describes a product, AITIS, that identifies and locates thermally related faults on printed circuit boards by comparing the image of a known good printed circuit board, stored in memory, with the live image of a suspect unknown board.

Two commercial infrared detectors are:

- The FLIR[24] Q Series Model 325 is sensitive to 2.0–5.6 micron wavelengths. FLIR's literature claims that this device is the highest resolution thermoelectrically cooled system presently on the market. This device has the parameters as shown in table 8.

  The IQ Series Model 812 is sensitive to 8–12 micron wavelengths. This range is useful for objects near ambient temperatures.
- The Compix[25] PC2000 has the parameters as shown in table 9.

[23] AutoTherm is produced by Mentor Graphics, 8005 SW Boeckman Road, Wilsonville, OR 970700-7777.
[24] FLIR Systems, 16505 SW 72nd Avenue, Portland, OR 97224.
[25] Compix Incorporated, PO Box 885, Tualatin, OR 97062.

5.2 Measurement of phase angle

For the electrooptical and the magnetooptical technologies, a shift of phase angle between two arms must be measured. This relative phase shift can be measured with laser interferometry equipment. A sensitive device for measuring small phase angles is a Mach–Zehnder interferometer (see Born and Wolf [12]). There are five classes of detection systems for use with a Mach–Zehnder interferometer: passive homodyne (HOM), homodyne with DC phase tracking (PTDC), homodyne with AC tracking (PTAC), true heterodyne (HET), and synthetic heterodyne (SHET).

5.2.1 Phase detectors

This section describes the ability to measure small amounts of phase.

A great deal of work was performed at NRL in the late 70's and early 80's on developing ultra-sensitive fiber-optic Mach–Zehnder interferometers whose purpose was to detect small optical phase changes due to acoustic strains in optical fiber waveguides. The paper by Giallorenzi *et. al* [43] reviews the then-current performance of fiber optic sensors (acoustic, magnetic, gyro, and laser diode) which detect through a measurement of phase angle. They report that optical interferometers appeared to be capable of detecting an optical phase shift whose spectral density is as low as 10^{-6} radians/$\sqrt{\text{Hz}}$, limited by shot noise in the photo-detector.

The recent review article by Dandridge and Cogbell [26] describes applications of fiber-optic technology to very sensitive acoustic, magnetic, and gyroscopic measurements for use at sea. The conclusions are that active homodyne optical interferometers are capable of detecting a noise spectral density of about 0.6μradians of optical phase shift per square root of Hz at 1000 Hz and this floor of detectability varies monotonically with frequency to the -0.6 power. The data reported are over only the acoustic range of frequencies, i.e., up to about 6000 Hz. Giallorenzi *et al.* [43] assert that the lower limit of detectability continues to decrease until it reaches a lower limit determined by shot noise in the photo-detector. They state that this limit is about one-hundredth of a micro radian. The increased sensitivity is achieved through the use of a alternative configuration of the passive homodyne modulation arrangement, invented by Dandridge *et. al* [27] in 1982. This system has very high sensitivity and high dynamic range. The observed dynamic range for this type of interferometer is approximately 140 dB.

Four alternative interferometer configurations are discussed in Dandridge *et al.* [27]. These are

1. passive homodyne,
2. active homodyne with phase tracking,
3. true heterodyne, and
4. synthetic heterodyne.

In Mach–Zehnder systems that have been tested the active homodyne interferometer system has exhibited the greatest sensitivity. In this system, a length compensator is used in the reference arm of the interferometer to maintain the length difference between the signal and reference arms at a quarter of an optical wavelength plus perhaps an integral number of optical wavelengths. Length changes due to thermal drift and other environmental changes typically require constant adjustment of the compensation system. Sensitivity is best when the integral number of additional wavelengths is zero.

The length compensator used is typically a piezoelectric rod whose length is changed electrically. Fiber in the reference arm is wrapped on the rod so that its length will change as the rod expands or contracts. The circuitry to maintain the compensator at the proper length is somewhat complicated.

Dandridge [27] describes an alternate to the active homodyne configuration which he calls a "passive homodyne". This configuration has high dynamic range and sensitivity almost as high as the active homodyne. The dynamic range for a laboratory prototype of this "passive homodyne" interferometer was approximately 140 dB. In this design there is additional circuitry required to generate two phase-modulated quadrature components of the carrier.

A comparison of the noise floors of the active and passive homodyne detectors is shown in figure 22 as a function of the length difference between the sensor and reference arms. The lowest curve represents the minimum detectable phase shift for the active homodyne system. The three curves above it are for the

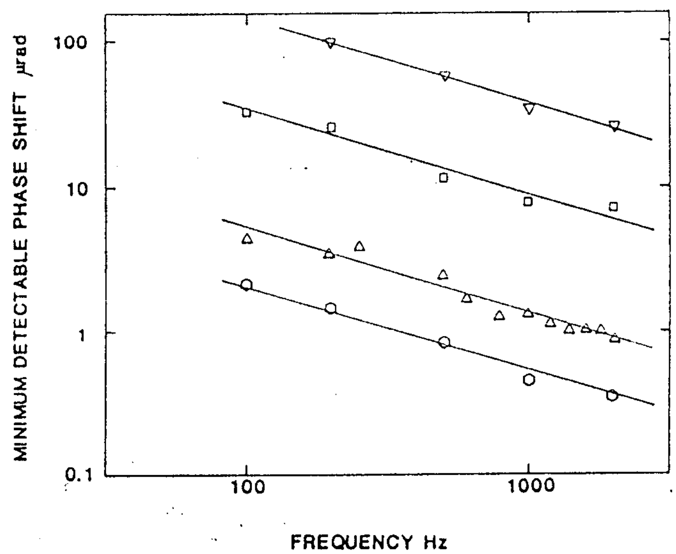

Figure 22: Minimal detectable phase shift as a function of frequency (from [27])

passive homodyne system with a path length difference between the signal and reference arms of zero, two and ten centimeters respectively. The floor for detectability increases monotonically with this difference.

The passive homodyne developed by Dangdridge requires that the optical carrier be phase modulated at a frequency higher than that of the measurement band. The measurements appear as sidebands of the modulated carrier. For use in circuit board measurements up to 100 MHz the carrier would have to be modulated at a frequency of at least 200 MHz. This would present difficulties.

5.3 Measurement of surface height

For the piezoelectric and electrodynamic technologies, a surface height must be determined. There are many commercial products that can be used to determine the height of a sensing sheet. These products fall into two categories, non-contact and contact methods.

5.3.1 Measurement of surface height: non-contact method

This type of measurement can be obtained with laser interferometry equipment. The recent article by Kaplan [54] describes a new system that can measure to an accuracy of 0.0005-in. There are many vendors of such equipment, including: Phase Shift Technology[26], WYKO[27], and Zygo.[28]

Note that this is an active area of research. A 1992 SBIR Phase I contract was awarded by DARPA to Juan Elizondo of Tetra Corporation[29] (contract number DAAH0193CR055 on topic 92-225) for work with the title *Holographic Interferometry for the Analysis of the Electro-acoustic Effect.* Their report describes the use of holographic interferometry to study both the mechanical and electrical stress characteristics of thin polymer films, especially those exhibiting electroacoustical behavior such as polyureas and polyurethanes. They attempted to correlate the holographic fringe pattern, created by the mechanical stress induced by the applied electric field, to the charge distribution induced in the polymer by the electric field.

[26] Phase Shift Technology, Inc, 3480 East Britannia Drive, Tucson, AZ 85706, 602/573–9250
[27] WYKO, 2650 East Elvira, Tucson, Arizona, 85706, 602/741–1044
[28] Zygo Corporation, Laurel Brook Road, PO Box 448, Middlefield CT 06455-0448, 203/347–8506.
[29] Tetra Corporation, 3701 Hawkins Street NE, Albuquerque, NM 87109, 505/345–8623

data acquisition time	0.110 sec
field of view	10 cm
measurement repeatability	$\lambda/300 = 2$ nm
number of pixels	320×240 or 640×480
overall accuracy	$\lambda/100 = 6$ nm

Table 10: Parameters for Zygo's GPI surface measurement device

WYKO

This company produces many products of potential interest, including

- RST Plus
  - field of view up to 8.2 mm $\times$ 6.1 mm
  - spatial sampling interval from 0.1 μm to 12.7 μm
  - measure surface heights from 0.1 nm to 500 μm
  - scan speed 2.4 μm/sec
- WYKO 400: 100 mm (4 in) test aperture
- WYKO 6000: 152 mm (6 in) test aperture

The WYKO 400 and WYKO 6000 can be used with either of two different lasers, with a wavelength of either $\lambda = 633$ nm or $\lambda = 1060$ nm. Whichever is chosen, the product literature claims that the unit is accurate to 1/100 wave (that is $\lambda/100 \approx 6$ nm). However, in detailed discussions we have determined that this value (1/100 wave) is only theoretically possible. (Since the reference flat in the machine used for comparison flat to 1/100 of a wave.) It was estimated that, in a relatively quiet room such as at a conference, 1/20 wave (about 30 nm) could be measured accurately. These WYKO products takes 5 frames of data and use them together to create a single estimate of surface height. It takes about 0.3 seconds to take all 5 measurements.

Note also that the WYKO 400 and the WYKO 6000 can detect a step height change, pixel-to-pixel, of not more than $\lambda/4$, where λ is the laser wavelength. Hence, a surface displacement of no more than 158 nm, or 251 nm, can be measured, pixel-to-pixel.

The pixel size is determined by the CCD camera used to record the fringe patterns. Typically, the CCD camera with measure 512 pixels by 480 pixels. Hence, for a 4-by-4 inch image of the sheet, each pixel corresponds to about 100 mm/480 $\approx 2 \times 10^{-3}$ m. For a 6-by-6 inch image of the sheet, each pixel corresponds to about 152 mm/480 $\approx 3 \times 10^{-3}$ m.

Zygo

The instrument GPI is manufactured by Zygo. With the 150 mm aperture, the (standard) laser wavelength of $\lambda = 633$ nm, and a (standard) internal reference surface flat to $\lambda/20$, the device has the parameters as shown in table 10.

5.3.2 Measurement of surface height: contact method

The instrument Dektak^3 [30] is representative of the contact measurement techniques. This device has a stylus that is dragged across a surface. The force of the stylus can be as low as 4 milligrams. As the stylus can be 12.5 microns in diameter, this would exert negligible pressure on the sensing sheet. The scan speed, in a straight line can be as much as, approximately, an inch a second. The noise floor of the measurements is about 3Å for slow scan speeds, this decreases for faster scan speeds.

[30] Dektak^3 is manufactured by Sloan Technology, A subsidiary of Veeco Instruments Inc, 602 East Montecito Street, Santa Barbara, CA 93103, 805/963–4431.

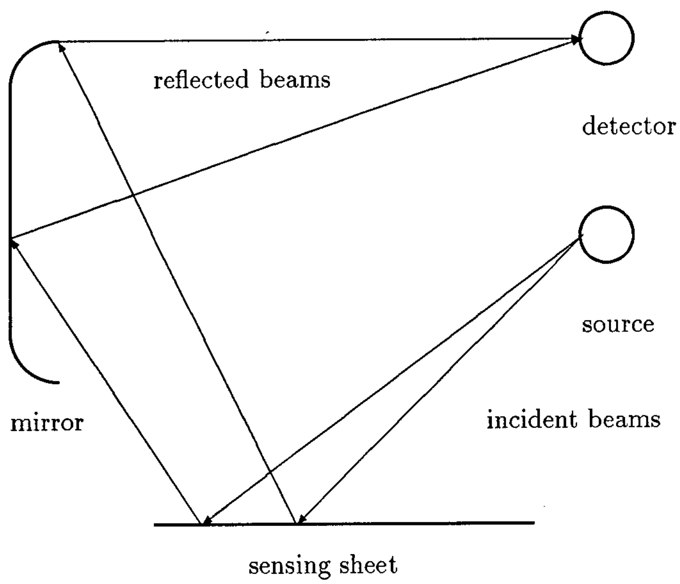

Figure 23: How to use a mirror with electronic steering and a single detector

5.4 Motion of Sensing Point

There are two basic ways in which the data corresponding to the electromagnetic field around a circuit board may be detected: point-by-point, or all points at once. For the sensor systems that measure the field at a single point, the sensing point must be moved to cover the field of interest. Generally there are two ways to move the point being sensed, either electronically, or mechanically.

- The circuit card can be moved horizontally in two directions (this motion will allow all regions of the card to be visualized)

  In this case, the speed and stability of mechanical positioning equipment may limit the operation of the sensor (see section 5.4.2).

- There is an array of sensors that cover the entire field of interest (so that the circuit card does not need to be moved).

- The light ray that is used for the detection can be electronically steered. (see section 5.4.1).

5.4.1 Electrical positioning

The difficult part of using electrical positioning of the signal is to sense the reflected beam, which may be leaving the circuit board at different angles. One solution of this problem is shown in figure 23, here all the reflected beams are focused onto a single detector by use of a mirror.

5.4.2 Mechanical positioning

A comprehensive list of commercial mechanical positioning device vendors may be found in pages 120–122 of *Laser Focus World* from February 1994. There are many manufacturers of such devices, including NEAT.[31] NEAT manufacturers many devices for precise positioning, including: motor driven single axis tables, motor driver rotary tables, and motor driven X–Y tables.

The X–Y tables have an additional parameter that impacts accuracy: orthogonality, or the degree of squareness between the two axes. This parameter is held to 20 (10) arc-seconds on NEAT's precision (special order) models. This corresponds to a 30 micron deflection when traversing 12 inches.

[31] NEAT stands for New England Affiliated Technologies, 620 Essex Street, Lawrence, MA 01841

NEAT also supplies stepper motors that can have a resolution of as little as .35μm (about 0.000014 inches).

NEAT's product literature has a good detailed discussion of thermal affects. We quote

> "To illustrate the degree to which thermal issues complicate the system, consider a 10" travel single axis table which seeks to achieve "tenth micron accuracy". Since a tenth of a micron is 4 micro-inches, we are looking for accuracy at the 4 ppm level. ... There will be ≈11" of base material (we will presume granite) between the table center and the stationary beamsplitter. ... If we choose to allocate our "error budget" of .4 ppm, assigning .1 ppm to atmospheric temperature, .1 ppm to atmospheric pressure, .2 ppm to granite thermal expansion. then we have the following result: air temperature must be be measured with .1 degree C absolute accuracy; pressure must be maintained to within .25 mm Hg accuracy; and the granite must be maintained at a constant temperature with .03 degrees C."

5.5 Sampling Time

The Nyquist criterion (see, for example, Oppenheim and Schafer [80, page 29]) states that the time T required to measure a signal of bandwidth W must satisfy $T > 2\pi/W$.

For example, if we are measuring, at a single location on the circuit board, frequency bins of width 10^4 Hz, then the sampling time for each bin must be at least $T > 10^{-4}$ seconds. If we are trying to measure frequencies from 0 to 100 MHz, then we require $N = 10^{8-4} = 10^4$ bin values. If each bin is measured with the theoretical minimum sampling time, then the total sample time required is $NT = 1$ second. Allowing an additional factor of 10 above the theoretical minimum indicates that, at a single location, all frequency bins could be measured within 10 seconds.

Crystal	n^3r/ϵ	Avail. dimensions (cm^2)	Origin	Remarks
MNA	50	1	France	Dangerous
ZnTe	10.8	1	USA	Low Resistance
AsGa	3	100	France	Low Resistance
CuCl	1.9	1	France	soluble
$LiNbO_3$	1.6	10	USA	non-cubic piezoelectric
$Bi_{12}SiO_{20}$	1.2	12	Japan	
$Bi_4Ge_3O_{12}$	0.5	100	France	
$KNbO_3$	0.5	2	France	Non-cubic; high ϵ

Table 11: Parameters for some electrooptical materials (from Tremblay *et al* [109])

6 Availability of Materials

For most of the techniques discussed in the proposal, special materials are required. In this section we discuss the availability of these different materials. For:

- electrooptical materials, see section 6.1
- magnetooptical materials, see section 6.2
- piezoelectric materials, see section 6.3

In trying to find useful electrooptic materials, we found the "Optoelectronic Materials Center". This center is a collaborative program involving the university of New Mexico, Stanford University, and the California Institute of Technology. Sandia National Laboratories and the MIT Lincoln Laboratory are also involved. Their program emphasizes three application areas: (1) diode-based visible sources, (2) two-dimensional optical interconnects, and (3) high-speed optoelectronics. They are not presently investigating the type of electrooptic materials we require.

6.1 Electrooptic materials

For a cubic crystal (for instance $Bi_4Ge_3O_{12}$ with the [100] orientation normal to the plate), the light phase retardation is proportional to the voltage difference between the two faces of the crystal and totally independent of the crystal thickness and of the field distribution in the crystal (see Zhu *et al.* [122]).

For a non-cubic crystal, the effect is also proportional to the voltage difference between the two faces of the crystal. However, the proportionality constant between the electrooptical effect and the applied voltage depends critically on the crystal cut orientation (see Berezhnoi [9].

Tremblay and Meyrueix [108] list the desired characteristics of an electrooptical for electric field sensing, which we repeat. The crystal must

- be available in large dimensions (since a PCB may be large), and not too fragile
- have a low absorption
- have a low diffusion
- have low linear birefringence
- have minimal temperature variations
- have resistivity greater than 10^{10} Ω-cm
- have dielectric constant lower than 100
- have a transverse electrooptical effect 10 times lower than the longitudinal electrooptical effect (to have acceptable cross-talk)

Tremblay and Meyrueis then indicate that they have not yet found a material with all of these properties. Tremblay *et al* [109] have summarized information about available materials, this information is reproduced in table 11.

Material	Electrooptic coefficient (units of 10^{-6}/V)
Inorganic crystals: $LiNbO_3$	$r_{33} = 30$
Inorganic crystals: KDP	$r_{41} = 8.77$ $r_{63} = 11.0$
Inorganic crystals: KTP	$r_{33} = 35.0$ $r_{13} = 8.8$ $r_{23} = 13.3$
Poled polymers: polyimide Guest-Host	$r_{11} = 30$
Neutral organic crystals: MMONS	$r_{33} = 40$
Neutral organic crystals: MNA	$r_{11} = 67$
Organic salts: DAST	$r_{11} = 400$

Table 12: Parameters for some electrooptical materials (from Stewart [103])

Parameter	Units	Value
r_{22}	10^{-12} meters/Volts	≈ 5
n_0	(dimensionless)	≈ 2.3

Table 13: Electrooptic parameters for lithium niobate (from Weis and Gaylord [119])

The article by Stewart[103] gives values for electrooptic coefficients which are summarized in table 6.1. The material DAST which has the largest electrooptical coefficient is presently available as raw crystals, of approximate size 1 mm × 5 mm × 5 mm.

Weis and Gaylord [119] lists many parameters, including electrooptical parameters, for lithium niobate. Some of the values they quote are in table 13 (these values are used in section 7.4.1).

6.2 Magnetooptic materials

By the magnetooptical "effect", we usually mean either the Faraday effect or the Kerr effect .[32] The Kerr effect occurs when an incident light ray in reflected from the surface of a magnetooptical material. The Faraday effect occurs when a light ray traverses a magnetooptical material.

6.2.1 Faraday effect

The relevant parameter controlling the magnetooptical rotation of the polarization vector for the Faraday effects is the Verdet constant, V (also called ρ in some older books). We have the formula:

$$V = \alpha/tB\cos\theta \tag{8}$$

where α is the total angle, t is the thickness of the substance through which the light beam passes, B is the magnetic induction field, and θ is the angle between the direction of the magnetic field and the path of light (see Cullity [24]).

The Verdet constant typically is between 1 and 300 in units of radians per meter per Tesla.[33] Section 6.2.2 surveys the Verdet constant for diamagnetic and paramagnetic materials. For these types of materials, it is possible to have a Verdet constant of approximately 250 radians/meters-Tesla. Section 6.2.3 surveys the Verdet constant for diluted magnetic semiconductors. For these types of exotic materials, it is possible to have a Verdet constant of approximately 100,000 radians/meters-Tesla.

[32] There is also a Cotton–Mouton effect, which we shall not describe.

[33] Note that some older sources use the units of minutes/cm–Gauss. The conversion is 1 minute/cm–Gauss= 290.9 radians/meter–Tesla.

We conclude that the largest Verdet constant, for an ordinary material, that we may expect to use for our application is $V \approx 250$ radians/meters-Tesla. This is the value used in section 7.5.1 where comparisons are made. We will sometimes refer to the possibility of a material with $V \approx 100,000$ radians/meters-Tesla.

6.2.2 The Verdet constant of diamagnetic and paramagnetic materials

In a forth-coming reference book, a chapter will be devoted to modern magnetooptical materials. Values of the Verdet constant for diamagnetic, paramagnetic and ferromagnetic, ferrimagnetic, and antiferromagnetic materials are given in Deeter *et al.* [29]. In that chapter we find that most materials have a larger Verdet constant at infrared wavelengths than at visible wavelengths. From Deeter's chapter:

- table 8.2 ("Verdet constants of commercial diamagnetic glasses") the largest value we observe is for "SF 59" for which $V = 28.5$.
- table 8.4 ("Verdet constants of noncommercial diamagnetic glasses") the largest value we observe is for a mixture of 88.9% TeO_2 and 11.1% P_2O_5 for which $V = 57.1$.
- table 8.5 ("Verdet constants of diamagnetic crystals") the largest value we observe is for GaSe for which $V = 232$. Since this value was measured at a frequency near an absorption edge, it may be more practical the use the next largest values, which occur for CU_2O (for which $V = 147$) and GaP (for which $V = 154$).
- table 8.6 ("Verdet constants of some commercially available paramagnetic glasses") the largest value (in magnitude) we observe is for terbium borosilicate and for terbium borate for which $V = -71.0$.
- table 8.7 ("Verdet constants for other paramagnetic glasses") the largest value (in magnitude) we observe is for praesodymium metaphosphate for which $V = -39.6$.
- table 8.8 ("Verdet constants for representative paramagnetic crystals") the largest value (in magnitude) we observe is for EuF_2 for which $V = -262$.

It may be possible to use ferromagnetic materials as they have high Faraday rotation at room temperature. The material europium oxide (which is electrically semiconducting) has an equivalent Verdet constant of 400,000 at room temperature. This value was obtained by dividing the Faraday rotation at saturation magnetic field by the magnetic induction at saturation. The material $CrBr_3$ (which is electrically insulating) also has a large Verdet constant.

Note that at 16°C under sodium light, we have (Lide [65]) $V_{\text{zinc sulfide}} = 0.224$ min/cm–Gauss= 65 radians/m–T. (This material was referenced in our original proposal.)

Among the materials listed by Massey, Erickson and Kadlec [68] the material with the largest Verdet constant is the crystal terbium gallium garnet (TGG). This crystal is transparent in the visible and has low optical loss and permeability similar to other magnetooptic glasses. The cited value for the Verdet constant is -130 micro radians per centimeter per Gauss of magnetic field applied in the direction of optical propagation. (This is the same as -130 radians/m–T.)

6.2.3 The Verdet constant of diluted magnetic semiconductors

Samarth and Furdyna [94] describe a class of materials that exhibit very large Faraday rotation, especially at low temperature. These materials are named "semimagnetic or diluted magnetic semiconductors". The values are very dependent on optical wavelength and temperature. They are usually paramagnetic at room temperature. The values of the Verdet constants vary strongly with the temperature and optical wavelength. Samarth and Furdyna [94] describe a material with a singularly large Verdet constant. The legend in figure 8 of that paper states that for 0.351 cm of the material $Cd_{1-x}Mn_xTe$ (with $x = 0.23$), at a temperature of 5°K, a field of 5 kiloGauss induced a rotation angle of more that $-8000°$. Converting to radians, dividing by the thickness and then dividing by the magnetic field strength, the Verdet constant is found to be

$$V \approx \frac{(8000 \text{ degrees}) \left(\frac{2\pi \text{ radians}}{360 \text{ degrees}}\right)}{(0.3515 \text{ cm })(5 \text{ kiloGauss})} = 79,000 \ \frac{\text{radians}}{\text{meter-Tesla}}$$

Parameter	Units	PZT4	PZT5A	PZT5H	PZT8
ϵ_{33}	—	1300	1700	3400	1000
d_{33}	10^{-2} Å/V	289	374	593	225
d_{13}	10^{-2} Å/V	−123	−171	−274	−97
d_{15}	10^{-2} Å/V	496	584	741	330
T_{Θ}	°C	328	365	193	300
k_{33}	—	70	0.705	0.752	0.64
ρ	g/cm^3	7.5	7.75	7.5	7.6

Table 14: Parameters for some ceramic piezoelectric materials (from Dorf [31, page 1089])

The Samarth and Furdyna [94] paper mentions that Verdet constants for other materials that are as high as 100,000 have been reported.

At room temperature a value of −2400 might be achieved with the material $Cd_{1-x}Mn_xTe$ at a particular wavelength (see Deeter *et al.* [29]). A newly available crystal BIG[34] (see Matsuda *et al* [69]), has the value $V_{BIG} = -0.806$ min/cm–Gauss= 234 radians/m–T at 1300 nm and room temperature.

6.3 Piezoelectric materials

Initially available piezoelectric materials were single crystal ceramics, such as quartz. In the last 20 plus years, though, piezoelectric materials have been constructed from polymers. Polymer piezoelectric materials allow thin sheets to be constructed.

The most popular presently used ceramic piezoelectric material is the family of PZT materials (PZT stands for lead–zirconate–titanate). While these are brittle, they have large piezoelectric effects. From Dorf [31, page 1089]) we have created table 14, which has a list of relevant constants for different PZT materials. Another recent review of piezoelectric materials is in Davis [28].

Almost any polar polymer can be made to be piezoelectric. This involves heating the material to above it's glass temperature, align the molten material with an electric field, then cool the substance. This process is called "poling". The degree of piezoelectricity is proportional to the amount of dipole alignment obtained.

A popular piezoelectric polymer is polyvinylideine fluoride (PVDF). PVDF is an electrorestrictive polyurethane which can be poled to become piezoelectric. For more details, see Wang *et al.* [117]. This material has a strain constant of $d_{33} \sim 20 \times 10^{-12}$ m/Volt. Note that since this material can hold a permanent polarization, it does not require conductive sheets on both sides.

The material Nylon 7 can be made piezoelectric, and it has a higher operating temperature before it loses it's piezoelectric properties. While there are other piezoelectric materials in the research labs, their properties are not too different from PVDF.

Many companies fabricate piezoelectric material:

- Material Systems[35] constructs ceramic sheets of piezoelectric materials with cones on them, by an injection molding process. The cones are typically 2–3 mm high, and about 2 mm apart. In section 7.3.2 we will perform some estimates using this material. When we do, we will assume the dimensions of the cones to be: height 2.5 mm, diameter 2.5 mm, and spacing 4 mm. With a compliance value of $s_{33} = 20.7 \times 10^{-12}$ meters squared per Newton, this configuration of the material corresponds to a bar wave resonant frequency of approximately 150 KHz.
- Ceranova[36] constructs ceramic sheets of piezoelectric material by pouring a resin onto a substrate.
- PVDF is manufactured by AMP[37]
- Voided PVDF is manufactured by ThornEMI (this material is available from Pennwalt, Pennsylvania).

[34]BIG stands for epitaxially grown bismuth-substituted yttrium-iron-garnet
[35]Material Systems Inc., 521 Great Road; Littleton, MA 01460
[36]Ceranova, Hopedale, MA
[37]AMP, Valley Forge, PA, 215/666–3500

7 Performance of Techniques for Visualizing EM Fields

In this section we describe the applicability of each of the different technologies under study that could, in principle, be used to visualize electromagnetic fields generated by circuit boards.

1. direct thermal imaging of electromagnetic field (see section 7.2)
2. electrodynamic force technique (see section 7.3)
3. electrooptical technique (see section 7.4)
4. magnetooptical techniques (see section 7.5)
5. piezoelectric techniques (see section 7.6)

Two of these techniques, the electrodynamic technique and the piezoelectric technique require that the motion of a moving plate be determined. The two thermal imaging techniques require that an infrared field be detected. The remaining techniques require that a sensor interrogate each spot on a non-moving layer.

A summary of the results from this section may be found in table 16 on page 67.

7.1 Comparison assumptions

Ideally, we would like to analytically model the electromagnetic field radiated from a portion of a printed circuit board, and to use that model to evaluate our end-to-end design before obtaining more accurate values from a finite-element formulation. This is very difficult, however, as Laroussi and Costache[62] demonstrate:

> "In a printed circuit board environment, the solution domain is highly inhomogeneous, and analytic expressions for design parameters are very difficult to obtain, even for the simplest configuration."

Hence, in section 3 we created and studied a simple geometry in order to determine approximate field values. That section also produced graphs showing typical fields. Section 3 conclusions are contained in section 3.6 (see, in particular, table 7). Using those conclusions, and the physical restrictions described in section 5, we will now determine the performance of the different technologies under study. When comparing the different technologies, we must assume parameter values for each technique. We summarize all of these assumptions in table 15 on page 53.

7.2 Direct thermal imaging

Aside from the heating of a piezoelectric material in a slurry (see the last section) a circuit board could be directly imaged thermally. A computation similar to that in the last section can be performed very easily. The power dissipated (as heat) on a single trace will be $P = I^2 R_s$, where R_s is the series resistance of the wire. For low frequency resistance of the wire, with the skin effect neglected, $R_s = \rho L / \pi r_0^2$, where ρ is the resistivity (see section C.2.1). For a trace of length L and half-width r_0, the power dissipated per unit area will be $P/2Lr_0$. In thermal equilibrium, the energy radiated by the trace, per unit area, is given by the Stefan–Boltzman law (see Halliday and Resnick [46, equation 47–3]):

$$\frac{\langle P_{\mathrm{OUT}} \rangle}{\text{unit area}} = R = e\sigma T^4 = \frac{I^2 \rho}{2\pi r_0^3}$$

where e is the emissivity and σ is the Stefan–Boltzman constant. Assuming

- The value $\rho = 1.53 \times 10^{-8}$ Ω-meter from table 5
- The value $e = 1$ from table 5
- The value $r_0 = 0.2$ mm from table 5
- The value $I = I_1 = 0.02$ amps from table 5
- The value $V = V_1 = 2.5$ Volts from table 5
- The value $\sigma = 5.67 \times 10^{-8}$ watt/(meter^2)($^\circ$K)^4 from page 73

All techniques	
radian frequency of electromagnetic field on card	ω =100 MHz
Direct thermal imaging	
resistivity (appropriate for copper)[a]	$\rho = 1.53 \times 10^{-8}$ Ω-meter
emissivity[b]	$e = 1$
Electrodynamic technique	
density[c]	$\rho = 7.8$ gm/cc
current density[d]	$J^* = 100, 00$ amps/meter
Electrooptical technique	
Interaction length with field	$L = 2$ mm
Interferometric techniques	
wavelength of light	λ =633 nm
Magnetooptical techniques	
Verdet constant[e]	$V = 250$ radians/meter-Tesla
Piezodynamic techniques (slurry and sheet)	
emissivity[f]	$e = 1$
proportionality of strain to voltage[g]	$d_{33} = 285 \times 10^{-12}$ meters/Volt
dissipation factor[h]	$\eta = 0.02 \times 10^{-15}$
stiffness[i]	$K = 2.5 \times 10^{11}$ Newtons/meter^2
total volume per unit area of crystals[j]	$V_{\mathrm{PE}} = 0.0005$ meter^3/meter^2

Table 15: Assumed parameters when comparing different technologies (in addition to those in table 5)

[a] from table 20
[b] The value given is the theoretical maximum.
[c] This value is typical of steel.
[d] See section C.2
[e] See section 6.2.1.
[f] The value given is the theoretical maximum.
[g] The value given is for PZT4 (see Morgan Matroc [72]).
[h] From Morgan Matroc [72] the values for PZT4 (PZT5) are $\eta = 0.02$ (0.004) times 10^{-15}.
[i] This value is typical of steel.
[j] The value chosen is equivalent to a solid layer of piezoelectric material 0.5 mm thick in the sensing sheet (which itself is assumed to be $h = 2$ mm thick)

we find that the temperature on the trace is given by

$$
\begin{aligned}
T &= \left(\frac{\frac{(0.02 \text{ amp})^2 (1.53\times 10^{-8}\ \Omega\text{-m})}{2\pi (0.2 \text{ mm})^3}}{(1)\left(5.67 \times 10^{-8}\ \frac{\text{watt}}{(\text{meter}^2)(^\circ\text{K})^4}\right)} \right)^{1/4} \\
&\approx 40^\circ\text{K}
\end{aligned}
$$

This is a large signal that can be readily measured. In fact, this technique has been used for measuring electromagnetic fields (see section 4.12).

7.3 Electrodynamic force technique

Consider a thin flat metallic sensing sheet containing a surface current that is supported vertically (in a vacuum). Assume that the plate has a surface current density of $\mathbf{J}^*$. If there is a prevailing magnetic field $\mathbf{B}$, then the force exerted on the sheet by the magnetic field is $\mathbf{F} = \mathbf{J}^* \times \mathbf{B}$ (see, for example, Jackson [50, equation (5.12)]). When applying this technology to circuit boards, $\mathbf{B}$ is the magnetic field produced by currents in the circuit board. See figure 24 for a typical geometry.

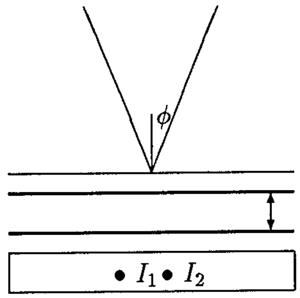

Figure 24: The physical apparatus for plate deformation (electrodynamic and piezoelectric techniques)

We presume that the sensing sheet is a conductor that contains a surface current parallel to the wires: $\mathbf{J}^* = J^*\mathbf{k}$. Then the force per unit area on the sensing sheet in this technique is given by

$$\mathbf{F}^* = \mathbf{J}^* \times \mathbf{B}_m = B_m(-\sin\theta_m \mathbf{j} - \cos\theta_m \mathbf{i})J^*$$

We define the vertical component of that force to be F_m^*. That is, $F_m^* = \mathbf{F}^* \cdot \mathbf{j} = -B_m \sin\theta_m$. The total force per unit area on the sheet, due to the two wires, is then $F^* = F_1^* + F_2^*$.

To have the sheet respond quickly to the ambient magnetic field, we will presume that the plate acts as a "limp mass". This means that the inertia effects of the plate are small, see page 76. Further, we presume that the currents vary sinusoidally as follows: $\mathbf{i}_m(t) = I_m e^{-i\omega t}$. Note that it is the choice of ω that determines whether or not the sensing sheet will act as a limp mass. If m_p is the mass per unit area of the plate (defined to be density times thickness) then the dynamics of the sensing sheet are given by (see equation 19):

$$-m_p\omega^2 u \approx F^* \tag{9}$$

where u represents the vertical motion of the plate at a specific location. Solving for u we obtain

$$u = \frac{F^*}{-m_p\omega^2} = \frac{-B_1\sin\theta_1 - B_2\sin\theta_2}{-m_p\omega^2}J^* = \frac{\mu_0}{2\pi m_p\omega^2}\left[I_1\frac{\sin\theta_1}{r_1} + I_2\frac{\sin\theta_2}{r_2}\right]J^* \tag{10}$$

Using values of $\rho = 7.8$ gm/cc and $J^* = 100,000$ amps from table 15, and the geometry from figure 5, we created the plot in figure 25. For the graph with the keyword "common" we took $I_2 = I_1$, for the graph with the keyword "differential" we took $I_2 = -I_1$. The value of J^* used is not unreasonable; in section C.2 it is shown that if the sensing sheet is constructed of a material similar to copper, than a value of $J^* = 200,000$ amps/meter is possible.

There are now at least two ways in which the surface deformation can be detected:

- By using scanning laser interferometry techniques (see section 7.3.1).
- By placing a sheet of piezoelectric material on top of the conducting sensing sheet and measuring the voltage induced by the surface deformation (see section 7.3.2).

7.3.1 Optical detection

From table 10 we observe that commercial off the shelf equipment can, in principle, measure surface height to an accuracy of 6 nm. This is adequate to resolve the displacement of the sensing sheet shown in figure 25. However, from table 10 we observe that a measurement acquisition time of 0.1 seconds is required. In section C.2.1 we have shown that, in this time, the material will—due to thermal expansion alone—expand by 38 nm (see table 21). This thermal size change dominates the effect that we are attempting to measure.

We conclude that optical detection of a sheet deformed through the electrodynamic force is not a good electromagnetic field measurement device.

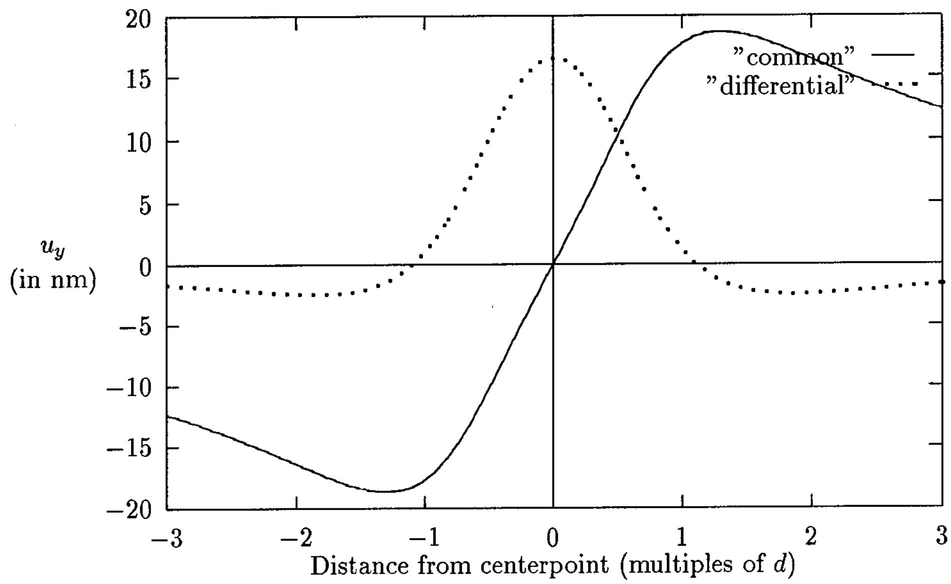

Figure 25: Vertical displacement of sensing sheet

7.3.2 Piezoelectric detection

It is also possible to use piezoelectric materials to perform surface height measurement. If a sheet of piezoelectric material is bonded to the conducting sensing sheet that experiences the electrodynamic forces, then the conducting sheet deformation will put a strain on the piezoelectric sheet. This strain induces a voltage that can be measured. Assuming

- The value $I_1 = 0.02$ amps from table 5
- The value $I_2 = 0$ amps (that is, there is only one wire)
- The value $r_1 = h = 2$ mm (so that the sensing point is directly above the wire)
- The value $J^* = 100,000$ amps/meter from table 15
- The nominal value $\theta_1 = \pi/2$
- We will assume that the sensing sheet is backed by a sheet of piezoelectric cones similar to those produced by Materials Research (see page 51 for assumed parameters). Note that the operating frequency, in this case, is below the resonant frequency of the piezoelectric sheet (which is about $\omega = 150$ KHz).

then equations 9 and 10 predict that the force per unit area on the sheet will be approximately $F = 0.2$ Newtons per square meter. In the conventional decibel scale this pressure is 104 dB (with respect to a micro-Pascal squared).

We next compute the charge generated by the piezoelectric rod, which is assumed to be holding the current sheet motionless. The total force on one rod is equal to $F_T = F(4\text{mm}^2) = 3.2 \times 10^{-6}$ Newtons. Therefore, the charge on a single rod is given by $Q = F_T d_{33}$. Using the value of d_{33} for PZT5H (from table 14) we find $Q = 2 \times 10^{-15}$ Coulombs.

From the dimensions of the piezoelectric rods and properties of the piezoelectric material we find that the capacitance of a single rod of PZT5H is equal to C_{PZT} =(permittivity of the material)*(area)/(height)= 20 pico-Farads.

We will assume a standard high quality FET amplifier to be excited by this charge. A good low–noise amplifier such as the one developed by Colaruotolo [22] has an input impedance of $R_{in} = 240\text{M}\Omega$ in parallel with $C_{in} = 200$ pico-Farads. An equivalent circuit that may be used for measurement computations is given in figure 26. For frequencies larger than $1/2\pi R_{in} C_{in} \approx 3$ Hz the admittance of the resistor can be neglected.

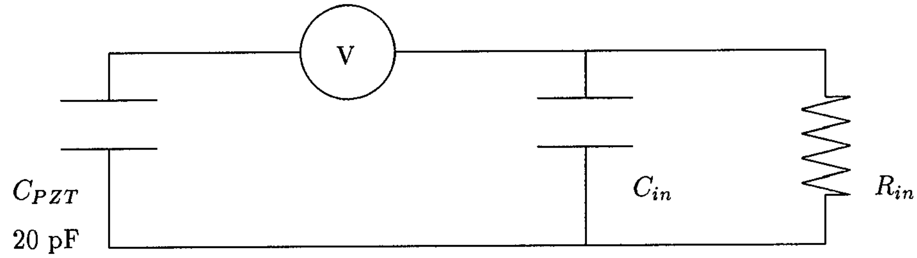

Figure 26: Equivalent electrical circuit of measurement system

From the above circuit model, the charge generated by one rod would produce a voltage of about $V \approx Q/(C_{in} + C_{PZT}) = 9\ \mu$Volts into this input impedance. Hence, the signal energy is $S = 81 \times 10^{-12}$ Volts^2. The spectral density of the noise floor of this amplifier is about -171 dB with respect to a Volt squared per Hz. The noise energy is given by the noise floor times the bandwidth (which is assumed to be 100 KHz) to produce $N = 8 \times 10^{-13}$ Volts^2. Finally, the signal to noise ratio is approximately $S/N \approx 100 = 20$ dB.

These estimates indicate that using individual piezoelectric rods to measure currents would be effective in the frequency range 3 Hz to 100 KHz. (With the implicit assumption that most of the spectral energy of the signal is within this frequency band.) The device might be used to measure currents at higher frequencies by using sheet currents of a higher frequency to create mixing effects, similar to the approach described in section 4.9 describing magnetostrictive sensors.

7.4 Electrooptical technique

One way to detect the in-plane electric field is to exploit the change in index of refraction of electrooptical materials caused by the electric field (similarly, the change in index of refraction of magnetooptical materials caused by the magnetic fields can be detected). This approach will allow a small region of a circuit board to be imaged at a time.

Because the traces on a circuit card are, for the most part, aligned at right angles we know in advance in which directions the electromagnetic fields will reside. This makes it possible to align the polarization of the optical field with respect to that of the electric field in the card. Note that, with this technique, only the in-plane electric field is measured. Because of this, the measurements of the field of a wire is taken displaced slightly from the wire.

The geometry of the apparatus is illustrated in figure 27. The standard way to detect a phase shift induced by the electrooptical material is to use a Mach–Zehnder interferometer (see, for example, Born and Wolf [12]). We assume an optically reflective film which is thin enough to allow the electric field of the circuit card to penetrate the electrooptic material.

After submitting our original proposal, we discovered that the concept of using the electrooptic technique to measure electric fields has been used before. We have found two references to previous work, by a group at Schlumberger (see section 4.4.1), and by a group at SRICO (see section 4.4.2).

7.4.1 Analysis of electrooptical techniques

This section demonstrates how the phase shift caused by the electrooptical (Pockels) effect can be computed.

The incremental phase shift, Γ, of an optical wave caused by a transverse electric field in one branch of an interferometer of length L is given by (see Massey *et. al* [68]):

$$\Gamma = 2\pi n_0^3 r_{22} \frac{EL}{\lambda}, \tag{11}$$

where r_{22} is the electrooptic tensor coefficient to which the electric field, E, is applied. The symbol λ designates, as usual, the free-space wavelength of the light wave. Assuming

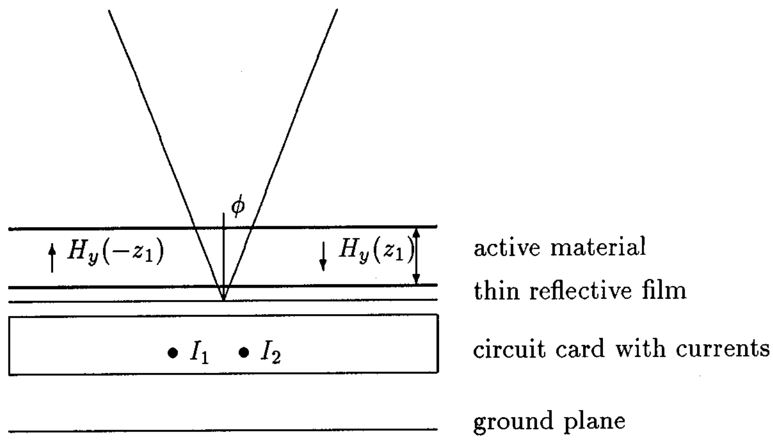

Figure 27: The physical apparatus for phase changes using electrooptical or magnetooptical materials

- The value $E = 100$ Volts/meter from table 7.
- The material is lithium niobate (n_0 and r_{22} are taken from table 13 on page 49)
- The value $\lambda = 633$ nm from table 15.
- The value $L = 2$ mm from table 15.
- The electric field E is constant throughout the length, L, of the sensor.

we determine that the incremental phase shift is

$$\begin{aligned}\Gamma &\approx 2\pi(2.3)^3\left(5\times 10^{-12}\,\frac{\text{meters}}{\text{Volt}}\right)\frac{\left(100\,\frac{\text{Volts}}{\text{meter}}\right)(2\text{ mm})}{633\text{ nm}}\\ &= 120\ \mu\text{radians}\end{aligned}$$

This phase shift can be measured with existing sensitive devices (see section 5.2.1). This makes the electrooptical method very promising. In section 7.4.2 we describe how the sensor that SRICO makes can be modified for our specific needs.

7.4.2 Modification of the SRICO electrooptical sensor

Note that section 4.4.2 contains an overall description of an electrooptical field sensor device developed by SRICO. This section describes how this sensor may be adapted to our needs.

We have held detailed discussions with SRICO about the applicability of their product for our needs. SRICO has indicated that their design (as shown in figure 18) can be modified as shown in figure 28. In this modified design (1) the "oppositely poled" electrooptical material is at the right end of the device, and (2) the light rays are reflected from a polished surface coated with a dielectric mirror. In this case, the circuit board being measured would be to the right of the illustration.

A single point sensor can be difficult to use for our application (see section 5.4.2). However, the sensors shown in figure 28 can be constructed as a linear array, as shown in figure 29. Fabrication requirements (the size of a 3 inch silicon wafer) could restrict the length of this array to about 2.5 inches (which could contain, possibly, 100 individual sensors). Since the array is only 1 mm thick, it is possible to laminate several arrays together to obtain a two-dimensional array of sensors. If 100 arrays were combined the resulting two-dimensional array could, conceivably, have 10,000 sensors in an approximate area of 2.5 inches by 4 inches. This many sensors in 10 square inches results in an average of 30 sensors to the linear inch. Note that this is a factor of ten spatial improvement over the EMSCAN device (see section 4.3).

Section 4.4.2 indicates that an electric field of 0.2 V/m$\sqrt{\text{Hz}}$ was detectable with SRICO's standard sensor. Assuming

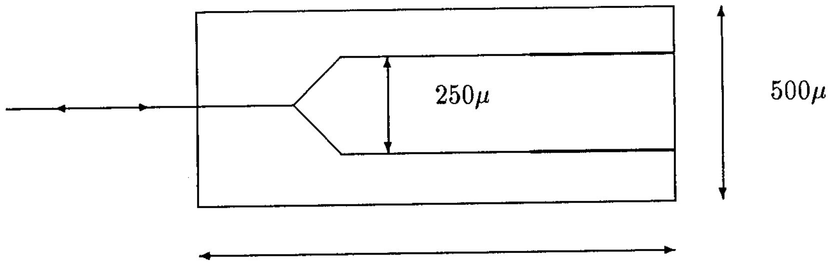

Figure 28: A modified SRICO electromagnetic field sensor

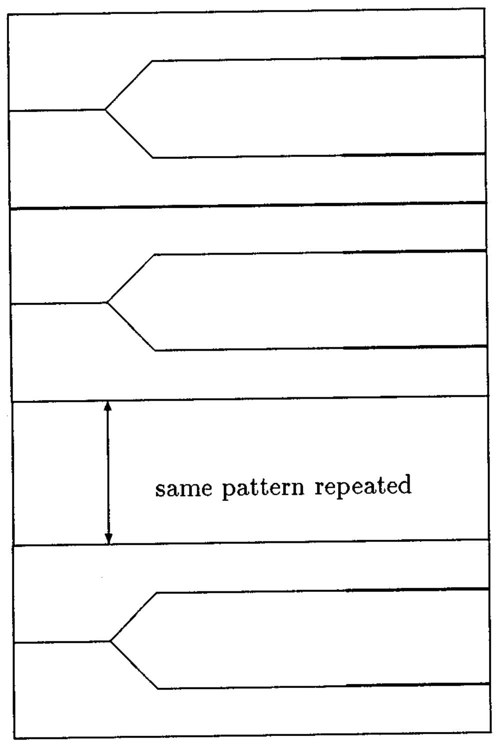

Figure 29: An array of modified SRICO electromagnetic field sensors

- The modified sensor has the same detectability as the sensor in section 4.4.2
- The electric field is constant throughout the active portion of the sensor.

then the modified SRICO sensor, with a resolution bandwidth of 10^4 Hz, would be able to detect 20 Volts/meter in that bandwidth. Since this bandwidth is achievable (see section 5.5), and since this electric field is smaller than we need to detect,[38] we should be able to detect a circuit board's electromagnetic field with this approach.

Note that more sensitive detection of the phase angle, which is achievable with existing technology, will result in an improved minimum electric field detectability.

We conclude that electrooptical sensors are good electromagnetic field measurement devices for circuit board applications.

[38] From table 7 we need to measure a minimum field of 50–150 Volts/meter.

7.5 Magnetooptical techniques

Section 4.8 contains a discussion of several different types of electromagnetic field sensors that have been constructed using magnetooptical materials. The following sub-sections show how the different magnetooptical effects may be computed. The Faraday effect sensor computation is in section 7.5.1. The state of the art for a Kerr effect sensor is contained in section 4.8.1.

7.5.1 Application of Faraday effect

In this section we estimate the rotation of the polarization of a linearly polarized optical ray incident on the sheet of magnetooptical material at a grazing angle θ_i which is transmitted into the sheet, reflected off the bottom of the sheet and then passes back up through and out of the sheet.

The formula in equation 8 (see page 49) can be solved for α:

$$\alpha = VtB\cos\theta \tag{12}$$

Assuming

- The nominal value $\theta = 45°$
- The value $t = 2$ mm from table 1
- The value $B = 0.5 \times 10^{-6}$ Tesla from table 7
- The value $V = 250$ radian/meter-Tesla from table 15
- The magnetic field is constant throughout the depth of travel of the light ray.

then a simple estimate of the rotation angle is given by

$$\begin{aligned}\alpha &\approx \left(250\ \frac{\text{radian}}{\text{meter-Tesla}}\right)(2\ \text{ mm})(5\times 10^{-7}\ \text{Tesla})(0.707)\\ &= 0.2\mu\ \text{radians}\end{aligned} \tag{13}$$

A rotation angle of this amount is nearly at the limit of what can be currently achieved (see section 5.2). A more detailed calculation is now given.

The total polarization rotation is determined by integrating the differential polarization rotation along the full length of the ray path in the material. The differential polarization rotation is equal to the product of the Verdet constant, the component of the magnetic field parallel with the optical wavevector, and the differential length.

We will assume that the incident ray enters the magnetooptical sheet at $-x_1$ and leaves at $+x_1$, after reflecting off the underside of the sheet just above the current carrying trace at $x = 0$ (see figure 30). We will approximate the integral along the ray path by performing the integral along a path of constant depth (i.e., the integral will be evaluated along the dark line within the sensing sheet). Along this line the horizontal component of the magnetic field is $H_x = (I/2\pi r)(y/r)$ where r is the distance from the trace to the evaluation line. Using $B_x = \mu_0 H_x$, the ray-path integral for the polarization rotation angle α, due to the upper trace, is then given by the approximate expression,

$$\begin{aligned}\alpha_{\text{upper trace}} &= \int_{x_1}^{x_1} VB_x\,dx \approx \frac{\mu_0 VI}{2\pi}\int_{x_1}^{x_1}\frac{y_0-\beta}{r^2}\,dx\\ &= \frac{\mu_0 VI}{2\pi}\int_{-x_1}^{x_1}\frac{y_0-\beta}{x^2+(y_0-\beta)^2}\,dx = \frac{\mu_0 VI}{\pi}\tan^{-1}\left(\frac{x_1}{y_0-\beta}\right)\end{aligned}$$

Note that when an image trace is included (which models the ground plane), the effect of the image current is to add an oppositely signed contribution which tends to cancel the rotation. Because the image current is farther away, the angle will be smaller and the cancellation will not be complete. The result is given by the expression,

$$\begin{aligned}\alpha &= \alpha_{\text{upper trace}} + \alpha_{\text{lower trace}}\\ &\approx \frac{\mu_0 VI}{\pi}\left[\tan^{-1}\left(\frac{x_1}{y_0-\beta}\right) - \tan^{-1}\left(\frac{x_1}{y_0+\beta}\right)\right] = \frac{\mu_0 VI}{\pi}\tan^{-1}\left(\frac{2x_1\beta}{y_0^2+x_1^2-\beta^2}\right)\end{aligned} \tag{14}$$

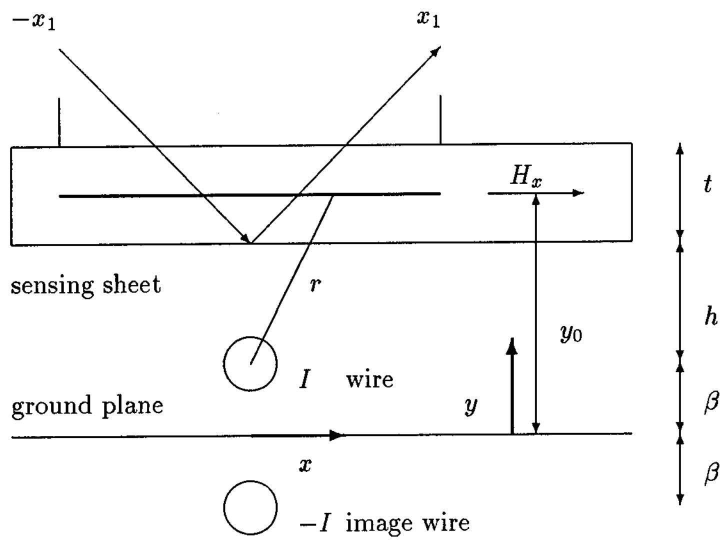

Figure 30: Geometry of detailed electrooptical computation

Using $y_0 = h + \beta + t/2$ and assuming

- The value $x_1 = 2$ mm
- The value $t = 2$ mm from table 1.
- The value $\beta = 0.5$ mm from table 5
- The value $h = 2$ mm from table 5
- The value $B = 0.5 \times 10^{-6}$ Tesla from table 7
- The value $V = 250$ radian/meter-Tesla from table 15

we can compute

$$\begin{aligned}\alpha &= \frac{\left(4\pi \times 10^{-7} \frac{\text{weber}}{\text{amp-meter}}\right)\left(250\ \frac{\text{radians}}{\text{meter-Tesla}}\right)(0.02 \text{ amps})}{\pi} \\ &\quad \times \tan^{-1}\left(\frac{(2 \text{ mm})^2 + (0.5 \text{ mm})^2 + (3.5 \text{ mm})^2}{2(2 \text{ mm})(3.5 \text{ mm})}\right) \\ &\approx 0.2\mu \text{ radians}\end{aligned}$$

We conclude that a more detailed computation arrives at approximately the same rotation angle.

Note that if the Verdet constant were taken to be equal to $V = 100,000$ radians/meter-Tesla (see section 6.2.1) then the rotation angle would increase to 100 μ radians.

7.6 Piezoelectric techniques

Piezoelectric materials respond to an electric field by creating a strain (see Dorf [31, chapter 47]). Any mechanical object is governed by the following relationship between stress (**S**, relative elongation) and strain (**T**, force per unit area) $\mathbf{S} = \mathbf{sT}$, where **s** contains the coefficients connecting the two quantities. Note that **S** and **T** are second rank tensors and **s** is a fourth-rank tensor. For a piezoelectric material this relationship is modified to become

$$\mathbf{S} = \mathbf{sT} + \mathbf{dE}, \tag{15}$$

where **E** is the electric field tensor and **d** are additional coefficients that have been tabulated for many materials.

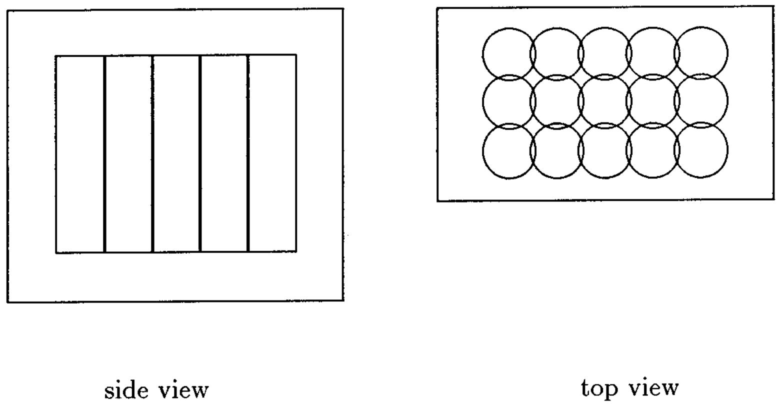

Figure 31: A sensing sheet composed of many rods of piezoelectric material

Note that if a piezoelectric material is maintained in a stress free environment (i.e., $\mathbf{T} = 0$), then the maximum strain is proportional to the applied electric field, with the constants of proportionality being $\mathbf{d}$ (that is $\mathbf{S} = \mathbf{dE}$, see equation 15). For thin rods, this can be approximated by the simple relation $S = d_{33}E$.

This relationship implies that an electric field will produce a strain in a piezoelectric material. There are two ways this can be used in the current application

- If a thin sheet of piezoelectric material is exposed to an ambient electric field, then the sheet will deform (expand or contract) depending on the electric field. The deformation of the sheet may be obtained by laser interferometry.

  Details of this technique may be found in section 7.6.1.

- A possibility for the detection of an electric field is to sense to heat generated by a piezoelectric material. We imagine that a layered apparatus, containing a slurry of piezoelectric material, is placed over a powered circuit board. The electric fields produced by the components on the board will excite the piezoelectric material, causing it to alternately expand and contract.

  This periodic excitation will transfer heat to the slurry. This heat build-up may be detectable via infrared imaging, or by using materials that change color with temperature.

  Details of this technique may be found in section 7.6.2.

A recent article about computational results with piezoelectric materials is Zharii [121].

7.6.1 Piezoelectric sheet technique

To increase the maximum possible effect, we assume in this section that the sheet of piezoelectric material is composed of many tiny rods fused together, see figure 31. This is the technique that material scientists use to achieve maximum deformation of a piezoelectric material. If the sheet is maintained in a stress free support then we have, approximately, $S = d_{33}E$.

The total displacement, d, of the sheet will be given by $d = St = d_{33}Et$. If the sheet expands symmetrically, so that that the top and the bottom of the sheet move the same amount, then the displacement on the top surface d_s will be $d_s = d/2 = d_{33}Et/2$. Assuming

- The value $t = 2$ mm from table 1.
- The value E from table 7.
- The value d_{33} from table 15.
- The electric field is constant throughout the depth of the sensing sheet.

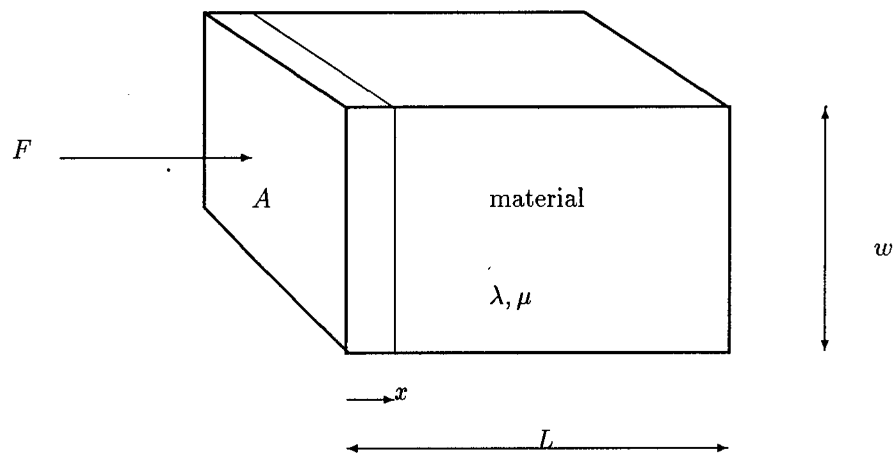

Figure 32: Isolation of a single piezoelectric crystal

then we determine the displacement on the top surface to be:

$$\begin{aligned} d_s &= \frac{1}{2}\left(285 \times 10^{-12}\frac{\text{meter}}{\text{Volt}}\right)\left(100\frac{\text{Volts}}{\text{meter}}\right)(1 \text{ mm}) \\ &= 0.14\text{Å} \end{aligned}$$

This tiny movement (a hydrogen atom is typically 0.5Å in size) will not be detectable.

We conclude that a piezoelectric sensing sheet is not a good electromagnetic field measurement device.

7.6.2 Piezoelectric slurry technique

Consider in isolation a single piezoelectric crystal that has a sinusoidal force F applied to a surface of area A (see figure 32). We assume that the piezoelectric crystal has the material parameters λ and μ.

The elastic work performed on the crystal by the action of the applied force is given by: $W_{\text{EL}} = \int_0^{x_1} F(x)\,dx$. The force is the product of the area and the pressure: $F(x) = AP(x)$. The pressure is given by $P(x) = \frac{x}{L}(\lambda + 2\mu)$ where the combination $\lambda + 2\mu$ is known in elasticity theory as the one-dimensional modulus. Defining the peak strain to be $S = -x_1/L$ (note that S will depend on the applied voltage) the work per unit volume is given by

$$\frac{\text{work}}{\text{unit volume}} = \frac{W_{\text{EL}}}{AL} = \frac{\lambda + 2\mu}{2}S^2$$

The "Q" of an oscillator is defined to be the peak energy divided by the power P_{IN} dissipated per radian: $Q = \omega W_{\text{EL}}/P_{\text{IN}}$. Re-writing this we obtain $P_{\text{IN}} = \omega W_{\text{EL}}/Q$. Writing the one-dimensional modulus in terms of real and imaginary parts, and defining $\eta = Q^{-1}$ (as usual in elasticity), we have

$$\lambda + 2\mu = K(1 - i\eta)$$

where K is real. The imaginary part accounts for the energy dissipation (the real part represents stored elastic energy). Using the fact that the material is undergoing sinusoidal oscillations (so that $x(t) = S\sin\omega t$, $v(t) = S\omega\cos\omega t$, and $F(t) = (\lambda + 2\mu)x(t)/2$), we can take averages to find that

$$\frac{\langle P_{\text{IN}}\rangle}{\text{unit volume}} = \langle \mathbf{F}\cdot\mathbf{v}\rangle = \frac{1}{2}K\eta\omega S^2 \tag{16}$$

This is the average power dissipated per unit volume per radian. Assuming we have a distribution of random piezoelectric crystals in the slurry with a total volume of V_{PE} per unit area then

$$\frac{\langle P_{\text{IN}}\rangle}{\text{unit area}} = \frac{1}{2}V_{\text{PE}}K\eta\omega S^2$$

The energy radiated away from the slurry, per unit area, is again given by the Stefan–Boltzman law:

$$\frac{\langle P_{\mathrm{OUT}} \rangle}{\text{unit area}} = R = e\sigma T^4$$

We now assume that the length of time work is performed on the slurry is

- small: compared to the thermal conduction time of the slurry
- large: large enough to reach equilibrium

and that the slurry is in thermal equilibrium (in which the power input equals the power output). This leads to the relationship $V_{\mathrm{PE}} K \eta \omega S^2/2 = e\sigma T^4$ or

$$T = \left(\frac{V_{\mathrm{PE}} K \eta \omega}{2e\sigma}\right)^{1/4} \sqrt{S} \tag{17}$$

If we assume that the piezoelectric crystal is stress-free then we have, approximately, $S = d_{33}|E|$. Hence, the temperature T varies as the square-root of the applied field E. Assuming

- The value E from table 7
- The values V_{PE}, K, η, ω, e from table 15 on page 53
- The value $\sigma = 5.67 \times 10^{-8}$ watt/(meter^2)($^\circ$K)^4 from page 73
- The electric field is constant throughout the depth of the sensing sheet

we calculate the equilibrium temperature to be

$$\begin{aligned} T &= \left(\frac{\left(0.0005\ \frac{\mathrm{m}^3}{\mathrm{m}^2}\right)\left(2.5 \times 10^{11}\ \frac{\text{Newtons}}{\text{meter}^2}\right)(0.02 \times 10^{-15})(2\pi \times 100 \times 10^8 \text{ radians})}{2(1)\left(5.67 \times 10^{-8}\ \frac{\text{watt}}{\text{meter}^2\ {}^\circ\mathrm{K}^4}\right)} \right)^{1/4} \\ &\quad \times \sqrt{\left(285 \times 10^{-12}\ \frac{\text{meters}}{\text{Volt}}\right)\left(100\ \frac{\text{Volts}}{\text{meter}}\right)} \\ &\approx 0.03^\circ\mathrm{K} \end{aligned}$$

While absolute temperature differences of this size are not difficult to detect, they are not easily performed on our system since the sensing sheet is very close to several heat producing elements on the circuit board (note that in [100], see page 39, a resolution on only 0.02°K was achieved).

We conclude that the use of a slurry containing piezoelectric materials is not a good electromagnetic field measurement device.

8 Visualization of the Electromagnetic Field

Independent of the technology used to determine the electromagnetic field, the net result of any of our measurement techniques will be a two-dimensional grid of scalar values, corresponding to fields on the surface of the circuit card.[39] This grid of scalar values can be visualized in any of a number of ways. Note that our image comparison problem is dramatically simplified by the fact that no orientation or scaling of images is required. This is because each image will be obtained by the same equipment, with each circuit board in the same orientation.

The simplest technique is to map a uniform gray scale to the scalar values obtained (with, say, black corresponding to the lowest field value and white corresponding to the largest field value). The maximum and minimum values in the gray scale could be determined dynamically from the data, or fixed in advance. Dynamic determination results in an image with a better contrast, while the latter technique is more useful for comparison of images. Since every measurement technique has a noise threshold, when using fixed values the lowest fixed field value should be larger than this noise threshold.

In section 2.6 we indicated that there may be large currents on the power traces and much smaller currents on the signal traces. Since the magnitude of the electromagnetic field is, ultimately, proportional to the currents, the power traces will create much larger fields than the signal traces. Hence, the gray scale values will be dominated by the power traces. They are probably of less interest since:

- Power traces are generally thicker than signal traces. This means that they are less likely to be defective.
- A digital circuit board will have many more signal traces than power races (although analog circuit boards will have only power traces).

Hence, it makes sense to perform two comparisons:

- First use a threshold that would allow all signal traces to be discarded, and verify that the power grid matches between two images.
- Then set a low enough upper threshold to discard the power traces. In the new images verify that the signal traces match between two images.

For comparison of visual images, we must distinguish between human and machine comparison. For human comparison:

- Many studies of human performance have been carried out. See, for example, Kibbe and Stiff [55]. For infrared images, see Sanders *et al.* [95].
- Humans can sense only about 6 bits of monochrome information, which corresponds to 64 gray levels. (Note that our measurement techniques vary in the number of bits of information produced.)

Machine comparison of images is a well studied problem, which generally goes under the name "matching". See, for example, Ballard and Brown [7, chapter 11]. There are many different approaches currently in use for matching images. One technique that we think is promising for our application uses the topology of the images (see section 8.1).

Note that the articles in Amit [3] and Bajcy and Kovacic [6] focus on the matching of medical images, such as X-ray images. This is very similar to the image matching required for this task.

[39] Since the fields are temporal, as the device continues to measure the field, a sequence of two-dimensional images will be generated. Since two sequences of images can be compared one-by-one, we now restrict attention to a single two-dimensional image.

8.1 Image comparison: topological method

The electromagnetic field values that are detected will generally be due to either components on the circuit board, or traces on the circuit board. By definition, these are connected to one another. Hence, if attention is focused on just the strongest fields, then this should form a connected graph (in the mathematical sense of the word, see, for example, Roberts [90]). This connected graph should be the same for different circuit boards. See the reports by Fleck [35] and Ranganath and Chipman [88]

The complete plan is then this:

- Fix a single threshold value which is above the noise floor of the sensing device.
- All values less than the threshold are set to white, all values greater than the threshold are set to black.
- Interpret the set of dark regions as a graph (composed, possibly, of several separate connected subgraphs)
- Determine if the graphs from two circuit boards are the same by determining if they are isomorphic. There are many routines available for determining the isomorphism of graphs, see, for example, Kobler *et al.* [56] or Gazit [40].
- If they are isomorphic, then declare a good comparison. If they are not isomorphic, then declare a bad comparison

It may also be possible to set several threshold values, and compare the graphs determined by adjacent thresholds. For example, if the raw image data has values from 0 to 256, then a graph can be determined from all those values within the range $[0, 63]$. A different graph would arise from those values within the range $[64, 127]$, etc. This may be useful if the data from different regions of the board are radically different in field strength. More details about image thresholding and segmentation may be found in any image processing book, such as Russ [91, Chapter 5].

We have not implemented the algorithms described above since we have not obtained images from our proposed sensing methods.

9 Conclusions

1. Advantages of Linear Sensing Technique

   Different sensor technologies studied in this report may be described as either linear (that is, the effect scales with the electromagnetic fields on the circuit board) or quadratic (that is, the effect scales with the square of the electromagnetic fields on the circuit board). Linear methods include electrooptical and piezoelectric techniques. Quadratic methods include the thermal techniques. For low power fields, the linear methods generate a much larger sensed signal than the quadratic methods, and therefore are more useful for circuit board applications.

2. Electrooptical measurement

   The most well documented technique for sensing high frequency electromagnetic fields employs electrooptic materials to generate an optical phase shift through the Pockels effect. This effect is one in which an applied electric field causes a change in the index of refraction. Imaging a circuit board would be done with an array of electrooptic waveguides located close to the circuit board. The normal electric field on the board would produce an optical phase shift in the light waves traversing the electrooptical waveguides. To detect the optical phase shift a Mach–Zehnder interferometer would be used with phase–coherent detection techniques. These detection techniques have been demonstrated in laboratory facilities. The effect will produce an amount of phase shift which we judge to be sufficient for imaging the fields on a circuit board.

3. Magnetooptic Faraday effect

   When used with materials having very large Verdet constants, the magnetooptic Faraday effect can provide amounts of polarization rotation of a linearly polarized optical beam which are comparable to the phase shifts produced by the electrooptic effect. Dilute magnetic semiconductors, a recently created kind of material, have extremely large Verdet constants, on the order of 100,000 when the material is held at very low temperature, i.e., 5 degrees Kelvin. Certain ferromagnetic semiconductors, such as europium oxide, have extremely large equivalent Verdet constants at room temperature and may provide suitable performance. An important feature of magnetooptic imaging is that the magnetooptic material is a simple sheet close to the circuit board.

4. High frequency measurements with heterodyne detection

   Several measurement techniques, which employ low frequency mechanical motion, have been shown to be effective when used in a heterodyne mode. In this mode, a high frequency field mixes with a high frequency field to be measured in a nonlinear device. The force at the difference frequency excites the device at it's resonance. Many of these heterodyne measurements have been demonstrated. The demonstrations have all been with large sensor devices, which would not provide the spatial resolution required for imaging the small scales on circuit boards. A heterodyne technique employing a matrix of small piezoelectric rods does have the potential for the required spatial resolution.

These conclusions are summarized in table 16 on the next page. They are listed in the order of their feasibility for near term application.

9.1 Recommended further work to develop imaging systems

The most important areas for further investigation are listed below in prioritized order.

1. Determine if and how the EMSCAN device (see section 4.3) will be modified to increase it's resolution. With a sufficient increase in resolution, it may be practical to use this product on low power digital circuit boards. This course of action might have the most immediate pay-back from the Air Force point of view.

2. Explore Schlumberger's plans to package and sell their patented measurement system which has been designed for the visualization of circuit board electromagnetic fields. (Their patent is less than one year old, see section 4.4.1.)

electrooptical technique	This technique appears to be very promising for imaging of low power digital circuit board electromagnetic fields. A sensor array concept that achieves a linear spatial separation of 0.03 inches has been described (recall that EMSCAN achieves only 0.3 inches). This is a high–frequency technique.
magnetooptical techniques	The polarization rotation angles obtainable with conventional diamagnetic and paramagnetic materials are near the limit of presently detectable polarization rotation angles. If dilute magnetic semiconductors at low temperature are used the polarization angle rotation will be about 100 times larger and comparable to the phase shifts produced by the electrooptical effect. Several ferromagnetic semiconductor materials may also provide large polarization rotation at room temperature. This is a high–frequency technique.
electrodynamic force technique	For piezoelectric detection this technique could work if the frequency of detection is between 3 Hz and 100 KHz, or higher (up to hundreds of MHz) if used in a heterodyne mode.
direct thermal imaging	This technique can be used directly, and applications for circuit boards have already been developed by others
electrodynamic force technique	For optical detection of the deformations, the measurement time for commercial off the shelf devices is too long (the material experiences significant thermal expansion during the measurement).
piezoelectric techniques	For the piezoelectric sheet technique the sheet deformations are too small to be detected. For the piezoelectric slurry technique the temperature rise is too small to be useful.

Table 16: Suitability of measurement techniques for imaging (conclusions from section 7)

3. Specify and select, in consultation with experts in the Air Force and in industry, a class of circuit boards and defining operating parameters. Relevant parameters needed for detailed sensor design will be measured from a representative of this class. This process will determine some of the parameters that were only estimated in this report, for example

   At which frequencies is the spectral energy concentrated?

   What is the trace separation on the circuit board?

   How close can the sensing sheet come to the circuit board?

4. Design and construct in conjunction with SRICO a prototype electromagnetic field sensor based on the electrooptical effect in the form of a linear array. The SRICO sensor appears to be adequate for the measurement of electric fields produced by a low power digital circuit board. While a two-dimensional array of sensors is the eventual product, it would be prudent to first construct a single linear array of sensors.

5. Determine the magnetooptical performance available from dilute magnetic semiconductor materials and from ferromagnetic semiconductors. While these materials show great promise, because of their large Verdet constants, many important practical parameters need to be explored.

A Bibliography

References

[1] *Reference Data for Radio Engineers.* ITT Handbook, 5 edition, 1968.

[2] Market measures up. *EBN*, page 54, 15 June 1994.

[3] Y. Amit. A nonlinear variational problem for image matching. *SIAM J. Sci. Compout.*, 15(1):207–224, January 1994.

[4] B. Archambeault. Predicting EMI emission levels using EMSCAN. *Proceedings of the IEEE International EMC Symposium*, August 1993.

[5] F. T. Arecchi and E. O. Schulz-DuBois, editors. *Laser Handbook.* North–Holland, Amsterdam, 1972.

[6] R. Bajcy and S. Kovacic. Multiresolution elastic matching. *Computer Vision, Graphics, and Image Processing*, 46(1–21), 1989.

[7] D. H. Ballard and C. M. Brown, editors. *Computer Vision.* Prentice-Hall, Inc, Englewood Cliffs, NJ, 1982.

[8] L. Balme, A. Mignotte, J. Monari, and P. Pondaven. New testing equipment for SMT (surface mounted technology) PC (printed circuit) boards. Technical report, Grenoble Univ, June 1988.

[9] A. A. Berezhnoi. Anisotropy of the electrooptical effect in the plane of a light wavefront. *Opt. Spectrosc.* (USSR), 44(2), Februrary 1978.

[10] M. Bertolotti, B. Daino, F. Scudieri, and D. Sette. *Spatial Distribution of Light Scattered by p-Azoxyanisole in Applied Electric Field*, pages 123–130. In Brown and Labes [14], 1972.

[11] L. M. Blinov and V. G. Chigrinov. *Electrooptic Effects in Liquid Crystal Materials.* Springer Verlag, New York, 1993.

[12] M. Born and E. Wolf, editors. *Principles of optics: electromagnetism theory of propagation, interference and difffraction of light.* Pergamon Press, New York, sixth edition, 1980.

[13] G. H. Brown, editor. *Advances in Liquid Crystals.* Academic Press, Orlando, FL.

[14] G. H. Brown and M. M. Labes, editors. *Liquid Crystals 3.* Gordon and Breach, New York, 1972.

[15] F. Bucholtz. *Fiber Optic Magnetic Sensors*, chapter 12, pages 369–408. In Udd [110], 1991.

[16] F. Bucholtz, D. M. Dagenais, and K. P. Koo. High-frequency fibre-optic magnetometer with 70 $fT/\sqrt{(Hz)}$ resolution. *Electronics Letters*, 25(25):1719–1720, 1989.

[17] F. Bucholtz, D. M. Dagenais, and K. P. Koo. Mixing and detection of RF signals in fibre-optic magnetostrictive sensor. *Electronics Letters*, 25(19):1285–1286, 1989.

[18] A. N. Campbell, J. Edward I. Cole, B. A. Dodd, and R. E. Anderson. Internal current probing of integrated cicuits using magnetic force microscopy. *Proceedings of the 31st IEEE Annual Proceedings Reliability Physics 1993*, pages 168–177, 23–25 March 1993.

[19] A. N. Campbell, J. Edward I. Cole, B. A. Dodd, and R. E. Anderson. Magnetic force microscopy/current contrast imaging: A new technique for internal current probing of ics. *Microelectronic Engineering*, 24:11–22, 1994.

[20] J. A. Castellano. *Applications of Liquid Crystals*, pages 439–457. In Saeva [93], 1979.

[21] R. H. Clark. *Printed Circuit Engineering.* , Van Nostrand Reinhold, New York, 1989.

[22] J. F. Colaruotolo. Hydrophone preamplifier and line driver for the autec acoustic array. *BBN TM 608 (Cambridge, MA)*, February 1981.

[23] S. H. Crandall, N. C. Dahl, and T. J. Lardner. *An Introduction to the Mechanics of Solids.* McGraw–Hill, New York, 1972.

[24] B. D. Cullity, editor. *Introduction to Magnetic Materials.* Addison–Wesley, Reading, MA, 1972.

[25] S. Daijavad, J. Janak, H. Heeb, A. Ruehli, and D. McBride. A fast method for computing radiation from printed circuit boards. *1990 International Symposium on Electromagnetic Compatibility*, pages 300–304, August 1990.

[26] A. Dandridge and G. B. Cogbell. Fiber optic sensors—performance, reliability, smallness. *Sea Technology*, pages 31–37, May 1994.

[27] A. Dandridge, A. B. Tveten, and T. G. Giallorenzi. Homodyne demodulation scheme for fiber 0ptic sensors using phase generated carrier. *IEEE Journal of Quantum Electronics*, QE–18:1647–1652, 1982.

[28] G. T. Davis. *Piezoelectric and Pyroelectric Polymers*, pages 435–465. In Wong [120], 1993.

[29] M. Deeter, G. W. Day, and A. H. Rose. *Magneto-Optic Materials*, chapter 8. In Webber [118], (to appear).

[30] D. S. Dixon, M. Obura, and N. Schade. Finite-element analysis (FEA) as an EMC prediction tool. *IEEE Transactions on Electromagnetic Compatibility*, 35(2):241–??, May 1993.

[31] R. C. Dorf, editor. *The Electrical Engineering Handbook*. CRC, Boca Raton, Florida, 1993.

[32] A. F. Drake. Polarisation modulation—the measurement of linear and circular dichroism. *J. Phys. E: Sci. Instrum.*, 19, 1986.

[33] R. D. Ennulat and J. L. Fergason. *Thermal Radiography Utilizing Liquid Crystals*, pages 141–156. In Brown and Labes [14], 1972.

[34] L. Fabiny, S. Y. Vohra, and F. Bucholtz. High-resolution fiber-optic low-frequency voltage sensor based on the electostrictive effect. *IEEE Photonics Technology Letters*, 5(8):952–953, August 1993.

[35] M. M. Fleck. Topological image matcher. Technical Report OUEL-1798/89; ETN-90-97049, Oxford University, England, 1989. NTIS No: N90-25600/9/HDM.

[36] M. J. Freiser. A survey of magnetooptic effects. *IEEE Trans. Magn.*, MAG-4(2):152–161, 1968.

[37] B. Fuller and R. Goering. Edif PC-board standard moves ahead. *Electrical Engineering Times*, page 76, 13 June 1994.

[38] J. N. Funk, M. P. Mengüç, K. A. Tagavi, and C. J. Cremers. A semi-analytical method to predict printed circuit board package temperatures. *IEEE Transactions on Components, Hybrids, and Manufacturing Technology*, 15(5):675–684, October 1992.

[39] B. Gabrielson. Future EMC trends in PC board design. *EMC EXPO 86: International Conference on Electromagnetic Compatibility*, pages T18.4–T.18.7, June 1986.

[40] H. Gazit. A deterministic parallel algorithm for planar graph isomorphism. In *32nd Annual Symposium on Foundations of Computer Science (San Juan, PR, 1991)*, pages 723–732. IEEE Comput. Soc. Press, Los Alamitos, CA, 1991.

[41] R. F. German, H. W. Ott, and C. R. Paul. Effect of an image plane on printed circuit board radiation. *1990 International Symposium on Electromagnetic Compatibility*, pages 284–291, August 1990.

[42] C. J. Gerritsma and P. V. Zanten. *Electric-Field-Induced Texture Transformation and Pitch Contraction in a Cholesteric Liquid Crystal*, pages 751–762. In Brown and Labes [14], 1972.

[43] T. G. Giallorenzi, J. A. Bucaro, A. Dandridge, G. H. Sigel, Jr, J. H. Cole, S. C. Rashleigh, and R. G. Priest. Optical fiber sensor technology. *IEEE Journal of Quantum Electronics*, QE-18(4):626–664, April 1982.

[44] W. M. Godfrey, K. A. Tagavi, M. P. Mengüç, and C. J. Cremers. Interactive thermal modeling of electronic circuit boards. In *ASME Winter Annual Meeting (Dallas)*. ASME, December 1990.

[45] Y. P. Gousev, G. N. Gol'tsman, A. D. Semenov, E. M. Gershenzon, R. S. Nebosis, M. A. Heusinger, and K. F. Renk. Broadband ultrafast superconducting NbN detector for electromagnetic radiation. *J. Appl. Phys*, 75(7):3695–3697, 1 April 1994.

[46] D. Halliday and R. Resnick, editors. *Physics: Part II*. John Wiley & Sons, New York, 1962.

[47] K. B. Hardin, C. R. Paul, and K. Naishadham. Direct prediction of common-mode currents. In *IEEE International Symposium on Electromagnetic Comptability*, pages 67–71, Cherry Hill, NJ, 12–16 August 1991. IEEE.

[48] U. Hartmann. Theory of magnetic force microscopy. *Journal of Vacuum Science and Technology A*, 8(1):411–415, 1990.

[49] Y. Y. Hung, N. H. Wang, and H. Q. Ruan. Specklegrammetry for precision surface coordinate measurement. *SPIE Industrial Laser Interferometry*, 955:14–25, 1988.

[50] J. D. Jackson. *Classical Electrodynamics*. John Wiley & Sons, New York, 1962.

[51] A. H. Kamel. Cost-effective schemes for the numerical simulation of electromagnetic waves. *Journal of Electromagnetic Waves and Applications*, 8(6):693–710, 1994.

[52] E. Kaneko. *Liquid Crystals TV Displays: principles and applications of liquid crystal displays*. D. Reidel Publishing Company, Boston, 1987.

[53] H. Kaplan. An update of commercially available infared thermal imaging systems. In A. D. Gara, editor, *Optical Sensing and Measurement*, pages 99–108. Springer–Verlag, 1988.

[54] H. Kaplan. 3–D gauging with laser triagnularion. *Photonics SPectra*, pages 50–52, July 1994.

[55] M. P. Kibbe and J. S. Stiff. Operator performance in pattern matching as a function of reference material structure. Technical Report NAWCWPNS-TP-8145, Naval Air Weapons Station, China Lake, CA, September 1993. NTIS No: AD-A269 889/2/HDM.

[56] J. Kobler, U. Schoning, and J. Toran, editors. *The graph isomorphism probelm: it's structural complexity.* Birkhauser Boston, Boston, 1993.

[57] V. Korthuis, N. Khrosrovani, A. W. Sleight, N. Roberts, R. Dupree, and J. W. W. Warren. Negative thermal expansion of zirconium vanadium phosphates. *Chemistry of Materials*, (to appear).

[58] K. S. Kunz and R. J. Luebbers. *The Finite Difference Time Domain Method for Electromagnetics.* CRC, Boca Raton, Florida, 1993.

[59] K. Kyuma, S. Tai, M. Nunshita, T. Takioka, and Y. Ida. Fiber optic measuring system for electric current by using a magnetooptic sensor. *IEEE Journal of Quantum ELectronics*, QE-18(10):1619–1623, 10 October 1982.

[60] F. J. Langley, R. R. Boatright, and L. Crosby. Composite electro-optic testing of surface-mount device boards – one manufacturer's experience. In *1989 International Test Conference*, pages 686–691. IEEE, 1989.

[61] R. Laroussi and G. I. Costache. Far-field predictions from near-field measurements using an exact integral equation solution. *IEEE Transactions on Electromagnetic Compatibility*, 36(3):189–195, August 1994.

[62] R. Laroussi and I. Costache. Finite-element methods applied to EMC problems. *IEEE Transactions on Electromagnetic Compatibility*, 35(2):178–??, May 1993.

[63] J. E. Lenz. A review of magnetic sensors. *Proceedings of the IEEE*, 78:973–989, 1990.

[64] F. M. Leslie. *Distortion of Twisted Orientation Patterns in Liquid Crystals by Magnetic Fields*, pages 763–778. In Brown and Labes [14], 1972.

[65] D. R. Lide, editor. *Handbook of Chemistry and Physics.* CRC, Boca Raton, Florida, 71st edition, 1990.

[66] C. C. Lin and L. A. Segel. *Mathematics Applied to Deterministic Problems in the Natural Sciences.* Macmillan Publishing Co., New York, 1974.

[67] A. J. Maddocks. Summary of recommendations in published literature on circuit board design for minimun electromagnetic radiation. Technical report, ERA Technology Ltd, 1990. NTIS number: ERATL-91/04/HDM.

[68] G. A. Massey, D. C. Erickson, and R. A. Kadlec. Electromagnetic field components: their measurement using linear electroptic and magnetooptic effects. *Applied Optics*, 14(11):2712–2719, November 1975.

[69] K. Matsuda and *et al.* Bi-substituted, rare earth iron garnet composite film with temperature independent faraday rotation for optical isolators. *IEEE Trans. Mag.*, MAG-23:3479, 1987.

[70] M. D. Mermelstein. Fundamental limit to the performance of fibre-optic metallic glass DC magnetometers. *Electronics Letters*, 21:1178–1179, 1985.

[71] P. Moon and D. E. Spencer, editors. *Field Theory Handbook.* Springer–Verlag, Berlin, 1961.

[72] Morgan Matroc, Inc. Guide to modern piezoelectric ceramics. *Product Literature*, July 1991.

[73] P. M. Morse and K. U. Ingard. *Theoretical Acoustics.* McGraw–Hill, 1962.

[74] G. Mur. The finite-element modeling of three-dimensional electromagnetic fields using edge and nodal elements. *IEEE Transactions on Antenna and Propagation*, 41(7):948–953, July 1993.

[75] D. H. Naghski, J. T. Boyd, H. E. Jackson, S.Sriram, S. A. Kingsley, and J. Latess. An integrated photonic mach–zender interferometer with no electrodes for sensing electric fields. *Journal of Lightwave Technology*, 12(6):1092–1098, June 1994.

[76] J. D. Norgard, R. M. Sega, M. G. Harrison, and H. H. Pohle. Infrared mapping of transient electromagnetic-fields radiated by high-power microwave pulsed sources. *IEEE Transactions on Nuclear Science*, 39:1912–1920, 1992.

[77] S. A. Oliver, C. A. DiMarzio, S. C. Lindberg, and A. B. Kale. Magnetic field measurements using magneto-optic kerr effect sensors. *Optical Engineering*, (to appear).

[78] S. A. Oliver, C. A. DiMarzio, S. C. Lindberg, S. W. McKnight, and A. B. Kale. Measurement of magnetic fields using the magneto-optic Kerr effect. *Applied Physics Letters*, 63(3):415–417, July 1993.

[79] G. H. Olsen. A high performance room-temperature near-infrared camera. *Government Report AD–A260 602*, January 1993.

[80] A. V. Oppenheim and R. W. Schafer, editors. *Digital Signal Processing.* Prentice–Hall, Englewood Cliffs, NJ, 1975.

[81] C. R. Paul. A comparison of the contributions of common-mode and differential-mode currents in radiated emissions. *IEEE Transactions on Electromagnetic Compatibility*, EMC-31:189–193, 1989.

[82] C. R. Paul. *Introduction to Electromagnetic Compatibility.* John Wiley, New York, 1992.

[83] K. V. Pearson. Printed circuit board fault detection and isolation using thermal imaging techniques. *SPIE* Thermal Imaging, 636:122–125, 1986.

[84] W. D. Pilkey and P. Y. Chang. *Modern Formulas for Statics and Dynamics.* McGraw–Hill, New York.

[85] F. Piriou and A. Razek. Finite element analysis in electromagnetic systems: Accounting for electric circuits. *IEEE Transactions on Magnetics*, 29:1669–??, March 1993.

[86] J. D. Previti. EMSCAN: A tool to measure EMI emissions from printed circuit packs. *EMC Testing*, pages 4–5, November–December 1989.

[87] L. Råde and B. Westergren. *Beta Mathematics Handbook.* CRC, Boca Raton, Florida, second edition, 1992.

[88] H. S. Ranganath and L. J. L. J. Chipman. Graph theoretic approach to scene matching. Technical report, Alabama University, Huntsville, Alabama, 1 August 1991. NTIS No: N91-31947/5/HDM.

[89] M. E. Re and M. H. Kryder. Magneto-optic determination of magnetic recording head fields. *IEEE Trans. Magn.*, MAG-22(5):840–842, 1986.

[90] F. S. Roberts. *Applied Combinatorics.* Prentice-Hall, Inc, Englewood Cliffs, NJ, 1984.

[91] J. C. Russ, editor. *The Image Processing Handbook.* CRC, Boca Raton, FL, 1992.

[92] M. N. O. Sadiku. *Numerical Techniques in Electromagnetics.* CRC, Boca Raton, Florida, 1992.

[93] F. D. Saeva, editor. *Liquid Crystals: the fourth state of matter.* Marcel Dekker, New York, 1979.

[94] N. Samarth and J. K. Furdyna. Diluted magnetic semiconductors. *Proceeedings IEEE*, 78(6):990–1003, 1990.

[95] J. S. Sanders, C. R. Halford, and K. A. Krapels. Human recognition of infared images. In *Infared imaging systems: Design, Analysis, Modeling, and Testing*, volume 1309, 1990.

[96] J. L. C. Sanz. *Advances in Machine Vision.* Springer-Verlag, Berlin, 1989.

[97] R. Schaetzing and J. D. Litster. *Light-Scattering Studies of Liquid Crystals*, pages 147–206. In Brown [13].

[98] R. M. Sega. Infared detection of microwave induced surface currents on flat plates. Technical Report RADC-TR-82-308, ??, 1982.

[99] R. M. Sega and G. J. Genello. Infared thermography; techniques for EMI/EMC measurements. *Proceedings of Electromagnetic Compatability '83*, pages 29–33, August 1983.

[100] R. M. Sega, J. D. Norgard, and A. L. Sapp. Infared images of microwave scattering from a ferrite coated cylinder. *SPIE International Conference on Thermal Infared Sensing*, 934:194–201, April 1988.

[101] O. Silvén, I. Virtanen, T. Westman, T. Piironen, and M. Pietikäinen. *A Design Data-Based Visual Inspection System for Printed Wiring*, chapter 5, pages 192–212. In Sanz [96], 1989.

[102] S. Sriram. Optical interferometers for sensing electromagnetic fields. *Government report AD-A273 712*, 1991.

[103] K. R. Stewart. Organic crystals give optoelectronics a boost. *Photonics Spectra*, pages 104–108, July 1994.

[104] J. A. Stratton, editor. *Electromagnetism theory.* McGraw–Hill, New York, 1941.

[105] J. C. Suits. Faraday and kerr effects in magnetic compounds. *IEEE Transactions on Magnetics*, MAG-8(1):95–105, 1972.

[106] J. Thewlis, editor. *Encyclopaedic Dictionary of Physics.* Pergamon Press, New York, 1962.

[107] H. Trabelsi, F. Rioux-Damidau, and B. Bandelier. Finite element 3d modelling of electromagnetic fields with tetrahedral and hexahedral elements. *J. Phys. III France*, 2:2069–2081, November 1992.

[108] G. Tremblay and P. Meyrueix. Optical reading of voltages on printed circuit boards. *Microelectronic Engineering*, 7:377–383, 1988.

[109] G. Tremblay, P. Meyrueix, and J. C. Peuzin. Optical testing of printed circuit boards. *IEEE International Test Conference*, pages 695–699, 1988.

[110] E. Udd, editor. *Fiber Optic Sensors: An Introduction for Engineers and Scientists.* John Wiley & Sons, New York, 1991.

[111] P. M. Vetoshko, R. I. Kononov, and A. Y. Toporov. A magnetooptical visualizer of microscopic magnetic fields. *Pribory i Tekhnika Eksperimenta*, 5:151–156, September–October 1993.

[112] S. T. Vohra and F. Bucholtz. Fiber-optic AC electric-field sensor based on the electrostrictive effect. *Opt. Lett.*, 17(5):372, 1992.

[113] S. T. Vohra, F. Bucholtz, and A. D. Kersey. Fiber-optic DC and low frequency electric field sensor. *Opt. Lett.*, 16(18):1445, 1991.

[114] S. T. Vohra and L. Fabiny. Mixing and detection of microwave signals in fibre-optic electrostrictive sensor. *Electronics Letters*, 30(5):444–445, 3 March 1994.

[115] R. L. Walter, IV. Identifying EMI parameters on printed circuit boards. *EMC EXPO 86: International Conference on Electromagnetic Compatibility*, pages T18.12–T.18.16, June 1986.

[116] P. K. U. Wang. Emerging trends in simulation. *Printed Circuit Design*, May 1994.

[117] T. T. Wang, J. J. Herbert, and A. M. Glass. *Applications of Ferroelectric Polymers.* Chapman & Hall, 1987.

[118] M. Webber. *(to appear).* CRC, Boca Raton, FL, (to appear).

[119] R. S. Weis and T. K. Gaylord. Lithium niobate: Summary of physical properties and crystal structure. *Appl. Phys. A*, 37:191–203, 1985.

[120] C. P. Wong, editor. *Polymers for Electronic and Photonic Applications.* Academic Press, Orlando, Fl, 1993.

[121] O. Y. Zharii. Normal mode expansions in dynamic electroelasticity and their application to electromechanical energy conversion. *J. Acoust. Soc. Am.*, 92(1):57–68, July 1992.

[122] Z. H. Zhu, J. P. Weber, and S. Y. Wang. New measurement technique: CW electro-optic probing of electric fields. *Appl. Phys. Lett.*, 49(8), 25 August 1986.

[123] D. Zwillinger. *Handbook of Differential Equations.* Academic Press, Orlando, Fl, second edition, 1992.

[124] D. Zwillinger. *Handbook of Integration.* Jones and Bartlett, Boston, 1992.

B Reference Material

B.1 Acronyms

Some of the common acronyms in the field of printed circuit board, analysis, and test are the following (not all have been used in this report):

ASCII American Standard Code for Information Interchange
ATE automated test equipment
ATS automatic test system
BUT board under test
CAD computer aided design
CMOS Complementary metal oxide semiconductor
COTS commercial off-the-shell
DEC Digital Equipment Corporation
DUT device under test
DoD Department of Defense
EDA electronic design automation
EDIF Electronic Design Interchange Format
EMC electromagnetic compatibility
EMI electromagnetic interference
FEA finite-element analysis
IGES Initial Graphics Exchange Specification
IPC The Institute for Interconnecting and Packaging Electronic Circuits
IR infrared
KGB known good board
MCM multichip modulus
MOKE magnetooptic Kerr effect
PCB printed circuit board; these are either "bare" or "assembled"
PDES Product Definition Exchange Specification
PVDF polyvinylideine fluoride
PWB printed wiring board
PZT lead–zirconate–titanate
SA signature analysis
SMD surface mount device
SQUID superconducting quantum interference device
TAFF test application and fault finding
TTL Transistor–transistor logic
Tesla 1 weber per square meter
UUT unit under test
VHDL VHSIC Hardware Description Language
s-a-0 stuck at 0
s-a-1 stuck at 1
nm nanometer (equal to 10^{-9} meter)

B.2 Mathematical notation

This proposal consistently uses many letters to represent physical quantities. Following are definitions of these terms:

B magnetic induction
E nominal electric field
F force
H magnetic field strength
J^* surface current density
L length of interaction
S strain in piezoelectric material
T sampling time
V nominal voltage
W bandwidth of signal to be measured
$\Delta\theta$ phase shift
$\mathbf{S}$ strain (relative elongation)
$\mathbf{T}$ stress (force per unit area)
$\mathbf{d}$ coupling coefficients for a piezoelectric material
δ displacement
ϵ permittivity
ϵ strain in a piezoelectric— material
λ Lamé constant for a piezoelectric material
λ free-space wavelength of light wave
μ_0 permeability of free space ($4\pi \times 10^{-7}$ weber/amp-meter)
μ permeability
μ rigidity modulus for a piezoelectric material
ω radian frequency of electromagnetic field on card
ϕ angle of light ray with respect to normal
ρ_A density (units of mass per unit area)
ρ depending on context: Verdet constant, or density (units of mass per unit volume)
σ Stefan–Boltzman constant, $\sigma = 5.67 \times 10^{-8}$ watt/(meter^2)($^\circ$K)^4
θ phase along probing light ray
c speed of light in vacuum, $c = 2 \times 10^8$ m/sec
d_{33} strain constant
d nominal distance of sensitive sheet (apparatus) from circuit card
e emissivity

h	height of the wires above the ground plane
i	nominal current in circuit card
k	wavenumber of optical field $(2\pi/\lambda)$.
m	mass per unit area of a flat plate
n	index of refraction
r_{63}	electric optic coefficient
t	nominal thickness of apparatus
w	nominal width between traces

B.3 Glossary

This proposal consistently uses many technical words that may be unfamiliar. Following are definitions of these terms:

- **circular birefringence** See optical rotation.
- **CMOS** Complementary Metal Oxide Semiconductor defines a type of digital circuit. It is characterized by a high digital signal state above 3.5 VDC, and low digital state below 1.5 VDC. Operating voltage is typically around 12 VDC. CMOS circuits are characterized by high nose immunity.
- **comparative tester** Evaluation of a component by comparing its performance to that of a properly functioning component.
- **digital signal** A discrete signal that assumes one of two states: high or low.
- **dielectric** A substance that can sustain an electric field and act as an insulator.
- **electric displacement (D)** The electric flux per unit area, or electric flux density, when an electric field exists in free space with magnitude **E** and a dielectric is introduced into the field.
- **electric field strength (E)** The strength of an electric field at a given point in terms of the force exerted by the field on the unit charge at that point.
- **fields**
  - **electrostatic fields** These are fields produced by static electric charges.
  - **magnetostatic fields** These are fields produced by the motion of electric charges with uniform velocity (direct current).
  - **time-varying fields** These are fields produced by accelerated charges or time-varying currents.
- **electrorheological property** Property exhibited by some fluids that are capable of altering their flow characteristics depending on an externally applied electric field.
- **electrostriction** The change in size of a nonpolarized, dielectric material when it is placed in an electric field.
- **Faraday rotation** First order isotropic nonreciprocal magnetooptical effect which causes the polarization direction of a polarized transmitted light to rotate when the propagation direction of the incident light is parallel to the direction of the applied magnetization of the magnetooptic medium. It is also known as magnetic circular birefringence.
- **free space** A space containing no particles and no force fields (note that a vacuum may contain fields).
- **ground plane** A region on a circuit card maintained at 0 Volts.
- **in-circuit testing** Evaluating the functioning of a component without removing the component from the circuit in which it is being used.
- **interfacial connection** A conductor that connects conductive patterns on opposite sides of the laminate.
- **Kerr effects** Reflected light from a magnetooptical medium which can be described by the optical Kerr effects. There are three types of Kerr effects: polar, longitudinal, and transverse, depending on the directions of the magnetization with respect to the plane of incidence and the reflecting film surface.
- **line** Synonym for trace.
- **linear birefringence** This refers to slight differences in the refractive index of a material depending on the different linear polarization states of light.
- **magnetic field strength (H)** A vector quantity given by $\mathbf{B}/\mu$, where **B** is the magnetic flux density and μ is the medium's permeability. It represents the strength of the magnetic field at a point in the direction of the line of force at that point.

- **magnetic flux density (B)** The magnetic flux passing through a magnetic field at right angles to the magnetic force. This vector quantity's magnitude is proportional to the magnetic field strength, and its direction at that point is that of the magnetic field. It indicates the magnetic field's strength, often in terms of the field's affects.
- **magnetic flux** The product if the particular area and the component, normal to the area, of the average magnetic flux density over it.
- **optical rotation** This refers to the slight difference in the refractive indices for the two senses of polarized light.
- **piezoelectric** A material which exhibits an external electric field when a stress is applied to the material and a charge flow proportional to the strain is observed when a closed surface is attached to electrodes on the surface of a material.
- **permeability (μ)** The ratio of the magnetic flux density in a body or medium (**B**) to the external magnetic field strength inducing it (**H**). The relative permeability, μ_r, is the ratio μ/μ_0, where μ_0 is the magnetic constant, or permeability of free space.
- **permittivity (ϵ)** The ratio of the electric displacement in a dielectric medium (**D**) to the applied electric field strength (**E**), indicating the degree to which the medium can resist the flow of electric charge; it is measured in farads per meter.
- **polar Kerr effect** The polar Kerr effect takes place when the magnetization is perpendicular to the plane of the material. A pair of orthogonal linearly polarized reflected lightmodes will be induced and the total reflected light becomes elliptically polarized. The orientation of the major axis of the elliptic polarization of the reflected light is the same for both TE ($E_{i\perp}$) or TM ($E_{i||}$) linearly polarized incident lights since $r_{11} = r_{21}$.
- **plated-through hole** Metal deposited on sides of the hole through the laminate for electrical connecting purposes and extending to the conductive pattern on both sides of the laminate.
- **printed circuit assembly** A printed circuit board on which separately manufactured components have been added.
- **printed contact** That part of a printed circuit used to connect the conductive pattern to a plug-in receptacle, or the equivalent of a pin on a male plug. It was previously known as "tab" or "finger".
- **terminal area** That part of a printed circuit that makes connection to the conductive pattern, such as the enlarged area of conductor material around a component-mounted hole. This is preferred to such terms as "boss, land, pad, or terminal pad".
- **trace** This is a conductor on a printed circuit board. Standard sizes for copper are 1 oz (corresponding to 0.0014" in thickness) and 2 oz (corresponding to 0.0028").
- **TTL** Transistor transistor logic defines a type of digital circuit. It is characterized by a high digital signal state above 2 VDC, and low digital state below 0.8 VDC. Operating voltage is typically 5 VDC.
- **via** A via is a connection between two layers of a circuit board. A buried via is one in which neither end of the via terminates on an external layer of the circuit board. A via that extends between the top and bottom of a circuit board is called a "through hole".

C Limitation of Electrodynamic Techniques

C.1 Limitation due to plate motion

The sensing plate for the piezoelectric and electrodynamic techniques is naturally modeled as an isotropic uniform plate. Since we are measuring small changes of the plate, we must ensure that the natural frequency modes of the plate are far from the mechanical frequency with which the circuit will be driving it. A moving plate has many competing forces that influence its motion; these include inertial factors, stiffness factors, tension factors, and applied stresses. If

- the plate is undergoing sinusoidal oscillations at frequency ω
- E is the modulus of elasticity of the plate
- I is the moment of inertia of the plate
- T is the tension in the plate
- T_{zz} represents the applied stress
- ν is Poisson's ratio
- ρ is the density of the plate
- h is the thickness of the plate
- k is the wavelength of the applied stress
- u_z is the motion of the plate in the $\mathbf{j}$ direction

then the motion of the plate is well described by the formula (see Morse and Ingard [73])

$$\left[-\rho h\omega^2 + Tk^2 + \frac{EI}{1-\nu^2}k^4\right] u_z = T_{zz} \tag{18}$$

The terms in the bracket in equation 18, from left to right, are: the inertial term, the tension term, and the stiffness term.

When the wavelength is sufficiently low, or the frequency is sufficiently high, then the inertial term dominates the other terms in equation 18. In this case the plate is called a "limp mass" and obeys

$$-\rho h\omega^2 u_z = T_{zz} \tag{19}$$

That is, the applied stress is immediately translated into vertical displacement.

To determine what a sufficiently high frequency is, we need to be operating above the natural frequency of the plate (ω_{natural}) (this parameter is calculated in section C.1.1). We also must ensure that the operating frequency is below the thickness resonance of the plate (ω_{tr}) (this parameter is calculated in section C.1.2). Hence, we require that $\omega_{\text{natural}} < \omega < \omega_{\text{tr}}$.

Note that if we attempted to determine the response at DC (i.e., when $\omega = 0$) we would need to consider classical beam theory (with tension) to determine the motion of the plate. The problem with using beam theory is that the plate then has a non-local response. That is, the local deformation can be substantially influenced by forcing a substantial distance away.

C.1.1 Natural frequencies of a plate

From Pilkey and Change [84] (formula (12.7a)) we find that the natural frequencies of a plate of size L_x by L_y, ω_{mn} are given by

$$\omega_{mn} = \frac{k_{mn}}{L_y^2}\sqrt{\frac{Eh^3}{12(1-\nu^2)\rho_A}} \tag{20}$$

where E is the modulus of elasticity, ν is Possion's ration, ρ_A is the density (in units of mass per unit area), and the values of the $\{k_{mn}\}$, for different types of plate support, are given by table 17.

To find a minimum natural mode frequency, we take the limit for an infinitely slender plate (i.e. $\alpha = 0$ in table 17). In all cases tabulated, we find that k_{11}, which corresponds to the lowest frequency, is given by

$x = 0$	$x = L_x$	$y = 0$	$y = L_y$	Value of k_{mn}
S	S	S	S	$k_{mn} = \pi^2(m^2 + \alpha^2 n^2)$
C	C	S	S	$k_{11} = \pi^2\sqrt{1 + 2.5\alpha^2 + 5.14\alpha^4}$,
				$k_{12} = 4\pi^2\sqrt{1 + 0.625\alpha^2 + 0.321\alpha^4}$,
				$k_{21} = \pi^2\sqrt{1 + 9.32\alpha^2 + 39.06\alpha^4}$
C	S	S	S	$k_{11} = \pi^2\sqrt{1 + 2.33\alpha^2 + 2.44\alpha^4}$,
				$k_{12} = 4\pi^2\sqrt{1 + 0.582\alpha^2 + 0.152\alpha^4}$,
				$k_{21} = \pi^2\sqrt{1 + 8.69\alpha^2 + 25.63\alpha^4}$

Table 17: Constants for natural frequency formula
"S" represents simply supported, "C" represents clamped, α is the aspect ratio ($\alpha = L_y/L_x$)

Material	E (in N/m^2)	ρ (in gm/cc)	ν
Aluminum	69×10^9	2.7	0.34
Copper	120×10^9	8.9	0.34
Steel	200×10^9	7.8	0.29

Table 18: Material parameters required for plates
Data is from Crandall, *et al.* [23]

$k_{11} = \pi$. Evaluating equation 20 for the materials in table 18, with $k_{11} = \pi$, we find that $\omega_{11,\text{aluminum}} = 270000R/\text{sec}$, $\omega_{11,\text{copper}} = 640000R/\text{sec}$, and $\omega_{11,\text{steel}} = 480000R/\text{sec}$, where R is the ratio $R = h/L_y^2$, and both h and L_y are measured in centimeters. Hence, the lowest frequency that we need to be concerned with is that for aluminum. For the sample numbers $h = 1$ mm and $L_y = 10$ cm (about 4 inches) we have $\omega_0 = \omega_{11,\text{copper}} \approx 600/\text{sec}$.

C.1.2 Thickness resonance

A sheet of an elastic material experiences resonances due to the thickness. If k_ℓ is the longitudinal wavenumber of the material, and h is the thickness of the sheet, then the classic quarter wavelength resonance (for a plate blocked on one side) occurs at $k_\ell h = \pi/2$.

When there is a free surface on each side of the sensing sheet, then the first resonance will occur when $k_\ell h = \pi/2$. The parameter k_ℓ is given by $k_\ell = \omega/c_\ell$, where c_ℓ is the speed of longitudinal waves and ω is (as usual) the frequency of excitation. Hence resonances will occur when

$$\omega \geq \pi\frac{c_\ell}{h} \qquad \textit{or} \qquad \omega \geq 2\pi\frac{c_\ell}{h}$$

depending on whether the plate is blocked, or free.

We note that the bar wave speed for known piezoelectric materials is approximately 1000 m/sec. When $h = 1$ mm this results in a maximum operating frequency of 1 MHz or 2 MHz. Hence, to avoid thickness resonance effects, the operating frequency must be below 1 MHz.

C.2 Limitation of surface current

In the electrodynamic technique, we apply a surface current to a thin sheet of metallic material. Since the surface current mechanically affects the sensing sheet, there is a maximum amount of surface current that can be applied. The surface current is potentially limited by at least two distinct effects, a thermal effect and an electrical effect.

- As a current passes through the sensing sheet, the sheet produces Joule heating, which increases the temperature of the sensing sheet. Since most materials expand when heated, a large deformation of the sensing sheet could be due to Joule heating, and not just the underlying magnetic field. While

parameter	description	value
l	length of sheet	10 cm
w	width of sheet	20 cm
h	thickness of sheet	1 mm
δt	system operation time	0.01 sec

Table 19: Parameters for thermal effects for electrodynamic technique

	thermal expansion coefficient ($10^{-6}/°K$)	electrical resistivity (10^{-8} Ω-m)	specific heat (cal/gm-°C)	mass per unit volume (gm/cc)	$10^4 \times \alpha/cm$ (MKS units)
Aluminum	$\alpha_{Al} = 25$	$\rho_{Al} = 2.42$	$c_{V;Al} = 0.215$	$m_{Al} = 2.70$	10.3
Chromium	$\alpha_{Cr} = 6$	$\rho_{Cr} = 12.9$	$c_{V;Cr} = 0.110$	$m_{Cr} = 7.19$	1.8
Copper	$\alpha_{Cu} = 16.6$	$\rho_{Cu} = 1.53$	$c_{V;Cu} = 0.092$	$m_{Cu} = 8.96$	4.8
Gold	$\alpha_{Au} = 14.2$	$\rho_{Au} = 2.05$	$c_{V;Au} = 0.031$	$m_{Au} = 19.3$	5.7
Silver	$\alpha_{Ag} = 19$	$\rho_{Ag} = 1.47$	$c_{V;Ag} = 0.057$	$m_{Ag} = 10.5$	7.6
Vanadium	$\alpha_V = 8$	$\rho_V = 18.1$	$c_{V;V} = 0.116$	$m_V = 6.11$	2.7

The values in this table are taken from Lide [65], page 12-23 (at 0°C) and page 12-107 (at 25° C).

Table 20: Parameters for specific materials for thermal effects

active cooling could be used to reduce the heat build-up, this has not yet been investigated. See section C.2.1.

- The surface current on the sensing sheet is achieved by applying a potential difference across the sheet. If this potential difference is too large, then arcing can occur in the air around the sheet. See section C.2.2.

From analysis of the above two effects, we observe that arcing is not a serious problem. Joule heating concerns, though, limit the maximum surface current to approximately 100,000 amps/meter. Supplying the required currents in practice may be difficult.

C.2.1 Thermal effects

Consider a thin metallic sheet of length l, width w, and thickness h. We presume that the sheet has a resistivity of ρ, a mass density of m, a specific heat of c, and a thermal expansion coefficient of α. (Note that table 19 contains the definitions and values for some of the thermal parameters used in this analysis, and table 20 contains and values of the relevant parameters for several different materials.)

The sheet then has a cross-sectional area of $A = wh$, a volume of $\text{VOL} = Al = whl$, and a total mass of $M = (\text{VOL})m$. The total electrical resistance is given by $R = \rho l/A$. If a voltage of V is applied across the sheet, then the current is given by $I = V/R$. The power expenditure in Joule heating is given by $P = I^2R$, and the surface current will be $J^* = I/l$.

We now presume that the device is operated for a total time of δt; during this time all measurements of the sensing sheet will be completed. In this time period, the total energy produced via Joule heating is $E = (\delta t)P$. From this we can determine the change in temperature of the sample to be $\delta T = E/Mc$. Finally, the deformation rate of the sheet is given by $(\delta T)\alpha$ so that the incremental change in height of the sensing sheet is given by $\delta h = h(\delta T)\alpha$.

Separating out the components of the two quantities of interest we find that:

$V = 0.05$ Volts	$V = 0.077$ Volts	$V = 0.20$ Volts
$\delta h = 16 \times 10^{-9}$ meter $= 16$ nm $J^* = 65,000$ amp/meter	$\delta h = 38 \times 10^{-9}$ meter $= 38$ nm $J^* = 100,000$ amp/meter	$\delta h = 250 \times 10^{-9}$ meter $= 250$ nm $J^* = 260,000$ amp/meter

Table 21: Thermal deformation of copper sensing sheet, and surface current, for 0.1 s measurement

$$\delta h = \underbrace{\frac{\alpha}{cm\rho}}_{\text{material of sheet}} \underbrace{\frac{h}{l^2}}_{\text{sheet size}} \underbrace{\delta t\, V^2}_{\text{operating conditions}}$$

$$J^* = \overbrace{\frac{1}{\rho}} \overbrace{\frac{wh}{l^2}} \overbrace{V}$$

or

$$\delta h = J^* \overbrace{\frac{\alpha}{cm}}^{\text{sheet parameters}} \overbrace{\frac{1}{w}}^{\text{size parameters}} \overbrace{\delta t\, V}^{\text{operating parameters}}$$

We need to have δh as small as possible, certainly it should be smaller than the size of the effect that we are attempting to measure. At the same time, we would like J^* to be as large as possible. From investigation of the preceding equations we observe that these simultaneous goals are achieved in the following limits:

- quantities that should be large: w
- quantities that should be small: δt, V, and $\dfrac{\alpha}{cm}$

Note that table 20 has values of α/cm for a number of materials. Since copper has the least value of α/cm, that is the material of choice. By setting $\delta t = 0.1$ seconds, and specifying V and a material, we can determine δh and J^*. Table 21 shows the deformation and surface current for a copper sensing sheet.

We note two ways in which the surface current might be increased without increasing δh:

- Active cooling could be used to cool the sensing sheet.
- New, exotic materials could be used to restrict the thermal expansion. For example, a new class of materials (constructed from zirconium, vanadium, and phosphorus, and oxygen) have been developed by Sleight *et al.* [57] that contract when the temperature is increased (their thermal expansion coefficients are approximately $-150 \times 10^{-6}/°\text{K}$). Because of their composition, these new materials are not conductors. Sleight and his colleagues is presently trying to combine this new material with other materials to create a conductor that does not expand much.[40]
  United States patent number 5,322,559, with the title "Negative Thermal Expansion Material", was awarded for these new materials) on 21 June 1994.

C.2.2 Arcing

The sparking potential, or minimum breakdown voltage of a gap, denotes the magnitude of the minimum voltage which causes a spark to form in the gap. It is generally measured under conditions where a DC voltage is applied to a gap and the voltage is slowly increased until breakdown occurs. For rapid rates of rise of voltage the gap may not break down until the voltage exceeds the minimum breakdown voltage because of the specifics of the spark formation process.

Suppose that the sparking potential V is measured for a uniform-field discharge of gap length l in a gas at a pressure p. Paschen's law states that $V = F(pl)$, some a specific function F. Curves of $F(pl)$ are in Thewlis [106, page 616]. At a pressure of 760 mm Hg and a temperature of 20°C, the breakdown voltage in

[40] Personnel communication.

air between plane electrodes is 30,000 Volts for a separation of 1 cm, and 261,000 Volts for a separation of 10 cm.

Since we intend to use voltages less than 1 Volt, arcing is not a problem in the electrodynamic technique.

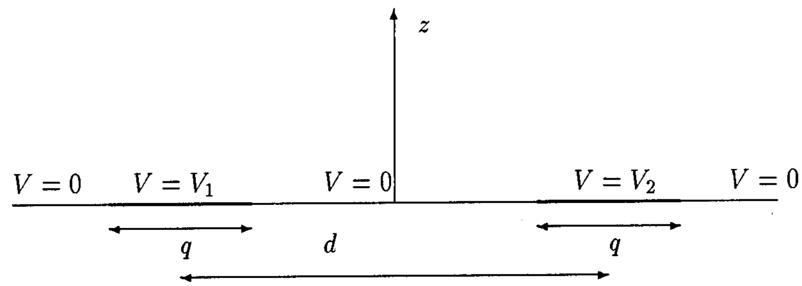

Figure 33: Original electrostatic boundary value problem

D Alternative Electric Field Estimation Computations

This section describes two ways in which Laplace's equation could be solved exactly, without resorting to the approximations in section 3.4.2.

D.1 Bipolar coordinates

The geometry of the problem in figure 10 can naturally be written in terms of bipolar coordinates (see Moon and Spencer [71, page 64]). This coordinate system is given by the conformal map $\bar{z} = a(e^w + 1)/(e^w - 1)$, where $z = x + iy$ and $w = u + iv$. This is equivalent to the change of variables

$$x = \frac{a \sinh u}{\cosh u - \cos v} \qquad y = \frac{a \sin v}{\cosh u - \cos v} \tag{21}$$

In this new coordinate system the electrostatic equation (Laplace's equation) is $\nabla^2 V = V_{uu} + V_{vv} = 0$. This must be supplemented with the boundary conditions for each trace having constant voltage; these are $V = V_0$ on $u = \pi/2$ and $V = -V_0$ on $u = -\pi/2$. The solution to Laplace's equation with these boundary conditions is simply $V = 2V_0 u/\pi$. Note that the voltage on the ground plane, $u = 0$, does vanish as required.

If it were easy to invert the relations in equation 21, then it would be easy matter to determine the voltage field at any point in (x, y) space. Such an inversion leads to formulae in which it is hard to obtain insight.

D.2 Elliptic Functions

This method requires addition assumptions on the structure of the circuit board and the traces. We presume that the two current carrying traces have a width of q, and that their tops are flush with the top of the circuit board. The voltage on the circuit board, away from the traces, is assumed to be $V = 0$. Then, the geometry of the situation is as shown in figure 33.

Since the voltage V solves Laplace's equation in the region above the circuit board, we have the following boundary value problem to solve

$$\begin{array}{ll}
\nabla^2 V = 0 & \text{for } x > 0 \\
V = 0 & \text{for } x < -(d+q)/2 \\
V = V_1 & \text{for } -(d+q)/2 < x < (q-d)/2 \\
V = 0 & \text{for } (q-d)/2 < x < (d-q)/2 \\
V = V_2 & \text{for } (d-q)/2 < x < (d+q)/2 \\
V = 0 & \text{for } (d+q)/2 < x
\end{array}$$

with the radiation condition (that is, there are no outgoing ways at large distances from the circuit board). We scale the independent variables, and introduce the parameter k as follows:

$$x' = \frac{x}{(d-q)/2} \qquad y' = \frac{y}{(d-q)/2} \qquad k = \frac{d-q}{d+q} \tag{22}$$

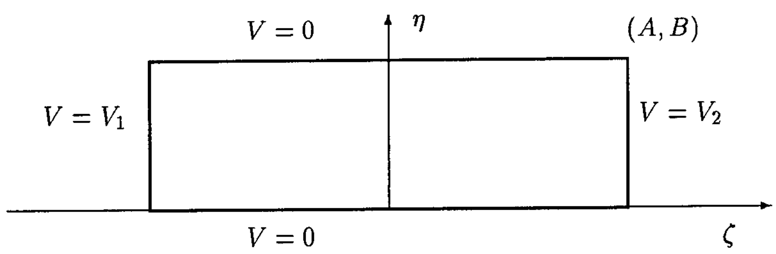

Figure 34: Transformed electrostatic boundary value problem

If we define the complex variable $z = x' + iy'$, then our boundary value problem becomes:

$$\begin{array}{ll}
\nabla_z^2 V = 0 & \text{for } x' > 0 \\
V = 0 & \text{for } x' < -1/k \\
V = V_1 & \text{for } -1/k < x' < -1 \\
V = 0 & \text{for } -1 < x' < 1 \\
V = V_2 & \text{for } 1 < x' < 1/k \\
V = 0 & \text{for } 1/k < x'
\end{array}$$

Our problem is now in exactly the right form to use the conformal mapping in *Beta* [87, page 313, #31]. Changing variables by

$$w = \int_0^z \frac{dt}{\sqrt{(1-t^2)(1-k^2t^2)}} = F\left(\sin^{-1} z, k\right) \tag{23}$$

where $F(\phi, k)$ is an elliptic function of the first kind (see Zwillinger [124]), our boundary value problem becomes

$$\begin{array}{ll}
\nabla_w^2 V = 0 & -A < \Re w < A, 0 < \Im w < B \\
V = 0 & \Im w = 0 \\
V = 0 & \Im w = B \\
V = V_1 & \Re w = -A \\
V = V_2 & \Re w = A
\end{array}$$

where $\Re w$ denotes the real part of w and $\Im w$ denotes the imaginary part of w. See figure 34 for the current geometry. The values of A and B are given by $A + iB = w(z = 1/k) = F\left(\sin^{-1} 1/k, k\right)$.

Knowing the expansion of unity in a sine series (see Lin and Segel [66, page 138]) $1 = \frac{4}{\pi} \sum_{n=\text{odd}} \frac{\sin nx}{n}$ for $0 < x < \pi$, we readily solve our boundary value problem as

$$V(w) = V(\eta + i\zeta) = \sum_{n=\text{odd}} \frac{2}{\pi n} \left[(V_1 + V_2) \frac{\cosh n\eta}{\cosh nA} + (V_1 - V_2) \frac{\sinh n\eta}{\sinh nA} \right] \sin n\zeta \tag{24}$$

To relationship between (x, y) and (η, ζ) is given by equations 22 and 23. Finally, the electric field $\mathbf{E}$ is obtained from the voltage field by the formula: $\mathbf{E} = \nabla V$. The field in any given direction $\mathbf{a}$ is then given by $E_{\mathbf{a}} = \nabla V \cdot \mathbf{a}$

To obtain numerical values of the electric field is, in principle, straightforward. Once d and q have been specified we can compute the value of k. With this value we can determine the constants A and B. Then, for every pair of values (x, y) of interest, we can scale to obtain values for x' and y'. Forming $z = x' + iy'$, we can find the w such that $w = F\left(\sin^{-1} z, k\right)$. The voltage is then obtained from equation 24. We can then numerically form the differentiation required to obtain the electric field.

Index